In fact, so far the effect of adiponectin on CVD is controversial. Previous studies reported that middle-aged and older subjects with higher circulating adiponectin levels had a lower incidence of CVD events [3,31]. The increase in plasma adiponectin of type 2 diabetic patients after Pioglitazone treatment was strongly associated with a decrease in hepatic fat content and improvement in hepatic and peripheral insulin sensitivity [32]. Higher insulin sensitivity is well known to be associated with higher incidence of CVD [33]. Therefore, it seems that there are numbers of observation in which high levels of adiponectin are associated with greater insulin sensitivity and thus lower incidence of CVD. Recent studies, however, have demonstrated that high adiponectin levels are associated with higher incidence of CVD and mortality of all causes [4–7]. Thus, an understanding of the physiological mechanisms underlying the positive associations between adiponectin levels and the risk of mortality is important. Wannamethee et al. [4,8] proposed that this relationship may be mediated by sarcopenia, which is defined as age-related loss in muscle mass or strength. However, previous studies showed that BMI [10], weight change [4,5], or muscle mass [6] failed to account for the increased risk of mortality related to circulating adiponectin levels. Conversely, Hozawa et al. [10] reported that significant associations between high adiponectin levels and a high incidence of physical disability and death in the elderly disappeared when the model was adjusted for physical function. These data suggest that positive associations between adiponectin and mortality in old age may be mediated partially by the decline in physical function, but not simply by body or skeletal muscle size. As an important determinant of physical function, muscle strength is suggested to be more important than muscle mass for estimating mortality risk [34]. Thus, our finding of an inverse association between adiponectin levels and muscle strength has led to new insights on a possible intermediary role of muscle strength in the associations of adiponectin levels and mortality risks in the elderly.

Several limitations of this study should be noted. The present study demonstrates an association between serum adiponectin levels and either grip strength or leg extension power, but it does not establish causality because of the cross-sectional design. Therefore, a prospective future study is necessary to clarify this. In addition, our study did not measure skeletal muscle fiber types conclusively; thus, it was unable to ascertain whether the negative association between serum adiponectin levels and muscle strength is mediated by changes in muscle fiber size or fiber type distribution. Furthermore, despite the wide age distribution of our study participants, it was not appropriate to carry out analyses by age group due to a reduction in a negligible sample size. Instead, age was included in the analyses as a confounder. Finally, we may have failed to evaluate other potential confounders in our analysis models.

In summary, this cross-sectional study in Japanese adult men and women demonstrates that serum adiponectin levels are associated significantly and negatively with grip strength and leg extension power independently of age, BMI, PA, nutrient intake, depressive symptoms, metabolic syndrome, hs-CRP levels, and other lifestyle-related potential confounders.

Role of the funding source

This work was supported by a Grant-in-Aid under the Knowledge Cluster Initiative from the Ministry of Education, Culture, Sports, Science, and Technology of Japan. The funding sources had no role in study design, data collection, analysis and interpretation, the writing of the report, or the decision to submit the paper for publication.

Conflicts of interest

The authors have no conflicts of interest to declare.

Acknowledgments

We are grateful to the participants of the Oroshisho Study. The authors also would like to thank for our staff for their dedicated work.

References

[1] Meier U, Gressner AM. Endocrine regulation of energy metabolism: review of pathobiochemical and clinical chemical aspects of leptin, ghrelin, adiponectin, and resistin. Clin Chem 2004;50:1511–25.
[2] Qi Y, Takahashi N, Hileman SM, Patel HR, Berg AH, Pajvani UB, et al. Adiponectin acts in the brain to decrease body weight. Nat Med 2004;10:524–9.
[3] Pischon T, Girman CJ, Hotamisligil GS, Rifai N, Hu FB, Rimm EB. Plasma adiponectin levels and risk of myocardial infarction in men. J Am Med Assoc 2004;291:1730–7.
[4] Wannamethee SG, Whincup PH, Lennon L, Sattar N. Circulating adiponectin levels and mortality in elderly men with and without cardiovascular disease and heart failure. Arch Intern Med 2007;167:1510–7.
[5] Kizer JR, Barzilay JI, Kuller LH, Gottdiener JS. Adiponectin and risk of coronary heart disease in older men and women. J Clin Endocrinol Metab 2008;93:3357–64.
[6] Wannamethee SG, Welsh P, Whincup PH, Sawar N, Thomas MC, Gudnarsson V, et al. High adiponectin and increased risk of cardiovascular disease and mortality in asymptomatic older men: does NT-proBNP help to explain this association? Eur J Cardiovasc Prev Rehabil 2011;18:65–71.
[7] Dekker JM, Funahashi T, Nijpels G, Pilz S, Stehouwer CD, Snijder MB, et al. Prognostic value of adiponectin for cardiovascular disease and mortality. J Clin Endocrinol Metab 2008; 93:1489–96.
[8] Wannamethee SG. Adiponectin and cardiovascular risk prediction: can the ambiguities be resolved? Nutr Metab Cardiovasc Dis 2008;18:581–4.
[9] Kizer JR, Arnold AM, Strotmeyer ES, Ives DG, Cushman M, Ding J, et al. Change in circulating adiponectin in advanced old age: determinants and impact on physical function and mortality. The Cardiovascular Health Study All Stars Study. J Gerontol A Biol Sci Med Sci 2010;65:1208–14.
[10] Hozawa A, Sugawara Y, Tomata Y, Kakizaki M, Tsuboya T, Ohmori-Matsuda K, et al. Relationship between serum adiponectin levels and disability-free survival among community-dwelling elderly individuals: the Tsurugaya Project. J Gerontol A Biol Sci Med Sci 2012;67:530–6.
[11] Rantanen T, Volpato S, Ferrucci L, Heikkinen E, Fried LP, Guralnik JM. Handgrip strength and cause-specific and total mortality in older disabled women: exploring the mechanism. J Am Geriatr Soc 2003;51:636–41.

[12] Guo H, Niu K, Monma H, Kobayashi Y, Guan L, Sato M, et al. Association of Japanese dietary pattern with serum adiponectin concentration in Japanese adult men. Nutr Metab Cardiovasc Dis 2012;22:277–84.
[13] Carlson RV, Boyd KM, Webb DJ. The revision of the Declaration of Helsinki: past, present and future. Br J Clin Pharmacol 2004;57:695–713.
[14] Bassey EJ, Short AH. A new method for measuring power output in a single leg extension: feasibility, reliability and validity. Eur J Appl Physiol Occup Physiol 1990;60:385–90.
[15] Craig CL, Marshall AL, Sjostrom M, Bauman AE, Booth ML, Ainsworth BE, et al. International physical activity questionnaire: 12-country reliability and validity. Med Sci Sports Exerc 2003;35:1381–95.
[16] Ishikawa-Takata K, Tabata I, Exercise, Activity Physical. Reference for health promotion 2006 (EPAR2006). J Epidemiol 2007;17:177.
[17] Sasaki S. Serum biomarker-based validation of a brief-type self-administered diet history questionnaire for Japanese subjects: a research for assessment of nutrition and dietary habit in "Kenko Nippon 21". Tokyo, Japan: The Study Group of Ministry of Health, Labor and Welfare of Japan; 2005. p. 10–42 [in Japanese].
[18] Fukuda K, Kobayashi S. A study on a self-rating depression scale (author's transl). Seishin Shinkeigaku Zasshi 1973;75: 673–9 [in Japanese].
[19] Fountoulakis KN, Iacovides A, Samolis S, Kleanthous S, Kaprinis SG, St Kaprinis G, et al. Reliability, validity and psychometric properties of the Greek translation of the Zung depression rating scale. BMC Psychiatry 2001;1:6.
[20] Alberti KG, Eckel RH, Grundy SM, Zimmet PZ, Cleeman JI, Donato KA, et al. Harmonizing the metabolic syndrome: a joint interim statement of the International Diabetes Federation Task Force on Epidemiology and Prevention; National Heart, Lung, and Blood Institute; American Heart Association; World Heart Federation; International Atherosclerosis Society; and International Association for the Study of Obesity. Circulation 2009;120:1640–5.
[21] Une K, Takei YA, Tomita N, Asamura T, Ohrui T, Furukawa K, et al. Adiponectin in plasma and cerebrospinal fluid in MCI and Alzheimer's disease. Eur J Neurol 2011;18:1006–9.
[22] Jimenez-Pavon D, Ortega FB, Valtuena J, Castro-Pinero J, Gomez-Martinez S, Zaccaria M, et al. Muscular strength and markers of insulin resistance in European adolescents: the HELENA Study. Eur J Appl Physiol 2012;112:2455–65.
[23] Martinez-Gomez D, Eisenmann JC, Gomez-Martinez S, Veses A, Romeo J, Veiga OL, et al. Associations of physical activity and fitness with adipocytokines in adolescents: the AFINOS Study. Nutr Metab Cardiovasc Dis 2012;22:252–9.
[24] Ingelsson E, Arnlov J, Zethelius B, Vasan RS, Flyvbjerg A, Frystyk J, et al. Associations of serum adiponectin with skeletal muscle morphology and insulin sensitivity. J Clin Endocrinol Metab 2009;94:953–7.
[25] Pisto P, Santaniemi M, Turpeinen JP, Ukkola O, Kesaniemi YA. Adiponectin concentration in plasma is associated with muscle fiber size in healthy middle-aged men. Scand J Clin Lab Invest 2012;72:395–402.
[26] Verdijk LB, Snijders T, Beelen M, Savelberg HH, Meijer K, Kuipers H, et al. Characteristics of muscle fiber type are predictive of skeletal muscle mass and strength in elderly men. J Am Geriatr Soc 2010;58:2069–75.
[27] Frontera WR, Meredith CN, O'Reilly KP, Knuttgen HG, Evans WJ. Strength conditioning in older men: skeletal muscle hypertrophy and improved function. J Appl Physiol 1988;64: 1038–44.
[28] Matsushita K, Yatsuya H, Tamakoshi K, Wada K, Otsuka R, Zhang HM, et al. Inverse association between adiponectin and C-reactive protein in substantially healthy Japanese men. Atherosclerosis 2006;188:184–9.
[29] Schaap LA, Pluijm SM, Deeg DJ, Visser M. Inflammatory markers and loss of muscle mass (sarcopenia) and strength. Am J Med 2006;119:526.e9–526.e17.
[30] Monma Y, Niu K, Iwasaki K, Tomita N, Nakaya N, Hozawa A, et al. Dietary patterns associated with fall-related fracture in elderly Japanese: a Population Based Prospective Study. BMC Geriatr 2010;10:31.
[31] Frystyk J, Berne C, Berglund L, Jensevik K, Flyvbjerg A, Zethelius B. Serum adiponectin is a predictor of coronary heart disease: a population-based 10-year follow-up study in elderly men. J Clin Endocrinol Metab 2007;92:571–6.
[32] Bajaj M, Suraamornkul S, Piper P, Hardies LJ, Glass L, Cersosimo E, et al. Decreased plasma adiponectin concentrations are closely related to hepatic fat content and hepatic insulin resistance in pioglitazone-treated type 2 diabetic patients. J Clin Endocrinol Metab 2004;89:200–6.
[33] Hanley AJG, Williams K, Stern MP, Haffner SM. Homeostasis model assessment of insulin resistance in relation to the incidence of cardiovascular disease — the San Antonio Heart Study. Diabetes Care 2002;25:1177–84.
[34] Newman AB, Kupelian V, Visser M, Simonsick EM, Goodpaster BH, Kritchevsky SB, et al. Strength, but not muscle mass, is associated with mortality in the health, aging and body composition study cohort. J Gerontol A Biol Sci Med Sci 2006;61:72–7.

35th Annual International Conference of the IEEE EMBS
Osaka, Japan, 3 - 7 July, 2013

Hemodynamic Effects of Pressure-Volume Relation in the Atrial Contraction Model on the Total Artificial Heart Using Centrifugal Blood Pumps.

Takuya Shiga, Takehito Kuroda, Yusuke Tsuboko, Hidekazu Miura,
Yasuyuki Shiraishi, and Tomoyuki Yambe, *Member, IEEE*

***Abstract*— Hemodynamic effects of atrial contraction with centrifugal pump type total artificial heart is unknown. In this study, we simulated an atrial contraction in a mock model. By the driving condition with higher pressure in the mock atrial model, the load during atrial contraction increased. Based on these findings, we examined atrial contraction in the animal using adult goats. Prior to the measurement, we installed a centrifugal-type ventricular assist device (VADs), and then clamped both ventricles. We measured the hemodynamic data without ventricular contractile functions in order to obtain the effect of atrial contraction on hemodynamics under the condition of the total artificial heart (TAH) circulatory support model. We could estimate the heart rate by revolution number and voltage of pumps. There might be a possibility that we could regulate autonomic nervous response with the control of cardiac output.**

I. Introduction

The number of Japanese outpatients with left ventricular dysfunction is predicted to increase gradually with population growth and to be reached 1.3 million by 2030 [1]. There were 5.8 million people with heart failure (HF) in the United States in 2006 [2], and there were 0.2 million people with end-stage HF. The gold standard therapy for end-stage HF patient is the cardiac transplantation [3]. However, there are many cases that cannot get the cardiac transplantation because their age, complication or changing condition drops them from indication. VAD is the effective therapy for them [4]. In the United States and European countries, the purpose of VAD has changed rapidly from bridge-to-transplantation (BTT) to destination therapy (DT) [5]. Subsequent BiVAD installation may be necessary in about 5% of patients with VAD due to not only the left heart failure but also the right heart failure [6]. Total artificial heart (TAH) systems will be one of the viable alternatives, although there are functional differences between BiVADs and TAHs from the right or left ventricular physiological point of view.

As for the pulsatile TAH, which is commercially available at this moment, some critical issues on thrombosis and its durability are arising by the time of BTT, which is usually expected to be performed within 3 months [7]. Based on clinical evidences, the long-term follow up on the continuous-flow type VADs formed acceptable results for 2 years of awaiting period followed by DT [8]. Furthermore, Frazier, et al reported a trial with a continuous-flow TAH using axial blood pump [9].

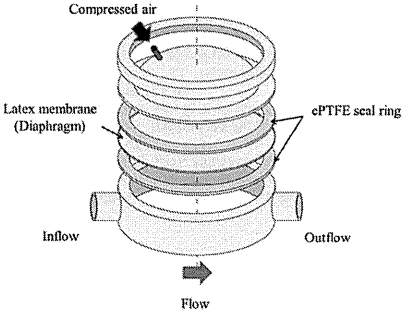

Fig. 1. Schematic illustration of the atrium model.

In this study, we designed a TAH support system which consisted of two centrifugal VAD devices. We preserved the functioning atriums. While some reports suggest that the atrial contraction may partly contribute to cardiac output promotion of the natural heart, the effect of atrial contraction for VAD with centrifugal pump system has not been known. Then, firstly, we performed simulation studies for the effectiveness of atrial contraction with a centrifugal-type TAH support in the mechanical circulatory system. Secondly, we examined the effectiveness of atrial contraction during the functional TAH support in the animal experiments.

Takuya Shiga is with Department of Anesthesiology and Perioperative Medicine, Tohoku University Graduate School of Medicine, 2-1 Seiryo-machi, Aoba-ku, Sendai 980-8575 Japan (corresponding author to provide phone:+81-22-717-7321; fax:+81-22-717-7325; e-mail: t-shiga@med.tohoku.ac.jp).

Takehito Kuroda is with Tohoku University School of Medicine, 2-1 Seiryo-machi, Aoba-ku, Sendai 980-8575 Japan (e-mail: take.tk10@gmail.com).

Yusuke Tsuboko is with Graduate School of Biomedical Engineering, Tohoku University, 4-1 Seiryo-machi, Aoba-ku, Sendai 980-8575 Japan (e-mail: tsuboko@idac.tohoku.ac.jp).

Hidekazu Miura is with Department of Medical Engineering and Cardiology, Institute of Development, Aging and Cancer, Tohoku University, 4-1 Seiryo-machi, Aoba-ku, Sendai 980-8575 Japan (e-mail: h.miura@idac.tohoku.ac.jp).

Yasuyuki Shiraishi is with Department of Medical Engineering and Cardiology, Institute of Development, Aging and Cancer, Tohoku University, 4-1 Seiryo-machi, Aoba-ku, Sendai 980-8575 Japan (e-mail: shiraishi@idac.tohoku.ac.jp).

Tomoyuki Yambe is with Department of Medical Engineering and Cardiology, Institute of Development, Aging and Cancer, Tohoku University, 4-1 Seiryo-machi, Aoba-ku, Sendai 980-8575 Japan (e-mail: yambe@idac.tohoku.ac.jp).

978-1-4577-0216-7/13/$26.00 ©2013 IEEE

II. Mock Hemodynamic Examination

A. Atrium Model

We developed an atrium model which was capable of representing atrial contraction in the mock circulatory system. The chamber of the atrial model was made of an acrylic cylinder, the inner and outer diameters of which were 100 and 120mm, respectively. A dome-shaped acrylic casing was mounted on the cylinder, and a natural rubber membrane (Nippon Elaster, Ltd., Japan) was sandwiched, which separated the fluid and air chambers. Average height of the fluid chamber was 38 mm, and the maximum volume was designed to be 300mL. We used ePTFE gasket sheets (Japan Gore, Ltd., Japan) for sealing between the casing and cylinder. The schematic illustration of the atrial model developed in this study was shown in Fig. 1.

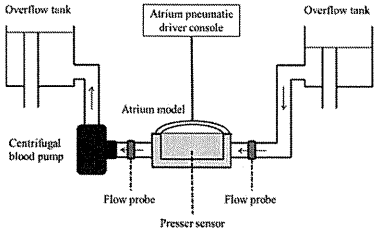

Fig. 2. Schematic illustration of the atrial mock circuit.

B. Controlling of Atrial Contraction Model

We also developed a pneumatic driver for the active contraction in the atrial model. Pressure in the upper air chamber was supplied and controlled by a regulator. We could control the period and timing of the contraction signal for the atrial model by a pulse controller using a microcontroller board (Arduino, MEGA 2590 R3, Italy). The system achieved the synchronous motion with ventricular driving signals in the atrial model, as well as its pumping rate and % systolic duration. During the systolic or diastolic phase, we supplied only pressure along with the passive dilatation of the atrial membrane without vacuum pressure.

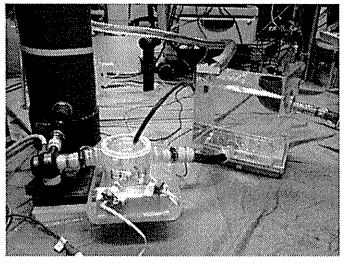

Fig. 3. Whole view of the atrial mock circuit.

C. A mock Circulatory System with the Contractive Atrium

We developed the simulator representing natural hemodynamics to examine the effects of atrial contraction on the function of the centrifugal pump type VAD. Figure 2 shows a schematic illustration of the atrial mock test circuit. The mock system consisted of reservoir tanks, overflow tanks, a VAD pump (EVAHEART™, Sun Medical Technology Research Corp., Japan) [10], the atrium model, the pneumatic driver. We measured pressure and flow rate at the pressure port and at the inflow and outflow portions of the atrium. Electromagnetic flow probes (Nihon Kohden, Japan) were used and the change of atrial volume was calculated by these data. We used 0.9% normal saline as circulatory media. As shown in Fig. 3, we installed the VAD pump at the outflow portion of the atrium in the mock circuit. We compared the pumping function of the VAD under the two different driving/loading conditions, which simulated the systemic or pulmonary pressure loadings. We set the revolution number of the VAD under the driving conditions in the right or left heart circulations to be 1400 and 2400 rpm, respectively. We selected the pressure heads by changing the afterload as 80 – 100, and 10–30 mmHg for the left and right heart circulation, respectively. We varied the driving pressure in the atrial model from 5 to 20 mmHg in order to change the contraction force on the atrial membrane.

D. Results

Figure 4 shows pressure waveform obtained with the atrial contraction in the mock circulatory system. As shown in Fig. 5, the additional flow velocity peaks could be derived in the forward flow, whereas the inflow exhibited back flow from the atrial model.

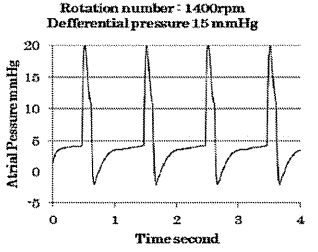

Fig. 4. Atrial pressure waveform in the mock loop.

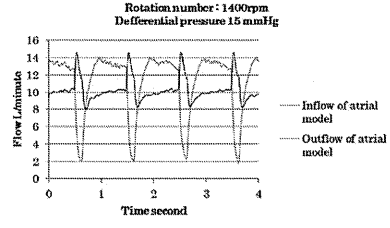

Fig. 5. Inflow and outflow waveforms obtained at the atrial model in the mock test.

Figure 6 shows the relationships between pressure and volume (P-V) calculated at the atrial model during the simulation of right heart circulation with the centrifugal VAD under the condition of active contraction of the atrial model. Figure 7 shows these P-V relations obtained from the mock circulatory system simulating the left heart circulatory conditions. We observed similar characteristics in both P-V loops under the different loading conditions in respect to the left or right ventricular support. The changes in the atrial stroke volume were 20mL, and the atrial pressures were 20/-2mmHg under the condition of 15mmHg supply at the atrium. These hemodynamic data resembled the natural heart functions. We investigated the negative pressure changes in the diastolic phase. By the elevation of driving pressure at the atrial model, the atrial pressure increased. There was no discernible difference in the cardiac output against the changes in the atrial driving pressure.

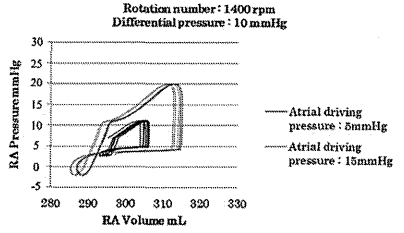

Fig. 6. Pressure-volume relations obtained in the right atrial model in the mock loop.

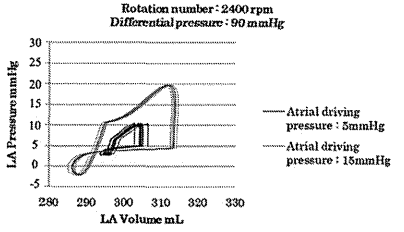

Fig. 7. Pressure-volume relations obtained in the left atrial model in the mock loop.

III. Animal Experiments

Based on the experimental results in the mock examination, we performed animal experiments. All the animal experimental procedure and related activities were reviewed and permitted by the Institutional Animal Use and Care Committee of the Tohoku University.

A. Animal Experiments

We examined the atrial contraction effects under the centrifugal blood pump support on hemodynamics in animal experiments using adult goats, which weighed 37.2–50.0kg. The heart was exposed by the left thoracotomy under general anesthesia. Prior to the measurement, we set up the functional TAH circulation by placing the clamps on both ventricles. Two centrifugal blood pumps (EVAHEART^{TM}) were installed for the systemic and the pulmonary circulation. We made end-to side anastomosis by the ePTFE vascular grafts to the descending aorta or the pulmonary artery, and connected to atriums via the atrial appendage for the inflow of each pump. Then we clamped both ventricles. Figure 9 shows overview of the functional TAH circulatory system. Then we examined the hemodynamic changes. We measured the ECG, the aortic, left atrial, right atrial, and pulmonary artery pressures. We also obtained the pump flow data by using two ultrasonic probes (ME16/19PXN, Transonic Systems Ltd., USA), and the revolution number and voltage in each pump simultaneously.

B. Results

Figure 8 shows an example of the hemodynamics obtained from the goat, which weighed 50.0kg. Atrial contraction wave in the ECG exhibited the synchronization with the atrial pressure changes. Hemodynamic parameters were obtained as follows: a) the right pump; the revolution number was 1250rpm, the pump flow was 2.51L/min, the atrial pressure was 19 / 6mmHg, the pulmonary artery pressure was 27mmHg, b) the left pump; 2370rpm, 2.21L/min, 30 / 10mmHg, respectively, and the arterial pressure was 105mmHg. As shown in the Fig. 8, we recognized the aortic and pulmonary arterial pressure increase by the atrial contraction, which was represented by P wave in the ECG, under the centrifugal blood pump support. By the blood flow through the pumps, the voltage and revolution number in each pump decreased during the atrial contraction phase under the pump control condition of the constant rotational speeds. We observed changes in responsive power consumption in each pump according to the variation of the flow velocity across the pumps by the atrial contractions.

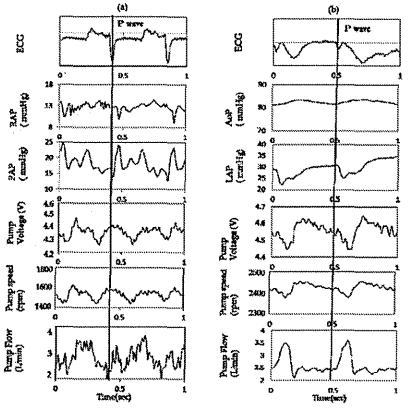

Fig. 8. Changes in parameters by the atrial contraction with the functional TAH support using two centrifugal blood pumps; (a) the right heart , and (b) the left heart circulations. ECG, electrocardiogram; RAP, right atrial pressure; PAP, pulmonary arterial pressure; AoP, aortic pressure; LAP, left atrial pressure.

IV. Discussion

In the mock test, we observed negative pressure changes during the active assistance by the atrial model. The elastic diaphragm might cause a kickback function in diastolic phase. Although the maximum pump flow rate was elevated by the atrial contraction, there was no discernible difference in the cardiac output due to the reciprocating flow at the atrial inflow portion in this mock experiment. As for the natural inflow characteristics of the atriums which are connected to veins, the impedance between the atriums and inflow vessels may change the flow characteristics consequently. We observed instantaneous flow velocity drops in the inflow waveforms as shown in Fig. 5. As the limitation of the mock test was in the calibration of the impedance matching of inflow of the atrium model was calibrated, the forward flow might increase under the optimized conditions with the centrifugal TAH, and we must update the atrium model to more sophisticated simulation of the natural heart.

We obtained the atrial contraction effects across the low-pressure loss centrifugal pump, such as EVAHEART^{TM} in the animal experiment without ventricular functions. During the functional TAH application, there was a difference between the right and left cardiac outputs. To determine the flow distribution patterns, we focused on venous return, coronary perfusion and other circulatory parameters. By monitoring pump power consumption, we might the atrial contraction non-invasively as well as the heart rate. We will be able to build a new feedback control and a co-pulse control to promote or lower the pump flow [11]. Leaving atriums may also be effective in preventing from sucking as a blood reservoir. Patients with chronic atrial fibrillation will be excluded explicitly in the purpose of those applications of pump control.

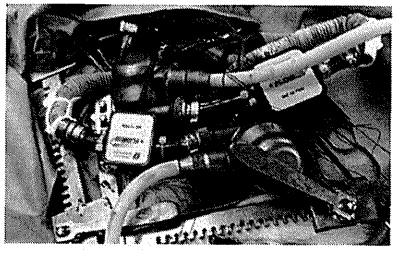

Fig. 9. Overview of the functional total artificial heart circulatory system in animal.

V. Conclusion

We measured hemodynamic effects of atrial contraction with two centrifugal type artificial hearts for the application as the functional TAH support. We examined the atrial contractile functions by using an originally designed atrial model as well as in animal experiments using goats. The atrial contraction might contribute to the increase of pulsatility during the centrifugal type TAH application without ventricular contractile functions.

References

[1] Y. Okura, M. M. Ramadan, Y. Ohno, et al., "Impending Epidemic Future Projection of Heart Failure in Japan to the Year 2055," *Circ J*, vol. 72, pp. 489–491, 2011.

[2] V. L. Roger, A. S. Go, D. M. Lloyd-Jones, et al., "Heart Disease and Stroke Statistics--2011 Update: A Report From the American Heart Association," *Circulation*, vol. 123, pp. e18–e209, 2010.

[3] M. R. Mehra, J. Kobashigawa, R. Starling, et al., "Listing criteria for heart transplantation: International Society for Heart and Lung Transplantation guidelines for the care of cardiac transplant candidates--2006," *J Heart Lung Transplant* : the official publication of the International Society for Heart Transplantation, vol. 25, pp. 1024–42, Sep. 2006.

[4] E. A. Rose, A. C. Gelijns, A. J. Moskowitz, et al., "Long-term use of a left ventricular assist device for end-stage heart failure," *N Engl J Med*, vol. 345, pp. 1435–43, Nov. 2001.

[5] J. K. Kirklin, D. C. Naftel, F. D. Pagani, et al., "Long-term mechanical circulatory support (destination therapy): on track to compete with heart transplantation?," *J Thorac Cardiovasc Surg*, vol. 144, pp. 584-603; discussion 597–8, Sep. 2012.

[6] J. K. Kirklin, D. C. Naftel, R. L. Kormos, et al., "The Fourth INTERMACS Annual Report: 4,000 implants and counting," *J Heart Lung Transplant* : the official publication of the International Society for Heart Transplantation, vol. 31, pp. 117–26, Feb 2012.

[7] K. Friedline and P. Hassinger, "Total artificial heart freedom driver in a patient with end-stage biventricular heart failure," *AANA journal*, vol. 80, pp. 105–12, Apr 2012.

[8] M. S. Slaughter, J. G. Rogers, C. A. Milano, et al., "Advanced heart failure treated with continuous-flow left ventricular assist device," The New England journal of medicine, vol. 361, pp. 2241–51, Dec 3 2009.

[9] O. H. Frazier, W. E. Cohn, E. Tuzun, et al., "Continuous-flow total artificial heart supports long-term survival of a calf," *Tex Heart Inst J*, vol. 36, pp. 568–74, 2009.

[10] K. Yamazaki, S. Saito, S. Kihara, et al., "Completely pulsatile high flow circulatory support with a constant-speed centrifugal blood pump: mechanisms and early clinical observations," *Gen Thorac Cardiovasc Surg*, vol. 55, pp. 158–62, Apr 2007.

[11] A. Tanaka, M. Yoshizawa, K. Abe, et al., "Open-loop analysis of transfer characteristics from blood pressure to heart rate using an effectively total artificial heart," *J Artif Organs*, vol. 28, pp. 109–14, Jan 2004.

Mutation of the Mg^{2+} Transporter *SLC41A1* Results in a Nephronophthisis-Like Phenotype

Toby W. Hurd,* Edgar A. Otto,† Eikan Mishima,‡ Heon Yung Gee,† Hana Inoue,§ Masato Inazu,‖ Hideomi Yamada,¶ Jan Halbritter,† George Seki,¶ Masato Konishi,§ Weibin Zhou,† Tsutomo Yamane,** Satoshi Murakami,†† Gianluca Caridi,‡‡ Gianmarco Ghiggeri,‡‡ Takaaki Abe, ‡§§‖‖ and Friedhelm Hildebrandt†§§‖‖‖

*MRC Human Genetics Unit, Institute of Genetics and Molecular Medicine, University of Edinburgh, Edinburgh, United Kingdom; †Department of Pediatrics, §§§Department of Human Genetics, and ‖‖‖Howard Hughes Medical Institute, University of Michigan, Ann Arbor, Michigan; ‡Department of Clinical Biology, Tohoku University Graduate School of Medicine, Miyagi, Japan; §Department of Physiology and ‖Institute of Medical Science, Tokyo Medical University, Tokyo, Japan; ¶Department of Internal Medicine, Faculty of Medicine, University of Tokyo, Tokyo, Japan; **Graduate School of Nanobioscience, Yokohama City University, Yokohama, Japan; ††Graduate School of Bioscience & Biotechnology, Tokyo Institute of Technology, Yokohama, Japan; ‡‡Istituto G. Gaslini, Genova, Italy; §§Division of Medical Science, Tohoku University Graduate School of Biomedical Engineering, Miyagi, Japan; and ‖‖Department of Clinical Biology and Hormonal Regulation, Tohoku University Graduate School of Medicine, Miyagi, Japan.

ABSTRACT

Nephronophthisis (NPHP)-related ciliopathies are recessive, single-gene disorders that collectively make up the most common genetic cause of CKD in the first three decades of life. Mutations in 1 of the 15 known *NPHP* genes explain less than half of all cases with this phenotype, however, and the recently identified genetic causes are exceedingly rare. As a result, a strategy to identify single-gene causes of NPHP-related ciliopathies in single affected families is needed. Although whole-exome resequencing facilitates the identification of disease genes, the large number of detected genetic variants hampers its use. Here, we overcome this limitation by combining homozygosity mapping with whole-exome resequencing in a sibling pair with an NPHP-related ciliopathy. Whole-exome capture revealed a homozygous splice acceptor site mutation (c.698G>T) in the renal Mg^{2+} transporter *SLC41A1*. This mutation resulted in skipping of exon 6 of *SLC41A1*, resulting in an in-frame deletion of a transmembrane helix. Transfection of cells with wild-type or mutant SLC41A1 revealed that deletion of exon 6 completely blocks the Mg^{2+} transport function of SLC41A1. Furthermore, in normal human kidney tissue, endogenous SLC41A1 specifically localized to renal tubules situated at the corticomedullary boundary, consistent with the region of cystogenesis observed in NPHP and related ciliopathies. Last, morpholino-mediated knockdown of *slc41a1* expression in zebrafish resulted in ventral body curvature, hydrocephalus, and cystic kidneys, similar to the effects of knocking down other NPHP genes. Taken together, these data suggest that defects in the maintenance of renal Mg^{2+} homeostasis may lead to tubular defects that result in a phenotype similar to NPHP.

J Am Soc Nephrol 24: 967–977, 2013. doi: 10.1681/ASN.2012101034

Rare CKDs make up the majority of CKD cases treated within long-term dialysis and renal transplantation programs in the first three decades of life but are notoriously difficult to diagnose.[1] Rare recessive mutations cause chronic diseases that often require hospitalization.[2] However, half of their single-gene causes are still unknown (http://omim.org/statistics/entries). Because recessive single-gene mutations directly represent the disease cause, gene identification offers a powerful approach to revealing disease mechanisms. Furthermore, because recessive mutations predominantly convey loss of function, recessive single-gene defects can be transferred directly into animal models to study the related disease mechanisms and to screen for small molecules as possible treatment modalities.

Received October 29, 2012. Accepted February 22, 2013.

T.W.H. and E.A.O. contributed equally to this work.

Published online ahead of print. Publication date available at www.jasn.org.

Correspondence: Dr. Friedhelm Hildebrandt, 8220C MSRBIII, 1150 West Medical Center Drive, Ann Arbor, MI 48109-5646. Email: fhilde@umich.edu

Nephronophthisis (NPHP), a recessive cystic kidney disease, is the most frequent genetic cause of CKD in the first three decades of life. NPHP-related disorders are recessive single-gene disorders that affect kidney, retina, brain, and liver by prenatal-onset dysplasia or by organ degeneration and fibrosis in early adulthood.[3] On ultrasonography, these conditions are characterized by increased echogenicity and cyst formation at the corticomedullary junction in small or normal-sized kidneys.[4] Renal histology exhibits a characteristic triad of renal corticomedullary cysts, tubular basement membrane disruption, and tubulointerstitial infiltrations.[5] Regarding renal, retinal, and hepatic involvement, there is phenotypic overlap of NPHP-related disorders with Bardet-Biedl syndrome and Alstrom syndrome.[6] Identification of recessive mutations in 15 different genes (*NPHP1–NPHP15*)[7–18] revealed that the encoded proteins share localization at the primary cilia-centrosomes complex, which characterizes them as ciliopathies.[3,19] However, the 15 known *NPHP* genes explain less than 50% of all cases with NPHP-related disorders, indicating that many of the single-gene causes of these conditions are still elusive.[20]

The finding that some of the more recently identified genetic causes of NPHP-related disorders are exceedingly rare necessitates a strategy to identify novel single-gene causes of these conditions in single affected families.[15] In this context, the new method of whole exome capture with consecutive massively parallel sequencing (here called whole exome resequencing [WER]) theoretically offers a powerful approach toward gene identification in rare recessive diseases. However, the utility of WER is hampered by the large number of novel genetic variants that result from whole exome sequencing in any given individual.[18,21] To overcome this limitation of WER, we developed a strategy that combines WER with homozygosity mapping.[18] Using this approach, we have identified mutation of the renal magnesium transporter gene *SLC41A1* as a novel genetic cause of disease that phenocopies NPHP-related conditions clinically, ultrasonographically, and histologically.

RESULTS

Identification of Mutation of *SLC41A1* in Family F438

To identify additional causative mutations for NPHP-related disorders, we performed WER in a consanguineous Italian family (F438) with an apparent NPHP-related disorder phenotype (Figure 1A). In this large family, two siblings born from first cousins (IV1 and IV2) displayed the unusual association of apparent NPHP with bronchiectasis.

Patient IV2 had had frequent episodes of fever, coughing, and respiratory infections since the first month of life, and chest radiography demonstrated the persistence of inflammatory infiltrates in the lung. High-resolution computerized tomography revealed bronchiectasis, and fiberoptic bronchoscopy showed reddening of the bronchial mucosa with purulent secretion. Evaluation of bronchoalveolar lavage showed a marked increase in the percentage of neutrophils and the presence of *Pseudomonas aeruginosa*. At age 8 years, the patient was referred to the Nephrology Department because of observed polyuria and polydipsia. Initial urine analysis revealed low urine osmolarity (380 mOsmol/kg in fresh morning urine), and blood analysis displayed renal insufficiency with serum creatinine levels of 2.37 mg/dl. Renal ultrasonography showed bilateral irregular echogenicity, with both kidneys decreased in size (Figure 1B). Percutaneous renal biopsy showed periglomerular fibrosis, tubular ectasia, tubular basement membrane disruption, and tubulointerstitial infiltrations (Figure 1C). On the basis of these clinical findings, a diagnosis of NPHP was proposed. The patient underwent peritoneal dialysis at age 9 years before undergoing kidney transplantation at age 10.

Patient IV1, like his sibling, had had a history of fever, coughing, and respiratory infections since the first month of life. IV1 also presented with polyuria and polydipsia with low urine osmolarity (420 mOsmol/kg) and serum creatinine level of 1.5 mg/dl at 5 years of age. Renal biopsy and renal ultrasonography showed similar findings as for patient IV2 (Figure 1B). Progression of renal damage led to ESRD at age 10 and initiation of peritoneal dialysis.

Patient IV3 is a first-line cousin of siblings IV1 and IV2. She presented with chronic bronchitis and bronchiectasis at age 6 years. However, by age 11 no signs of polyuria or polydipsia were present and results of blood and urine analysis were normal. In addition, renal ultrasonography revealed no abnormalities in kidney size or structure.

Homozygosity mapping performed on patient IV1 yielded eight homozygosity peaks (Figure 2A). By WER, we detected four homozygous variants (Supplemental Table 1) whose segregation pattern fit a recessive mode of inheritance. Of these four variants, only the variant in the *SLC41A1* gene was not a known single-nucleotide polymorphism (SNP) and was absent from both the 1000 Genomes and Exome Variant Server databases (Supplemental Table 2). Furthermore, only the *SLC41A1* variant was predicted to be damaging by all four predictive tools used (Polyphen 1, Polyphen 2, MutationTaster, SIFT [Supplemental Table 2]). In addition, only two of the variants (*SLC41A1* and *ZNF224*) display strong evolutionary conservation at the mutated residue (Supplemental Table 3). Finally, the homozygous missense mutation (c.698G>T, p.G223V) in *SLC41A1* resides within an evolutionary conserved exonic splice acceptor site in exon 6 of *SLC41A1*, probably resulting in missplicing of the *SLC41A1* transcript and thus a potentially more deleterious mutation. This mutation was absent from 100 European-American healthy controls and also absent from 80 regionally matched healthy controls (G. Caridi, personal communication). These

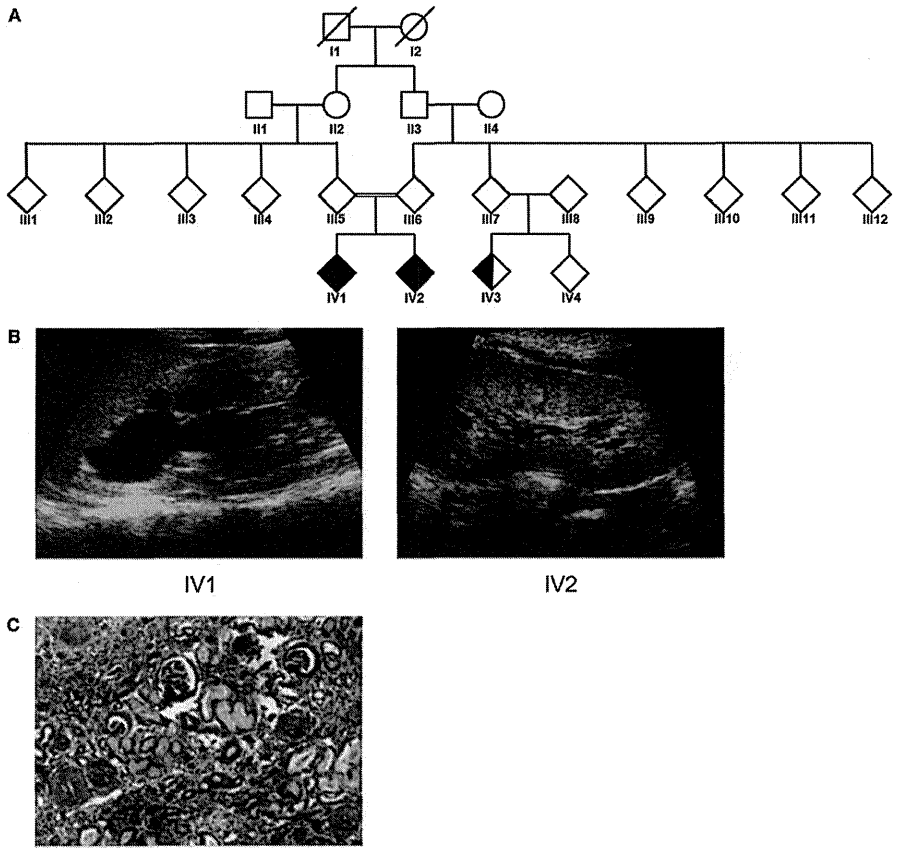

Figure 1. Renal ultrasonography and biopsy indicate characteristic hallmarks of nephronophthisis. (A) Pedigree for family F438. Individuals IV1 and IV2 display both NPHP and primary ciliary dyskinesia (shaded shapes). Individual IV3 has only primary ciliary dyskinesia (half-shaded). (B) RUS showing increased echogenicity, corticomedullary cysts, and loss of corticomedullary differentiation in patients F438-IV1 (left panel) and F438-IV2 (right panel). (C) Renal histologic findings from a renal biopsy specimen from F438-IV1 showing the characteristic triad of tubular ectasia, tubular basement membrane disruption, and tubulointerstitial infiltrations (Trichrome-Masson staining).

data together suggest that *SLC41A1* as a novel causative gene of an NPHP-related disorder phenotype (Figure 2, B and C).

SLC41A1 c.698G>T Mutation Results in Skipping of Exon 6

To test whether the c.698G>T mutation impairs normal splicing of the *SLC41A1* transcript, Epstein Barr virus (EBV)–transformed white blood cells were prepared from blood samples from both parents (III5 and III6) and the two affected siblings (IV1 and IV2). RT-PCR was performed using primers flanking exon 6 (Figure 2B) on cDNA prepared from both the EBV-transformed white blood cells. This test revealed that in both parents, one PCR product of the expected size and an additional faster-migrating PCR product was observed (Figure 2D, upper panel), consistent with the fact that both parents are heterozygous for the c.698G>T mutation. In contrast, RT-PCR on patient-derived cDNA yielded only the single faster-migrating band (Figure 2D, upper panel). Sanger sequencing

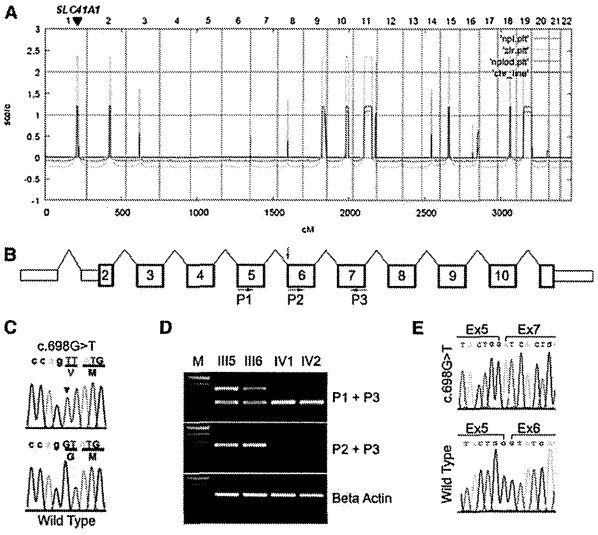

Figure 2. Recessive mutation in *SLC41A1* in family F438 identified by whole exome capture and homozygosity mapping. (A) Homozygosity profile for patient IV1. Nonparametric logarithm of odds scores were plotted over genetic distance across the genome, where chromosomal positions are concatenated from p- to q-arm (left to right). Arrowhead shows the *SLC41A1* locus. (B) Diagram of the human *SLC41A1* gene showing exon number and primer locations. Red arrow shows position of the c.698G>T splice acceptor site mutation. (C) Sanger-sequencing confirmation of the c.698G>T mutation in *SLC41A1*. Altered nucleotide and amino acid change are given above the sequence trace. WT control sequence and trace are shown below the mutated sequence. Codon triplets are underlined to indicate reading frame. Noncoding sequence is in lower case. Mutated nucleotide is denoted by arrowhead. (D) RT-PCR was performed on RNA from lymphoblastoid cells prepared from parents (III5 and III6) and affected siblings (IV1 and IV2) using the primers indicated. Positions of primers is indicated in B. M, 100-bp DNA ladder. (E) Sanger sequencing of the fast and slow migrating RT-PCR products (primers P1 + P3) revealed that the c.698G>T mutation results in skipping of exon 6 (upper trace).

of this faster-migrating band revealed that it arises from skipping of *SLC41A1* exon6 (Figure 2E). Consistent with this observation, further RT-PCR using a forward primer designed against exon 6 (P2; Figure 2B), revealed no detectable PCR product in the two affected siblings but did show a PCR product of the expected size in the two parents (Figure 2D, middle panel). Together, these data demonstrate that the c.698G>T mutation results in missplicing of the *SLC41A1* transcript.

SLC41A1 c.698G>T Mutation Results in Abrogated Protein Expression

The *SLC41A1* mutations that results in skipping of exon 6 is predicted to result in an in-frame deletion of a transmembrane domain. We next tested whether this deletion abrogates expression of SLC41A1. Western blotting of protein lysates generated from both parental and patient-derived cell lines revealed almost complete loss of SLC41A1 expression in the two affected siblings (Figure 3A).

Mutant SLC41A1 Traffics to Cell Surface

We next tested whether the mutated form of SLC41A1 can traffic in a similar fashion as the WT protein. An amino-terminal enhanced green fluorescent protein (EGFP)–tagged SLC41A1 expression construct was generated by cloning the full-length (WT) human SLC41A1 open-reading frame into a mammalian expression vector. In addition, an expression construct with the residues encoded by *SLC41A1* exon 6 deleted was cloned from patient-derived cDNA (dEx6). Transfection of the WT and mutant constructs into the MDCKII renal epithelial cell line revealed that both targeted to the basolateral membrane and that the mutant localization was indistinguishable from WT (Figure 3B). Furthermore, using a cell-surface biotinylation assay in which HEK293 cells were transfected with WT or mutant (dEx6) FLAG-tagged SLC41A1, neutravidin pulldown revealed that both the WT and mutant SLC41A1 are trafficked to the cell surface (Figure 3C). These data suggest that the in-frame deletion of exon 6 does not affect the normal trafficking of SLC41A1.

Deletion of *SLC41A1* Exon 6 Results in Loss of Magnesium Transport Activity of SLC41A1

Because the in-frame deletion of exon6 did not appear to perturb the normal trafficking of SLC41A1, we next sought to address whether the magnesium-transporting ability of SLC41A1 might be compromised by this deletion. In cells transfected with WT SLC41A1, basal free intracellular Mg^{2+} ($[Mg^{2+}]_i$) was, on average, 1.12±0.06 mM (n=20), which was significantly higher than that of mock transfected cells (0.81±0.02 mM, n=20). The average basal $[Mg^{2+}]_i$ of mutant transfected (ΔE6) cells, 0.87±0.04 (n=33), was very similar to that of mock cells (Figure 3D). To examine the Mg^{2+} transport activity, cells were exposed to high Mg^{2+}, low Na^+ solution (Mg^{2+} influx). A 15-minute exposure to high Mg^{2+}, low Na^+ solution resulted in a robust elevation of $[Mg^{2+}]_i$ in WT cells, whereas only small increases in $[Mg^{2+}]_i$ were observed in mock and ΔE6 cells

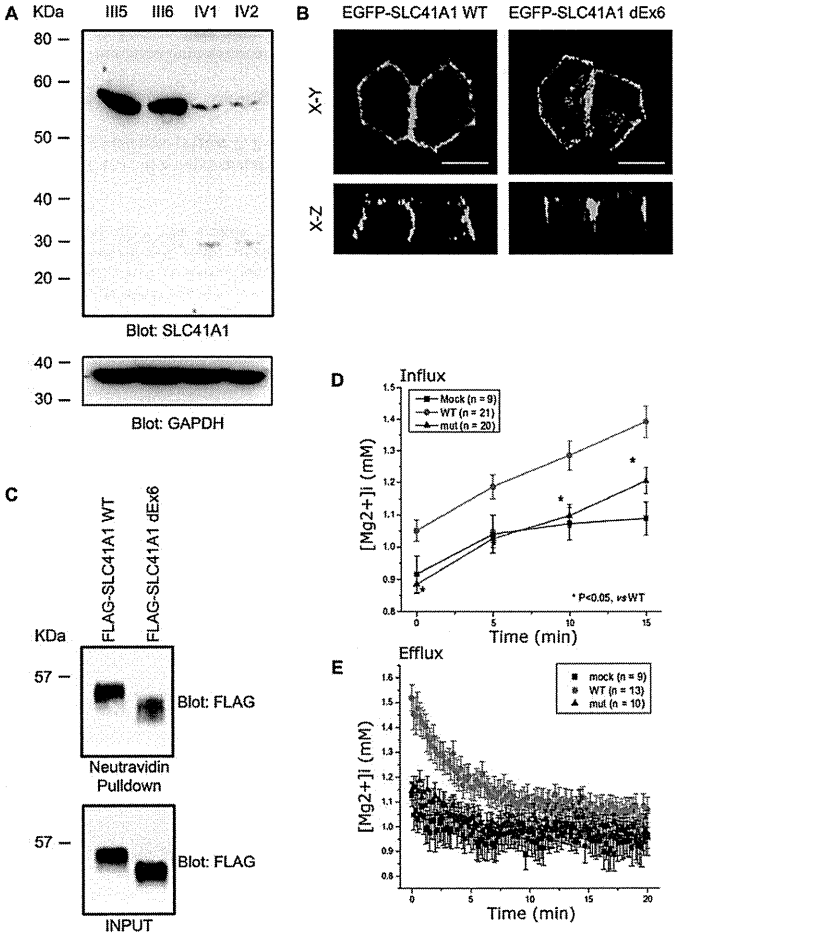

Figure 3. The c.698G>T mutation results in reduced expression and loss of function of SLC41A1. (A) Western blot of lysates prepared from parents (III5 and III6) and affected siblings (IV1 and IV2) showing decreased expression of SLC41A1 in affected siblings. Anti–glyceraldehyde 3-phosphate dehydrogenase (GAPDH) Western blot was used as loading control. (B) EGFP-tagged WT SLC41A1 and SLC41A1 lacking exon 6 (dEx6) were transiently transfected into MDCKII cells. Cells were fixed and EGFP fluorescence captured by confocal microscopy. (C) HEK293 cells transiently transfected with WT or dEx6 FLAG-tagged SLC41A1 were biotinylated at the cell surface before lysis. Cell lysates were then subjected to pulldown with neutravidin beads before SDS-PAGE and Western blotting with the indicated antibodies. (D) HEK293 cells were transfected with empty vector (MOCK) WT or dEx6 EGFP-SLC41A1 before loading with mag-fura2-AM. To measure magnesium influx, cells were exposed to high Mg^{2+}, low Na^{+} solution, and radiometric fluorescent images were collected to determine intracellular $[Mg^{2+}]$. (E) To measure magnesium efflux, cells were treated as above and then switched into magnesium-free media, and radiometric fluorescent images were collected to determine intracellular $[Mg^{2+}]$. Error bars show standard deviation.

(WT, 0.50±0.03 μM/s; mock, 0.21±0.04 μM/s; ΔE6, 0.20±0.01 μM/s). When the extracellular solution was switched to the Ca^{2+}-free Tyrode solution, $[Mg^{2+}]_i$ returned to the basal level in WT, ΔE6, and mock cells (Mg^{2+} efflux). Again, Mg^{2+} efflux rates were similar in mock cells and ΔE6 cells (Figure 3E). (Comparison of the efflux rates between WT cells and others is difficult because Mg^{2+} efflux was induced at much higher initial $[Mg^{2+}]_i$ in WT cells.) These data indicate that WT has Mg^{2+} transport activities, whereas ΔE6 mutant has null function.

Localization of SLC41A1 in Kidney

One of the hallmarks or NPHP is the formation of renal cortico-medullary cysts.[3,22] To ascertain why loss of SLC41A1 activity may cause the appearance of cysts at the cortico-medullary boundary, we examined whether *SLC41A1* is expressed in nephron segments in this region. Indeed, immunohistochemical analysis of *SLC41A1* expression on normal human kidney sections revealed expression primarily in the distal convoluted tubules (DCTs) and in the tubule adjacent to the macula densa (Figure 4A). Of note, claudin16, a major regulator of renal paracellular magnesium uptake in which recessive mutations cause renal disease that closely mimics NPHP in cattle,[23] was coexpressed in identical tubular segments to SLC41A1 in rat kidney sections (Figure 4B). In previous studies, RT-PCR has shown that claudin16 is expressed primarily in the DCTs and thick ascending limb of nephrons,[22] and indeed RT-PCR confirmed that *SLC41A1* is also expressed in the DCT and thick ascending limb but is absent from proximal convoluted tubule and cortical collecting duct of microdissected tubular segments (Figure 4C). Together, these data reveal that *SLC41A1* is expressed in the DCT, macula densa, and thick ascending limb tubular segments, whose location is entirely consistent with the region of cystogenesis observed in NPHP and related ciliopathies.

Knockdown of *slc41a1* in Zebrafish Results in Renal Cysts

To confirm that defective SLC41A1 function can lead to cystogenesis, we examined SLC41A1 function in the zebrafish, a widely used model organism for the study of human ciliopathies. Alignment of the human SLC41A1 protein with the zebrafish homolog revealed extensive conservation with 76% identity at the protein level, suggesting that the zebrafish homolog is likely to function in a manner similar to that of human protein (Supplemental Figure 1). To examine the expression pattern of *slc41a1* in zebrafish, an antisense *in situ* probe was generated. By *in situ* hybridization, *slc41a1* was expressed almost exclusively in the corpuscle of Stannius of the zebrafish pronephros, as previously described[24] (Figure 5A). To ablate *slc41a1* expression, a splice-blocking morpholino designed against the splice acceptor site of exon 4 (Figure 5B) was injected into 1–2 cell stage zebrafish embryos. Twenty-four hours after injection, embryos were harvested and the efficacy of the morpholino was examined by RT-PCR. RT-PCR of RNA prepared from embryos injected with a standard control morpholino revealed a PCR product of the expected size, whereas embryos injected with the splice-blocking morpholino exhibited a faster-migrating product indicative of missplicing consistent with skipping of exon 4 (Figure 5C).

To examine the effect of loss of *slc41a1* expression, 48 hours after morpholino injection, the morphology of control and *slc41a1* morphants was examined. Control morphants examined no obvious phenotype, whereas *slc41a1* morphants displayed severe developmental abnormalities (Figure 5, D and E). Specifically, >70% of *slc41a1* morphants exhibited severe ventral body curvature, a phenotype frequently observed upon knockdown of NPHP genes, compared with <2% of embryos injected with the control morpholino (Figure 5D and Supplemental Table 4). In addition, a high proportion (>50%) of the *slc41a1* morphants displayed severe hydrocephalus compared with control morphants (Figure 5D). Morphologic analysis of sections through the hindbrain of *slc41a1* morphants showed extensive dilation of the ventricle compared with controls (Figure 5E).

Because loss of *SLC41A1* function probably leads to renal dysfunction in humans, the presence of pronephric cysts in *slc41a1* morphants was examined. At 56 hours after injection, cross-sections through the zebrafish pronephros revealed the formation of cysts characterized by dilation of the pronephric duct in 60% of *slc41a1* morphants (Figure 5F and Supplemental Table 4). These data reveal that loss of *slc41a1* expression in zebrafish results in renal cyst formation but also several other phenotypes observed upon knockdown of other NPHP genes.[18,25]

DISCUSSION

NPHP-related disorders (including Bardet Biedl, Joubert, Senior-Loken, and Meckel syndromes) display significant locus heterogeneity, with causative mutations occurring in more than 30 different genes. Causative mutation frequency among these genes is not homogenous, ranging from frequent mutations (*NPHP1*, mutated in about 20% of all cases of NPHP-related disorders in our cohort) to extremely rare mutations (*GLIS2/NPHP7*, mutated in a single family).[15,26] It would appear that mutation of *SLC41A1* represents an extremely rare cause of NPHP-related disorders similar to *GLIS2/NPHP7*, as screening of 1000 patients with NPHP-related disorders using a newly developed high-throughput sequencing technique failed to identify any additional patients with *SLC41A1* mutations.[27] Furthermore, it is likely that the identified splice site mutation in *SLC41A1*, resulting in the skipping of exon 6, may be hypomorphic because a small amount of protein product was still detectable in the two affected patients (Figure 3A). Consequently, one may postulate that null mutations resulting from nonsense mutations or deletions might be embryonic lethal and hence not be represented in our cohort of patients with NPHP-RC.

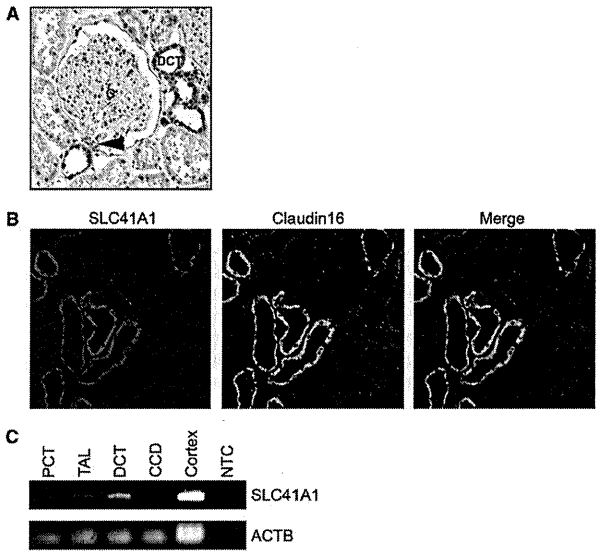

Figure 4. SLC41A1 localizes predominantly to distal convoluted tubules. (A) Immunohistochemistry was performed on human paraffin-embedded sections using rabbit anti-SLC41A1 antibodies. Signal was seen primarily in the DCTs. G, glomerulus. Arrowhead shows macula densa. (B) Rat paraffin-embedded sections were immunostained with antibodies against SLC41A1 (red) and Claudin 16 (green). DAPI (blue) was used to stain cell nuclei. (C) RT-PCR was performed on human nephron segments with primers for SLC41A1 and actin-β (ACTB) as loading control. CCD, cortical collecting duct; NTC, no template control; PCT, proximal convoluted tubule; TAL, thick ascending limb.

What remains to be ascertained in this case is the cause of the bronchiectasis in the two affected siblings and their cousin. The identified mutation in *SLC41A1* can explain the renal phenotype of the two affected siblings but cannot explain the cause of bronchiectasis because the cousin who had lung dysfunction but no renal disease is heterozygous for the *SLC41A1* mutation. A dominant effect for the *SLC41A1* allele is unlikely because neither parent of the two affected siblings who are heterozygous for the mutant *SLC41A1* allele showed any bronchiectasis phenotype. The possibility that the cousin had a compound heterozygous mutation in *SLC41A1* was ruled out as Sanger sequencing of all exons failed to identify additional mutations (data not show). The bronchiectasis phenotype probably arises from mutation of a separate gene. Using our exome data, we searched for mutations in all known primary ciliary dyskinesia genes, and although we did find variations in several, none of them segregated correctly with affected status within the family (Supplemental Table 5). Alternatively, the respiratory problems observed in the cousin (IV3) may be a phenocopy of the disease observed in the two siblings (IV1 and IV2). This is supported by the observation that the two affected siblings displayed symptoms of lung dysfunction soon after birth, whereas the cousin only exhibited problems at age 6 years.

Intracellular Mg^{2+} is a cofactor for enzymes and signal transduction proteins and regulates bioenergetics, ion transport, growth, and proliferation. $[Mg^{2+}]_i$ is thought to be maintained by transport across cell membranes with Mg^{2+} transporters. SLC41A1, a member of the solute carrier family 41, is a cell membrane protein expressed in various tissues, including heart, brain, kidney, liver, and colon, and has been proposed as one of the candidates for such Mg^{2+} transporters.[28–30] Although Mg^{2+} transport by SLC41A1 has not been fully characterized, Kolisek *et al.* recently reported that the human *SLC41A1* gene encodes for the Na^+/Mg^{2+} exchanger 4.[28] The finding that mutations of this renal Mg^{2+} transporter mimics an NPHP-RC phenotype may be related to the fact that other mutations in proteins involved in renal Mg^{2+} transport are known to cause an NPHP-related disorder phenotype. Specifically, recessive mutations of the *CLDN16* gene encoding the renal tight junction protein claudin-16 (also called paracellin-1) cause a recessive renal disease that closely mimics NPHP[31] in cattle[24] both clinically and histologically. An unusual finding, given that SLC41A1 is an apparent magnesium transporter, is that neither of the affected patients exhibited any abnormalities in serum or urine magnesium content or any evidence of nephrocalcinosis (G. Caridi, personal communication). Hence, the disease phenotype may result from perturbed intracellular magnesium homeostasis rather than global alterations in magnesium levels.

It is unclear how loss of correct magnesium homeostasis within the epithelial cells of the distal convoluted tubule could lead to the formation of cysts and the development of the NPHP-related disorder phenotype. Because the majority of cases of NPHP-related disorders are caused by mutations in genes whose products reside at or regulate ciliary function, one possibility is that the SLC41A1 transporter is regulated downstream of the NPHP-protein/ciliary network. Analysis of whether cellular magnesium levels are perturbed upon loss of cilia or knockdown of other NPHP proteins could potentially provide important insight into the pathogenesis of NPHP-related disorders. Of note, SLC41A1 is the first transporter to

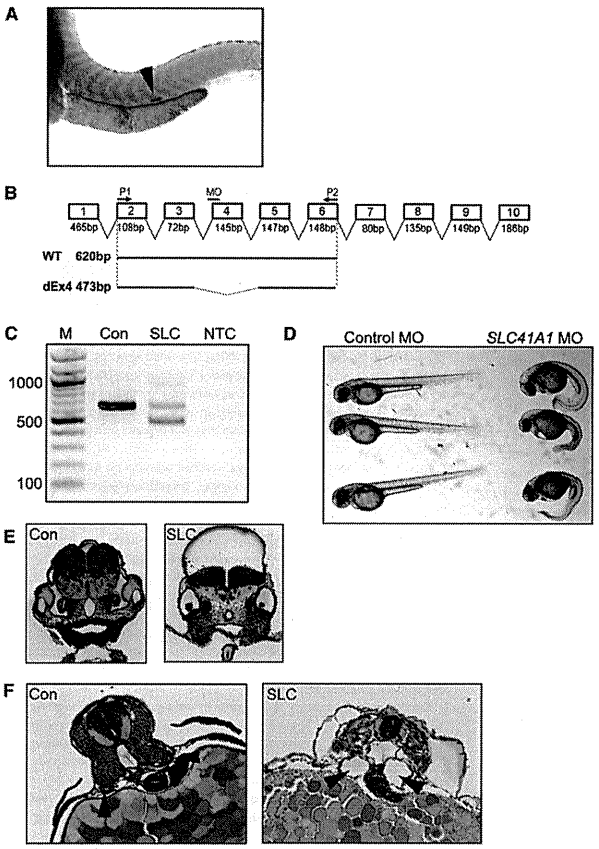

Figure 5. Knockdown of *slc41a1* expression in zebrafish results in kidney cysts. (A) *In situ* hybridization of 48-hour-old zebrafish embryos with an antisense *slc41a1* probe showing expression in the corpuscle of Stannius (arrowhead). (B) Schematic diagram of the zebrafish *slc41a1* gene showing location of the splice-blocking morpholino (MO) and primers used for RT-PCR (P1 and P2). Shown below are expected RT-PCR products using primers P1 and P2 on WT and splice morpholino injected (dEx4) samples and their expected sizes. (C) RT-PCR was performed on RNA prepared from embryos 24 hours after injection with standard control (Con) or *slc41a1* splice-blocking morpholino (SLC). Shown on the left are the sizes (in bp) of the major bands of the DNA ladder (M). NTC, no template control. (D) Phenotypic appearance at 48 hours of control and slc41a1 morpholino–injected embryos. (E) Methylene blue–stained plastic sections showing prominent hydrocephalus in *slc41a1* morpholino–injected embryos (right panel) compared with control morpholino–injected embryos (left panel). (F) Methylene blue–stained plastic sections showing tubular dilation (cysts) in *slc41a1* morpholino–injected embryos (right panel) compared with control morpholino–injected embryos (left panel). Arrowheads show pronephric tubules.

be identified as causing an NPHP-related disorder, and as such it represents an attractive potential target for pharmacologic intervention for the treatment of these disorders.

CONCISE METHODS

Research Participants

From worldwide sources we obtained blood samples and clinical and pedigree data after individuals with NPHP-related disorders and/or their parents provided informed consent. Approval for human subjects' research was obtained from the University of Michigan Institutional Review Board and relevant local review boards. NPHP-related disorder was diagnosed by (pediatric) nephrologists on the basis of standardized clinical[32] and renal ultrasonographic criteria.[4] Renal biopsy specimens were evaluated by renal pathologists.[5] Clinical data were obtained using a standardized questionnaire (http://www.renalgenes.org). Mutations in selected known *NPHP*-related condition genes were excluded using an approach of high-throughput mutation analysis.[33,34]

Homozygosity Mapping

For genome-wide homozygosity mapping[35] the Genome-wide Human SNP 6.0 ArrayII from Affymetrix was used. Genomic DNA samples were hybridized and scanned using the manufacturer's standard protocol at the University of Michigan Core Facility (www.michiganmicroarray.com). Nonparametric logarithm-of-odds scores were calculated using a modified version of the program GENEHUNTER 2.1[36,37] through stepwise use of a sliding window with sets of 110 SNPs using the program ALLEGRO.[38] Genetic regions of homozygosity by descent (homozygosity peaks) were plotted across the genome as candidate regions for recessive disease-causing genes. Disease allele frequency was set at 0.0001, and Caucasian marker allele frequencies were used.

Whole Exome Sequencing

Exome enrichment was conducted following the manufacturer's protocol for the NimbleGen SeqCap EZ Exome v2 beads (Roche NimbleGen Inc.). The kit interrogates a total of approximately 30,000 genes (about 330,000 consensus coding DNA sequence exons). Massively parallel sequencing was performed largely as described

in Bentley *et al.*[39] Sequence reads were mapped to the human reference genome assembly (National Center for Biotechnology Information build 36/hg18) and mutation calling performed using CLC Genomics Workbench (version 4.7.2) software (CLC bio, Aarhus, Denmark).

Cell Culture

HEK293T and MDCK II cells were cultured in DMEM with 10% FBS in 5% CO_2 at 37°C. Transfection was performed using Lipofectamine 2000 (Invitrogen). Cell surface biotinylation assay was performed with the Cell Surface Protein Isolation kit (Thermo Scientific) according to the manufacturer's protocol.

Constructs

Human SLC41A1 was cloned from human kidney cDNA (Clontech). Exon 6–deleted SLC41A1 was cloned from the cDNA made from EBV-transformed proband's peripheral lymphocytes. SLC41A1 cDNAs were subcloned into pEGFP-C (Invitrogen) or FLAG-tagged pcDNA3.1.

Measurement of Magnesium Influx and Efflux

Transfected cells were grown on 35-mm glass base dishes (Iwaki, Chiba, Japan) coated with Matrigel (BD Biosciences). Cells were washed with Ca^{2+}-free Tyrode solution composed of (in mM): 135 NaCl, 5.4 KCl, 1.0 $MgCl_2$, 0.33 NaH_2PO_4, 0.1 EGTA, 10 HEPES, and 2 glucose (pH 7.4 at 25°C by NaOH). After the background fluorescence of the GFP-positive transfected cells were measured, cells were incubated with 5 μM mag-fura-2-AM for 10 minutes, followed by three washes and further 20-minute incubation in the Ca^{2+}-free Tyrode solution on the stage of inverted microscope (TE300; Nikon, Tokyo, Japan). The fluorescence images of mag-fura-2 were collected from the cells at 25°C by a cooled charge-coupled device system (EM-CCD C9100, Hamamatsu Photonics, Hamamatsu, Japan) with a 40× objective (S fluor 40×0.90, Nikon). With alternate excitation at 345 and 380 nm, mag-fura-2 fluorescence images at wavelength longer than 470 nm were acquired, and digitized data were analyzed with image analysis software (Aquacosmos/Ratio, Hamamatsu Photonics). The ratio of fluorescence intensities excited at 380 nm and 345 nm was calibrated in terms of $[Mg^{2+}]_i$ as described previously.[40] To assess Mg^{2+} influx, cells were exposed to a high Mg^{2+}, low Na^+ solution composed of (in mM): 68.5 $MgCl_2$, 24 Mg-methanesulfonate, 5.4 KCl, 0.33 NaH_2PO_4, 0.1 EGTA, 10 HEPES, and 2 glucose (pH 7.4), and fluorescence images were obtained at 0, 5, 10, and 15 minutes. To assess Mg^{2+} efflux, extracellular solutions of the Mg^{2+}-loaded cells were changed back to the Ca^{2+}-free Tyrode solution and fluorescence images were obtained every 10 seconds for 20 minutes.

Morpholino Oligo-Mediated Knock-Down

To knock down zebrafish *slc41a1*, a splice-site blocking morpholino was designed against the *slc41a1* exon 4 splice acceptor site (TGAACCTGAACACAGCAGAGGGACA). Morpholinos were dissolved in nuclease-free water and injected into zebrafish embryos at 1- to 4-cell stages in 0.1 M KCl at the specified dosage. The injection volume is estimated to be 1–2 nl.

Human Kidney Samples

Kidney cortex tissues were obtained during unilateral nephrectomy for renal carcinoma.[41] The institutional review board of University of Tokyo School of Medicine approved the study. Human nephron segments were obtained from manual microdissection, as described previously.[42] Total RNA isolated from each nephron segments was used for RT-PCR. Primers were 5′-ggtcttcatcctagtgcctg and 5′-caaggtgatgaggtcgcc for SLC41A1; 5′-cgcaaagacctgtacgccaac and 5′-ccacacggagtacttgcgctc for ACTB.

Histology

Zebrafish embryos were fixed with 4% paraformaldehyde overnight, serial-dehydrated with 25%, 50%, 75%, and 95% ethanol, and then equilibrated with JB-4 solution (Polysciences) overnight at 4°C. The embryos were embedded in JB-4 resin and sectioned with a Leica R2265 microtome. The sections were stained with methylene blue as previously described.[25] For immunohistochemistry of human and rat kidney heat-induced antigen retrieval was done, and then paraffin-embedded human and rat kidney sections were stained with anti-SLC41A1 (Sigma Aldrich, St. Louis, MO) and Claudin 16 (Novus Biologicals, Littleton, CO). EnVision+ Dual Link System peroxidase (DAKO, Carpinteria, CA) and 3,3′-diaminobenzidine were used to visualize staining in human tissue. For rat kidney sections, goat anti-mouse A488 and goat antirabbit A594 (Invitrogen) secondary antibodies were used.

ACKNOWLEDGMENTS

The authors thank the families who contributed to this study. We thank Robert H. Lyons for excellent Sanger sequencing.

This research was supported by grants from the National Institutes of Health to F.H. (DK1069274, DK1068306, DK064614), W.Z. (DK091405), and E.A.O. (DK090917), and by a grant-in-aid for scientific research from the Ministry of Education, Culture, Sports, Science, and Technology of Japan to T.A. (23390033). F.H. is an investigator of the Howard Hughes Medical Institute, a Doris Duke Distinguished Clinical Scientist, and a Frederick G.L. Huetwell Professor.

DISCLOSURES

None.

REFERENCES

1. Smith JM, Stablein DM, Munoz R, Hebert D, McDonald RA: Contributions of the Transplant Registry: The 2006 Annual Report of the North American Pediatric Renal Trials and Collaborative Studies (NAPRTCS). *Pediatr Transplant* 11: 366–373, 2007
2. Bell C.J., et al Carrier testing for severe childhood recessive diseases by next-generation sequencing. *Sci Transl Med* 3: 65ra4, 2011.
3. Hildebrandt F, Benzing T, Katsanis N: Ciliopathies. *N Engl J Med* 364: 1533–1543, 2011
4. Blowey DL, Querfeld U, Geary D, Warady BA, Alon U: Ultrasound findings in juvenile nephronophthisis. *Pediatr Nephrol* 10: 22–24, 1996
5. Zollinger HU, Mihatsch MJ, Edefonti A, Gaboardi F, Imbasciati E, Lennert T: Nephronophthisis (medullary cystic disease of the kidney). A study using electron microscopy, immunofluorescence, and a review of the morphological findings. *Helv Paediatr Acta* 35: 509–530, 1980
6. Badano JL, Mitsuma N, Beales PL, Katsanis N: The ciliopathies: An emerging class of human genetic disorders. *Annu Rev Genomics Hum Genet* 7: 125–148, 2006
7. Hildebrandt F, Otto E, Rensing C, Nothwang HG, Vollmer M, Adolphs J, Hanusch H, Brandis M: A novel gene encoding an SH3 domain protein is mutated in nephronophthisis type 1. *Nat Genet* 17: 149–153, 1997
8. Otto EA, Schermer B, Obara T, O'Toole JF, Hiller KS, Mueller AM, Ruf RG, Hoefele J, Beekmann F, Landau D, Foreman JW, Goodship JA, Strachan T, Kispert A, Wolf MT, Gagnadoux MF, Nivet H, Antignac C, Walz G, Drummond IA, Benzing T, Hildebrandt F: Mutations in INVS encoding inversin cause nephronophthisis type 2, linking renal cystic disease to the function of primary cilia and left-right axis determination. *Nat Genet* 34: 413–420, 2003
9. Olbrich H, Fliegauf M, Hoefele J, Kispert A, Otto E, Volz A, Wolf MT, Sasmaz G, Trauer U, Reinhardt R, Sudbrak R, Antignac C, Gretz N, Walz G, Schermer B, Benzing T, Hildebrandt F, Omran H: Mutations in a novel gene, NPHP3, cause adolescent nephronophthisis, tapeto-retinal degeneration and hepatic fibrosis. *Nat Genet* 34: 455–459, 2003
10. Otto E, Hoefele J, Ruf R, Mueller AM, Hiller KS, Wolf MT, Schuermann MJ, Becker A, Birkenhäger R, Sudbrak R, Hennies HC, Nürnberg P, Hildebrandt F: A gene mutated in nephronophthisis and retinitis pigmentosa encodes a novel protein, nephroretinin, conserved in evolution. *Am J Hum Genet* 71: 1161–1167, 2002
11. Mollet G, Salomon R, Gribouval O, Silbermann F, Bacq D, Landthaler G, Milford D, Nayir A, Rizzoni G, Antignac C, Saunier S: The gene mutated in juvenile nephronophthisis type 4 encodes a novel protein that interacts with nephrocystin. *Nat Genet* 32: 300–305, 2002
12. Otto E, Loeys B, Khanna H, Hellemans J, Sudbrak R, Fan S, Muerb U, O'Toole JF, Helou J, Attanasio M, Utsch B, Sayer JA, Lillo C, Jimeno D, Coucke P, De Paepe A, Reinhardt R, Klages S, Tsuda M, Kawakami I, Kusakabe T, Omran H, Imm A, Tippens M, Raymond PA, Hill J, Beales P, He S, Kispert A, Margolis B, Williams DS, Swaroop A, Hildebrandt F: A novel ciliary IQ domain protein, NPHP5, is mutated in Senior-Loken syndrome (nephronophthisis with retinitis pigmentosa), and interacts with RPGR and calmodulin. *Nat Genet* 37: 282–288, 2005
13. Sayer JA, Otto EA, O'Toole JF, Nurnberg G, Kennedy MA, Becker C, Hennies HC, Helou J, Attanasio M, Fausett BV, Utsch B, Khanna H, Liu Y, Drummond I, Kawakami I, Kusakabe T, Tsuda M, Ma L, Lee H, Larson RG, Allen SJ, Wilkinson CJ, Nigg EA, Shou C, Lillo C, Williams DS, Hoppe B, Kemper MJ, Neuhaus T, Parisi MA, Glass IA, Petry M, Kispert A, Gloy J, Ganner A, Walz G, Zhu X, Goldman D, Nurnberg P, Swaroop A, Leroux MR, Hildebrandt F: The centrosomal protein nephrocystin-6 is mutated in Joubert syndrome and activates transcription factor ATF4. *Nat Genet* 38: 674–681, 2006
14. Valente EM, Silhavy JL, Brancati F, Barrano G, Krishnaswami SR, Castori M, Lancaster MA, Boltshauser E, Boccone L, Al-Gazali L, Fazzi E, Signorini S, Louie CM, Bellacchio E, Bertini E, Dallapiccola B, Gleeson JG; International Joubert Syndrome Related Disorders Study Group: Mutations in CEP290, which encodes a centrosomal protein, cause pleiotropic forms of Joubert syndrome. *Nat Genet* 38: 623–625, 2006
15. Attanasio M, Uhlenhaut NH, Sousa VH, O'Toole JF, Otto E, Anlag K, Klugmann C, Treier AC, Helou J, Sayer JA, Seelow D, Nürnberg G, Becker C, Chudley AE, Nürnberg P, Hildebrandt F, Treier M: Loss of GLIS2 causes nephronophthisis in humans and mice by increased apoptosis and fibrosis. *Nat Genet* 39: 1018–1024, 2007
16. Delous M, Baala L, Salomon R, Laclef C, Vierkotten J, Tory K, Golzio C, Lacoste T, Besse L, Ozilou C, Moutkine I, Hellman NE, Anselme I, Silbermann F, Vesque C, Gerhardt C, Rattenberry E, Wolf MT, Gubler MC, Martinovic J, Encha-Razavi F, Boddaert N, Gonzales M, Macher MA, Nivet H, Champion G, Berthélémé JP, Niaudet P, McDonald F, Hildebrandt F, Johnson CA, Vekemans M, Antignac C, Rüther U, Schneider-Maunoury S, Attié-Bitach T, Saunier S: The ciliary gene RPGRIP1L is mutated in cerebello-oculo-renal syndrome (Joubert syndrome type B) and Meckel syndrome. *Nat Genet* 39: 875–881, 2007
17. Otto EA, Trapp ML, Schultheiss UT, Helou J, Quarmby LM, Hildebrandt F: NEK8 mutations affect ciliary and centrosomal localization and may cause nephronophthisis. *J Am Soc Nephrol* 19: 587–592, 2008
18. Otto EA, Hurd TW, Airik R, Chaki M, Zhou W, Stoetzel C, Patil SB, Levy S, Ghosh AK, Murga-Zamalloa CA, van Reeuwijk J, Letteboer SJ, Sang L, Giles RH, Liu Q, Coene KL, Estrada-Cuzcano A, Collin RW, McLaughlin HM, Held S, Kasanuki JM, Ramaswami G, Conte J, Lopez I, Washburn J, Macdonald J, Hu J, Yamashita Y, Maher ER, Guay-Woodford LM, Neumann HP, Obermüller N, Koenekoop RK, Bergmann C, Bei X, Lewis RA, Katsanis N, Lopes V, Williams DS, Lyons RH, Dang CV, Brito DA, Dias MB, Zhang X, Cavalcoli JD, Nürnberg G, Nürnberg P, Pierce EA, Jackson PK, Antignac C, Saunier S, Roepman R, Dollfus H, Khanna H, Hildebrandt F: Candidate exome capture identifies mutation of SDCCAG8 as the cause of a retinal-renal ciliopathy. *Nat Genet* 42: 840–850, 2010
19. Ansley SJ, Badano JL, Blacque OE, Hill J, Hoskins BE, Leitch CC, Kim JC, Ross AJ, Eichers ER, Teslovich TM, Mah AK, Johnsen RC, Cavender JC, Lewis RA, Leroux MR, Beales PL, Katsanis N: Basal body dysfunction is a likely cause of pleiotropic Bardet-Biedl syndrome. *Nature* 425: 628–633, 2003
20. Otto EA, Ramaswami G, Janssen S, Chaki M, Allen SJ, Zhou W, Airik R, Hurd TW, Ghosh AK, Wolf MT, Hoppe B, Neuhaus TJ, Bockenhauer D, Milford DV, Soliman NA, Antignac C, Saunier S, Johnson CA, Hildebrandt F; GPN Study Group: Mutation analysis of 18 nephronophthisis associated ciliopathy disease genes using a DNA pooling and next generation sequencing strategy. *J Med Genet* 48: 105–116, 2011
21. Ng SB, Turner EH, Robertson PD, Flygare SD, Bigham AW, Lee C, Shaffer T, Wong M, Bhattacharjee A, Eichler EE, Bamshad M, Nickerson DA, Shendure J: Targeted capture and massively parallel sequencing of 12 human exomes. *Nature* 461: 272–276, 2009
22. Efrati E, Arsentiev-Rozenfeld J, Zelikovic I: The human paracellin-1 gene (hPCLN-1): Renal epithelial cell-specific expression and regulation. *Am J Physiol Renal Physiol* 288: F272–F283, 2005
23. Ohba Y, Kitagawa H, Kitoh K, Sasaki Y, Takami M, Shinkai Y, Kunieda T: A deletion of the paracellin-1 gene is responsible for renal tubular dysplasia in cattle. *Genomics* 68: 229–236, 2000
24. Wingert RA, Davidson AJ: The zebrafish pronephros: A model to study nephron segmentation. *Kidney Int* 73: 1120–1127, 2008
25. Zhou W, Dai J, Attanasio M, Hildebrandt F: Nephrocystin-3 is required for ciliary function in zebrafish embryos. *Am J Physiol Renal Physiol* 299: F55–F62, 2010
26. Soliman NA, Hildebrandt F, Otto EA, Nabhan MM, Allen SJ, Badr AM, Sheba M, Fadda S, Gawdat G, El-Kiky H: Clinical characterization and NPHP1 mutations in nephronophthisis and associated ciliopathies: Asingle center experience. *Saudi J Kidney Dis Transpl* 23: 1090–1098, 2012
27. Halbritter J, Diaz K, Chaki M, Porath JD, Tarrier B, Fu C, Innis JL, Allen SJ, Lyons RH, Stefanidis CJ, Omran H, Soliman NA, Otto EA: High-throughput mutation analysis in patients with a nephronophthisis-associated ciliopathy applying multiplexed barcoded array-based PCR amplification and next-generation sequencing. *J Med Genet* 49: 756–767, 2012
28. Kolisek M, Nestler A, Vormann J, Schweigel-Röntgen M: Human gene SLC41A1 encodes for the Na+/Mg^{2+} exchanger. *Am J Physiol Cell Physiol* 302: C318–C326, 2012
29. Goytain A, Quamme GA: Functional characterization of human SLC41A1, a Mg2+ transporter with similarity to prokaryotic MgtE Mg2+ transporters. *Physiol Genomics* 21: 337–342, 2005

30. Mandt T, Song Y, Scharenberg AM, Sahni J: SLC41A1 Mg(2+) transport is regulated via Mg(2+)-dependent endosomal recycling through its N-terminal cytoplasmic domain. *Biochem J* 439: 129–139, 2011
31. Simon DB, Lu Y, Choate KA, Velazquez H, Al-Sabban E, Praga M, Casari G, Bettinelli A, Colussi G, Rodriguez-Soriano J, McCredie D, Milford D, Sanjad S, Lifton RP: Paracellin-1, a renal tight junction protein required for paracellular Mg2+ resorption. *Science* 285: 103–106, 1999
32. Waldherr R, Lennert T, Weber HP, Födisch HJ, Schärer K: The nephronophthisis complex. A clinicopathologic study in children. *Virchows Arch A Pathol Anat Histol* 394: 235–254, 1982
33. Otto EA, et al: Mutation analysis of 18 nephronophthisis associated ciliopathy disease genes using a DNA pooling and next generation sequencing strategy. *J Med Genet* 48: 105–116, 2011
34. Harville HM, Held S, Diaz-Font A, Davis EE, Diplas BH, Lewis RA, Borochowitz ZU, Zhou W, Chaki M, MacDonald J, Kayserili H, Beales PL, Katsanis N, Otto E, Hildebrandt F: Identification of 11 novel mutations in eight BBS genes by high-resolution homozygosity mapping. *J Med Genet* 47: 262–267, 2010
35. Hildebrandt F, Heeringa SF, Rüschendorf F, Attanasio M, Nürnberg G, Becker C, Seelow D, Huebner N, Chernin G, Vlangos CN, Zhou W, O'Toole JF, Hoskins BE, Wolf MT, Hinkes BG, Chaib H, Ashraf S, Schoeb DS, Ovunc B, Allen SJ, Vega-Warner V, Wise E, Harville HM, Lyons RH, Washburn J, Macdonald J, Nürnberg P, Otto EA: A systematic approach to mapping recessive disease genes in individuals from outbred populations. *PLoS Genet* 5: e1000353, 2009
36. Strauch K, Fimmers R, Kurz T, Deichmann KA, Wienker TF, Baur MP: Parametric and nonparametric multipoint linkage analysis with imprinting and two-locus-trait models: Application to mite sensitization. *Am J Hum Genet* 66: 1945–1957, 2000
37. Kruglyak L, Daly MJ, Reeve-Daly MP, Lander ES: Parametric and nonparametric linkage analysis: A unified multipoint approach. *Am J Hum Genet* 58: 1347–1363, 1996
38. Gudbjartsson DF, Jonasson K, Frigge ML, Kong A: Allegro, a new computer program for multipoint linkage analysis. *Nat Genet* 25: 12–13, 2000
39. Bentley DR, Balasubramanian S, Swerdlow HP, Smith GP, Milton J, Brown CG, Hall KP, Evers DJ, Barnes CL, Bignell HR, Boutell JM, Bryant J, Carter RJ, Keira Cheetham R, Cox AJ, Ellis DJ, Flatbush MR, Gormley NA, Humphray SJ, Irving LJ, Karbelashvili MS, Kirk SM, Li H, Liu X, Maisinger KS, Murray LJ, Obradovic B, Ost T, Parkinson ML, Pratt MR, Rasolonjatovo IM, Reed MT, Rigatti R, Rodighiero C, Ross MT, Sabot A, Sankar SV, Scally A, Schroth GP, Smith ME, Smith VP, Spiridou A, Torrance PE, Tzonev SS, Vermaas EH, Walter K, Wu X, Zhang L, Alam MD, Anastasi C, Aniebo IC, Bailey DM, Bancarz IR, Banerjee S, Barbour SG, Baybayan PA, Benoit VA, Benson KF, Bevis C, Black PJ, Boodhun A, Brennan JS, Bridgham JA, Brown RC, Brown AA, Buermann DH, Bundu AA, Burrows JC, Carter NP, Castillo N, Chiara E Catenazzi M, Chang S, Neil Cooley R, Crake NR, Dada OO, Diakoumakos KD, Dominguez-Fernandez B, Earnshaw DJ, Egbujor UC, Elmore DW, Etchin SS, Ewan MR, Fedurco M, Fraser LJ, Fuentes Fajardo KV, Scott Furey W, George D, Gietzen KJ, Goddard CP, Golda GS, Granieri PA, Green DE, Gustafson DL, Hansen NF, Harnish K, Haudenschild CD, Heyer NI, Hims MM, Ho JT, Horgan AM, Hoschler K, Hurwitz S, Ivanov DV, Johnson MQ, James T, Huw Jones TA, Kang GD, Kerelska TH, Kersey AD, Khrebtukova I, Kindwall AP, Kingsbury Z, Kokko-Gonzales PI, Kumar A, Laurent MA, Lawley CT, Lee SE, Lee X, Liao AK, Loch JA, Lok M, Luo S, Mammen RM, Martin JW, McCauley PG, McNitt P, Mehta P, Moon KW, Mullens JW, Newington T, Ning Z, Ling Ng B, Novo SM, O'Neill MJ, Osborne MA, Osnowski A, Ostadan O, Paraschos LL, Pickering L, Pike AC, Pike AC, Chris Pinkard D, Pliskin DP, Podhasky J, Quijano VJ, Raczy C, Rae VH, Rawlings SR, Chiva Rodriguez A, Roe PM, Rogers J, Rogert Bacigalupo MC, Romanov N, Romieu A, Roth RK, Rourke NJ, Ruediger ST, Rusman E, Sanches-Kuiper RM, Schenker MR, Seoane JM, Shaw RJ, Shiver MK, Short SW, Sizto NL, Sluis JP, Smith MA, Ernest Sohna Sohna J, Spence EJ, Stevens K, Sutton N, Szajkowski L, Tregidgo CL, Turcatti G, Vandevondele S, Verhovsky Y, Virk SM, Wakelin S, Walcott GC, Wang J, Worsley GJ, Yan J, Yau L, Zuerlein M, Rogers J, Mullikin JC, Hurles ME, McCooke NJ, West JS, Oaks FL, Lundberg PL, Klenerman D, Durbin R, Smith AJ: Accurate whole human genome sequencing using reversible terminator chemistry. *Nature* 456: 53–59, 2008
40. Tashiro M, Inoue H, Konishi M: KB-R7943 inhibits Na+-dependent Mg2+ efflux in rat ventricular myocytes. *J Physiol Sci* 60: 415–424, 2010
41. Endo Y, Suzuki M, Yamada H, Horita S, Kunimi M, Yamazaki O, Shirai A, Nakamura M, Iso-O N, Li Y, Hara M, Tsukamoto K, Moriyama N, Kudo A, Kawakami H, Yamauchi T, Kubota N, Kadowaki T, Kume H, Enomoto Y, Homma Y, Seki G, Fujita T. Thiazolidinediones enhance sodium-coupled bicarbonate absorption from renal proximal tubules via PPARγ-dependent nongenomic signaling. *Cell Metab* 13: 550–561, 2011
42. Sun D, Seki G, Uwatoko S, Nakao A, Goto A, Fujita T, Kimura S, Taniguchi S. Quantifying porphobilinogen deaminase mRNA in microdissected nephron segments by a modified RT-PCR. *Kidney Int* 61: 336–341, 2002
43. Zhou W, Hildebrandt F: Molecular cloning and expression of phospholipase C epsilon 1 in zebrafish. *Gene Expr Patterns* 9: 282–288, 2009

See related editorial, "Working Out Nephronophthisis Genetics One Family at a Time," on pages 865–868.

This article contains supplemental material online at http://jasn.asnjournals.org/lookup/suppl/doi:10.1681/ASN.2012101034/-/DCSupplemental.

OPEN ACCESS Freely available online

Transscleral Sustained Vasohibin-1 Delivery by a Novel Device Suppressed Experimentally-Induced Choroidal Neovascularization

Hideyuki Onami[1,2☯], Nobuhiro Nagai[1☯], Hirokazu Kaji[3], Matsuhiko Nishizawa[3], Yasufumi Sato[4], Noriko Osumi[5], Toru Nakazawa[2], Toshiaki Abe[1]*

1 Division of Clinical Cell Therapy, United Centers for Advanced Research and Translational Medicine (ART), Tohoku University Graduate School of Medicine, Sendai, Japan, **2** Department of Ophthalmology, Tohoku University Graduate School of Medicine, Sendai, Japan, **3** Department of Bioengineering and Robotics, Graduate School of Engineering, Tohoku University, Sendai, Japan, **4** Department of Vascular Biology, Institute of Development, Aging and Cancer, Tohoku University, Sendai, Japan, **5** Division of Developmental Neuroscience, United Centers for Advanced Research and Translational Medicine (ART), Tohoku University Graduate School of Medicine, Sendai, Japan

Abstract

We established a sustained vasohibin-1 (a 42-kDa protein), delivery device by a novel method using photopolymerization of a mixture of polyethylene glycol dimethacrylate, triethylene glycol dimethacrylate, and collagen microparticles. We evaluated its effects in a model of rat laser-induced choroidal neovascularization (CNV) using a transscleral approach. We used variable concentrations of vasohibin-1 in the devices, and used an enzyme-linked immunosorbent assay and Western blotting to measure the released vasohibin-1 (0.31 nM/day when using the 10 μM vasohibin-1 delivery device [10VDD]). The released vasohibin-1 showed suppression activity comparable to native effects when evaluated using endothelial tube formation. We also used pelletized vasohibin-1 and fluorescein isothiocyanate-labeled 40 kDa dextran as controls. Strong fluorescein staining was observed on the sclera when the device was used for drug delivery, whereas pellet use produced strong staining in the conjunctiva and surrounding tissue, but not on the sclera. Vasohibin-1 was found in the sclera, choroid, retinal pigment epithelium (RPE), and neural retina after device implantation. Stronger immunoreactivity at the RPE and ganglion cell layers was observed than in other retinal regions. Significantly lower fluorescein angiography (FA) scores and smaller CNV areas in the flat mounts of RPE-choroid-sclera were observed for the 10VDD, VDD (1 μM vasohibin-1 delivery device), and vasohibin-1 intravitreal direct injection (0.24 μM) groups when compared to the pellet, non-vasohibin-1 delivery device, and intravitreal vehicle injection groups. Choroidal neovascularization can be treated with transscleral sustained protein delivery using our novel device. We offer a safer sustained protein release for treatment of retinal disease using the transscleral approach.

Citation: Onami H, Nagai N, Kaji H, Nishizawa M, Sato Y, et al. (2013) Transscleral Sustained Vasohibin-1 Delivery by a Novel Device Suppressed Experimentally-Induced Choroidal Neovascularization. PLoS ONE 8(3): e58580. doi:10.1371/journal.pone.0058580

Editor: Olaf Strauß, Eye Hospital, Charité, Germany

Received August 11, 2012; **Accepted** February 6, 2013; **Published** March 5, 2013

Funding: This work was supported in part by Grant-in-Aid for Scientific Research (No. 21592214) and Young Scientists (A) (No. 23680054) from the Ministry of Education, Culture, Sports, Science, and Technology, Health Labour Sciences Research Grant from the Ministry of Health Labour and Welfare (No. H23-iryokiki-wakate-003, H23-kankaku-ippan-004, H24-nanchitoiki-ippan-067), the Suzuken Memorial Foundation, and the Ichiro Kanehara Foundation. The funders had no role in study design, data collection and analysis, decision to publish, or preparation of the manuscript.

Competing Interests: The authors have declared that no competing interests exist.

* E-mail: toshi@oph.med.tohoku.ac.jp

☯ These authors contributed equally to this work.

Introduction

Age-related macular degeneration (AMD) is a well-known sight-threatening disease in developed countries [1]. Although many treatment regimens have been used to treat AMD [2–6], intravitreal injection of anti-vascular endothelial growth factor (VEGF) produced lesion improvement and better visual acuity in some patients [7,8]. However, intra-vitreal injection of anti-VEGF also produced irritation, infection, and other adverse side effects [9]. Further, that treatment required repeated injections, usually occurring once a month [7,8]. Thus, other types of drugs or drug delivery systems (DDSs) need to be developed to treat AMD.

Eye drops and systemic drug administration are unsuitable for retinal diseases if the physician is looking for effective drug penetration into the eye, especially for macular diseases such as AMD [10,11]. Although drug delivery device implantation into the vitreous showed effective delivery of drug to the retina, these treatments may cause severe side effects, such as infection, vitreous hemorrhage, or retinal detachment [12–14]. Drug delivery using viral vectors has been attempted for treatment of devastating retinal diseases [15]; however, this method may induce immune cell or humoral responses [16,17].

Subconjunctival drug delivery is less invasive than intravitreal drug injection and can deliver more drug than seen with eye drops or systemic administration [10,11]. There are published data investigating clinical use of subconjunctival drug administration [18,19]. Thus, the subconjunctival route may be an attractive method for drug delivery to the retina. The major difficulties with subconjunctival DDS are uncontrollable release of the target drug [20], as well as an unknown drug delivery route and mechanism to reach the retina [20,21]. Sustained release, with no drug bolus effect, would be required to reduce side effects [22,23].

We previously reported our results of the use of a novel drug delivery device placed on the sclera that we thought would be an effective tool in treating retinal diseases [24]. The device consisted of a drug-releasing semi-permeable membrane and impermeable membranes acting as the drug reservoir. Because of the non-biodegradable and one-way release nature of the device, we could achieve sustained release of the drug to the retina. We examined the effects of this device using a laser-induced choroidal neovascularization (CNV) model in rats.

Anti-VEGF antibody is a well-known treatment agent in CNV therapy, but suppression of VEGF function may induce many harmful effects in physiological function [25]. We selected vasohibin-1 for the loading drug in the device in this study because of its well-known anti-angiogenic activity [26,27]. Vasohibin-1 is a 42-kDa polypeptide, a VEGF-inducible molecule expressed by cultured human endothelial cells (ECs) [26]. Vasohibin-1 inhibits the formation of EC networks *in vitro*, corneal neovascularization *in vitro* [26], retinal neovascularization in a mouse model of oxygen-induced ischemic retinopathy [27], and laser-induced mouse [25] and monkey CNV [28]. Each of the *in vivo* studies treated the tissue by direct intravitreal injection of vasohibin-1.

Here we shall show that continuous trans-scleral vasohibin-1 delivery by the device can suppress laser-induced CNV in rat eyes (Fig. 1A) as well as that by intravitreal injection. This technique and device may hold promise for safer and more effective treatment of patients with AMD.

Methods

Vasohibin-1 and Device Preparation

Vasohibin-1 was purified as reported previously [25]. For the preparation of the vasohibin-1 formulation, an 80-μL volume of vasohibin-1 (either 1.25 or 12.5 μM) in vehicle (phosphate buffered saline [PBS] control) was mixed with 20 μL of polyethylene glycol dimethacrylate (PEGDM), then underwent UV curing at an intensity of 11.5 mJ/cm^2 (Lightningcure LCS; Hamamatsu Photonics, Hamamatsu City, Japan) for 3 minutes.

The devices consisted of a semi-permeable drug-releasing membrane and an impermeable reservoir (Fig. 1A, 1B), as we reported previously [24]. The loaded vasohibin-1 doses included vehicle only (identified as NVDD), 1 μM vasohibin-1 (VDD), and 10 μM vasohibin-1 (10VDD), with a total volume of 1.5 μL in each device. The size of the device was 2 mm×2 mm wide ×1 mm high (drug-releasing surface area; 1.5 mm×1.5 mm = 2.25 mm^2) for the rat experiments (Fig. 1B, device) and 4 mm×4 mm×1.5 mm (drug-releasing surface area; 3.5 mm×3.5 mm = 12.25 mm^2) for the vasohibin-1 releasing *in vitro* assay. The release amount from the transplanted device was small and it was very difficult to detect released vasohibin-1 by the standard ELISA technique, so we decided to use a larger device for the ELISA procedure. As a control, we used pelletized vasohibin-1 without the reservoir and permeable membrane (Fig. 1B, pellet). The concentration of pelletized vasohibin-1 was adjusted to be the same concentration as that of the 10VDD (10 μM vasohibin-1). The total amount of vasohibin-1 released from the 10VDD device during the 2-week *in vivo* experiment was aimed to be equivalent to that of the intravitreal vasohibin-1 injection. A FITC-labeled 40 kDa dextran-loaded device (FD40DD) was also used for monitoring the position of the implanted device.

In Vitro Experiments

***1 In Vitro* Release Assay, Enzyme-linked Immunosorbent Assay, and Western Blotting.** The devices loaded with vasohibin-1 were placed in the wells of a 24-well culture plate filled with 200 μL PBS at 37°C. Aliquots (200 μL) of the buffer in each well were collected at Days 1, 7, 14, and 28 during change-out of old buffer for new buffer solution. The collected samples were considered to include only protein for vasohibin-1. We then determined the amount of vasohibin-1 in the buffer using an enzyme-linked immunosorbent assay (ELISA) [29] and western blotting [30]. The intensity of the color of the ELISA reaction products was measured with a microplate reader (MAXline; Molecular Devices Corporation, Sunnyvale, CA, USA). The measurements were made in duplicate, and the mean value was used for comparisons. The 50-μL collected samples and 100 fmol of recombinant vasohibin-1 (positive control) were loaded, separated by sodium dodecyl sulfate-polyacrylamide gel electrophoresis (SDS-PAGE) on a 10% separating gel, and transferred to nitrocellulose membranes for western blotting. The membranes were blocked for 1 hour at room temperature with 5% ECL blocking agent (GE Healthcare Biosciences, Pittsburgh, PA, USA), and then incubated overnight at 4°C in PBS containing 0.05% Tween 20 (T-PBS), 2.5% skim milk, and 1 μg/mL horseradish peroxidase-conjugated anti–vasohibin-1 monoclonal antibody. The membrane filters were washed 3 times with T-TBS and the blots were detected using an enhanced chemiluminescence method (ECL Western Blotting Detection Kit; Amersham Biosciences, Piscataway, NJ, USA). The results were visualized using an imaging system (ImageQuant LAS-1000; GE Healthcare Biosciences).

2 Endothelial Tube Formation. Endothelial tube formation was assessed with normal human umbilical vein endothelial cells (HUVECs) (Takara Bio; Otsu, Japan) co-cultured on neonatal normal human dermal fibroblasts (NHDF, Takara Bio) layer using anti-human CD31 immunostaining, as reported previously [28]. Two nM vascular endothelial growth factor (VEGF, Wako; Tokyo, Japan) was then added to the endothelial cell growth medium (EGM, Takara Bio) containing no vasohibin-1 (control), and 0.2, 2, or 10 nM vasohibin-1, respectively. VEGF (2 nM) and samples of vasohibin-1 released from the vasohibin-1-loaded device over 3 hours at 37°C were used to examine released vasohibin-1 activity. We collected the released vasohibin-1 from the pellet and used it at a concentration of 0.56 nM (as measured by ELISA). On Day 3, the cells were fixed and stained using an anti-human CD31 immunostaining kit (Kurabo; Tokyo, Japan) according to the manufacturer's instructions. The number of stained HUVECs was determined using a computerized system (Kurabo Angiogenesis Image Analyzer program; Kurabo).

In Vivo CNV Experiments

1 Animals. The procedures used in the animal experiments followed the guidelines of the Association for Research in Vision and Ophthalmology Statement for the Use of Animals in Ophthalmic and Vision Research, and they were approved by the Animal Care Committee of Tohoku University Graduate School of Medicine (Permit Number: 2011–136). Twenty Sprague-Dawley (SD) rats (Experiments 1 and 2) and 36 Brown Norway (BN) rats (Experiment 3) weighing between 250 and 300 g were used (Table 1). All animals were followed up to 2 weeks after device transplantation and/or laser burn. We examined the effects of devices either at 1 week or 2 weeks for FA evaluation and 2 weeks for flat-mount evaluation. Macro examination was performed at 1 and 2 weeks after the device transplantation. For all procedures, the rats were anesthetized with an intramuscular

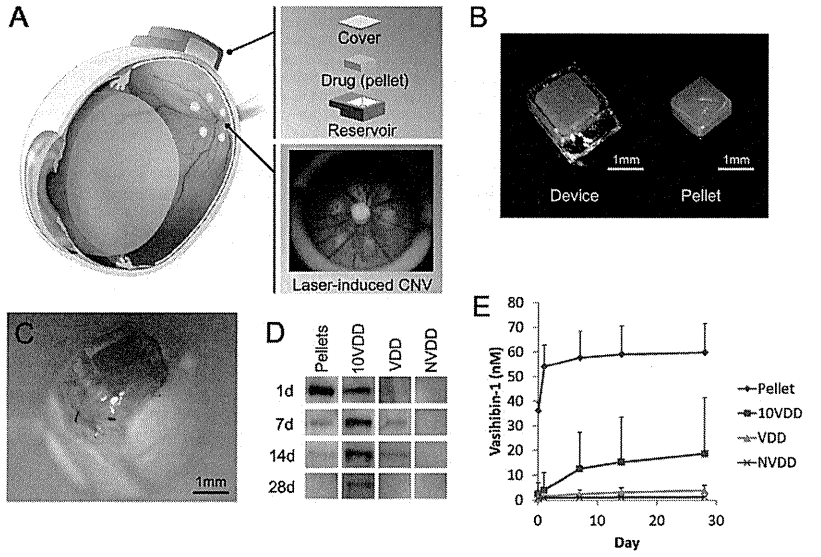

Figure 1. Device and vasohibin-1 release. (A) Schematic image of transscleral sustained vasohibin-1 delivery. We evaluated its effects via transscleral approach for rat laser-induced choroidal neovascularization (CNV). The device consists of a drug pelletized with PEGDM, a reservoir made of TEGDM, and a controlled-release membrane made of PEGDM that contains collagen microparticles. (B) Photograph showing a drug pellet and the delivery device containing a drug pellet. (C) Image of a device placed on the sclera of a rat eye at 3 days after implantation. The amount of vasohibin-1 in the PBS was measured at 1, 7, 14, and 28 days after starting incubation. The representative results of western blotting and the result of ELISA are shown in (D) and (E), respectively. We collected the samples at only the given time points and replaced only the equal volume of PBS. The released vasohibin-1 amounts accumulated for 6, 7, and 14 days. [The pellet samples collected at Day 1 (shown as 1d) were diluted five times due to their concentration before they were evaluated by western blotting]. NVDD: non-vasohibin-1 (vehicle) delivery device, VDD: 1 μM vasohibin-1 delivery device, 10VDD: 10 μM vasohibin-1 delivery device, Pellets: vasohibin-1 pelletized at the same concentration of 10VDD (without reservoir and cover).
doi:10.1371/journal.pone.0058580.g001

injection of ketamine hydrochloride (35 mg/kg) and xylazine hydrochloride (5 mg/kg), and the animals' pupils were dilated with topical 2.5% phenylephrine and 1% tropicamide. Oxybuprocaine hydrochloride (0.4%) was also used for local anesthesia. In all *in vivo* experiments, the animal's left eye was used as a control.

2 Implantation of VDDs, Pellets, and Intravitreal Vasohibin-1 Injection. Devices were implanted subconjunctively in the right eyes of the rats (Table 1). A 4-mm long conjunctival incision was made along the limbus in the upper temporal position. The devices were inserted into the subconjunctival space using forceps, with the drug-releasing surface facing the sclera. The device was placed between the optic disc and the equator, in the posterior quadrant, using no suture to anchor it into place. The conjunctival incision was closed with 9–0 silk and antibiotic ointment was applied to the eyes. Vasohibin-1 protein (0.24 μM) was injected using a 10-μL glass syringe (Hamilton; Reno, NV) 4 days after the experimental CNV procedure. The left eyes were used as untreated controls.

The rats were anesthetized, pupils were dilated, and a fundus examination was performed immediately after the surgery.

Experiment 1: Monitoring the Implanted Devices and Pellets

To monitor the device and drug release, fluorescein isothiocyanate (FITC) dextran (FD40; Sigma-Aldrich) pelletized with PEGDM was prepared and used as a control drug. The FD40 was dissolved in PBS at a concentration of 250 mg/mL and loaded in the device in the same way as vasohibin-1. Eight SD rats were included in this experiment; 4 rats received the FD40 delivery device (FD40DD) and 4 rats received only pelletized FD40.

Experiment 2: Immunohistochemistry after Device Implantation

Immunostaining for vasohibin-1was performed 2 weeks after device implantation. Twelve SD rats were used as follows (Table 1): 4 rats received vehicle (non-vasohibin-1) in the delivery device on the sclera (NVDD), 4 rats received 1.5 μL of 10 μM vasohibin-1 in the delivery device (10VDD), and 4 rats received 1.5 μL of 10 μM vasohibin-1 pellets implanted on the sclera. Immunohistochemistry was performed as reported previously [25].

Animals were euthanized using overdoses of ketamine hydrochloride and xylazine hydrochloride. The eyes were enucleated and fixed for 12 hours in 4% paraformaldehyde (PFA) at 4°C. The anterior segment and lens were removed from each eye. The posterior segment was cryoprotected at 4°C through successive 12-hour incubations in 10%, 20%, and 30% sucrose dissolved in saline. The tissues were immersed in OCT compound (Tissue-Tec; Sakura Finetec USA, Inc., Torrance, CA, USA) and frozen in acetone in a dry-ice bath. The frozen posterior segment was sectioned at the center of the implanted area at a thickness of 5 μm for each section, using a cryostat. We examined eight continuous sections per eye. The sections were incubated in rabbit polyclonal antibody against human vasohibin-1, followed by FITC-conjugated anti-rabbit IgG (1:200; Dako, Glostrup, Denmark) for 30 minutes. The sections were washed three times with PBS between each step. Negative controls (4 rats) incubated with just FITC-conjugated anti-rabbit IgG were also prepared. Slides were counterstained with 4, 6-diamino-1-phenylindole (DAPI; Vector Laboratories, Burlingame, CA, USA) and photographed using a fluorescence microscope (Leica FW4000, Ver. 1.2.1; Leica Microsystems Japan, Tokyo, Japan).

Table 1. In Vivo Study Demographics.

Number of animals	Strain	Treatment	Methods	Position of implant
Experiment 1				
4	SD	Untreated	FD40DD	Sclera
4	SD	Untreated	FD40 Pellet	Sclera
Experiment 2				
4	SD	Untreated	NVDD	Sclera
4	SD	Untreated	10VDD	Sclera
4	SD	Untreated	Pellet	Sclera
Experiment 3				
6	BD	CNV	NVDD	Sclera
6	BD	CNV	VDD	Sclera
6	BD	CNV	10VDD	Sclera
6	BD	CNV	Pellet	Sclera
6	BD	CNV	Vehicle	Vitreous
6	BD	CNV	Vasohibin-1	Vitreous

SD: Sprague-Dawley rats, BN: Brown Norway rats, CNV: choroidal neovascularization, NVDD: non-vasohibin-1 delivery device, 10VDD: 10 μM vasohibin-1 delivery device.
doi:10.1371/journal.pone.0058580.t001

Experiment 3: Choroidal Neovascularization Study

A total of 36 BN rats were used (Table 1). The devices and pellets were implanted on the same day as the CNV procedure. The rats were divided into six groups (6 rats in each group): rats with NVDD, rats with 1.5 μL of 1 μM vasohibin-1 in the delivery device (VDD), rats with 1.5 μL of 10 μM vasohibin-1 in the delivery device (10VDD), rats with 1.5 μL of 10 μM vasohibin-1 pellets implanted on the sclera, rats with intravitreal injection of 5 μL of vehicle, and rats with an intravitreal injection of 0.24 μM vasohibin-1 protein occurring 4 days after the experimental CNV procedure. The amount of intravitreal vasohibin-1 used and the day of the injection were determined based on our previous data [25]. The intravitreal injections were performed using a 10-μL glass syringe (Hamilton), and the needle was passed through the sclera just behind the limbus into the vitreous cavity.

3 CNV procedure. A green argon laser was used to rupture the choroidal membrane using a slit-lamp delivery system (Ultima 2000SE; Lumenis, Yokneam, Israel) with a contact lens [31]. The laser settings were: 50 μm diameter for 0.1 sec duration, at an intensity of 650 to 750 mW. Six laser burns were made around the optic disc (Fig. 1A). Each burn was confirmed to have induced subretinal bubbles, indicating a rupture of Bruch's membrane.

In addition to the routine ophthalmological examinations, fluorescein angiography (FA) with an imaging system (GENESIS-Df; Kowa, Tokyo, Japan) was performed at 1 and 2 weeks after the CNV laser burn, and choroidal flat mounts of the CNV site were performed at 2 weeks after the procedure. Two retinal specialists (HO and TA) and one non-specialist (NN) evaluated the angiograms for FA grading evaluation in a blinded manner using a grading system [32], where Grade 1 = no hyperfluorescence; Grade 2 = hyperfluorescence without leakage; Grade 3 = hyperfluorescence in the early or middle phase and leakage in the late phase; and Grade 4 = bright hyperfluorescence in the transit and leakage in the late phase beyond the treated areas. The camera was a handheld retinal camera for photographing humans, and the fact that rat eye optics differ from that of humans made the process somewhat difficult. Intense fluorescein leakage also made the results of photographs as faint. The laser burn sometimes made subretinal hemorrhages that were shown as fluorescein blockage. These results may have influenced the evaluation. We tried to focus on the laser burn as much as possible to not influence the evaluation. Further we also tried to synchronize evaluations as much as possible to avoid significant bias due to fluorescein leakage. Total grades were analyzed for statistical significance.

4 Fluorescein-Labeled Dextran Perfusion and Choroidal Flat-Mount Preparation. The size of the CNV lesion was measured on choroidal flat mounts to examine the effect of the vasohibin-1 delivery device (n = 6 eyes/group and each eye had 6 laser spots). Fourteen days after the CNV procedure, the rats were perfused with 5 mL PBS containing 50 mg/mL fluorescein-labeled dextran (FITC-dextran, MW: 2×10^6; Sigma-Aldrich). Results of mouse CNV experiments [25] indicated that laser-induced CNV lesions were most active at 14 days after laser application and gradually self-resolved more than 28 days after the laser burn. This data was supported by our previous study of laser-burned monkey eyes [28].

We enucleated the eyes in the current study at 14 days after the CNV laser procedure, after euthanizing the animals per the previously described method. The eyes were removed and fixed for 30 minutes in 4% phosphate-buffered PFA. The cornea and lens were removed and the entire retina was carefully dissected from the eyecup. Radial cuts (4 to 6) were made from the edge to the equator, and the eyecup of the RPE-choroid-sclera (R-C-S) complex was flat mounted in Permafluor (Beckman Coulter; Fullerton, CA, USA) with the scleral side facing down. Flat mounts were examined by fluorescence microscopy (Leica FW4000, Leica Microsystems Japan), and the total area of each CNV zone associated with each burn was measured. The CNV lesions were identified by the presence of fluorescent blood vessels on the choroidal/retinal interface circumscribed by a region lacking fluorescence. This process duplicated past reported procedures [33,34]. Two retinal specialists (HO and TA) and one non-specialist (NN) evaluated the size of the dextran-fluorescein perfused CNVs in a blinded manner, as described above.

Statistical Analyses

Analysis of variance (ANOVA) with Tukey's test was used to examine differences in the leakage and severity of the CNVs in the fluorescein angiograms and the area of the choroidal flat mount. Endothelial tube formation was also evaluated by this method. P-values less than 0.05 were considered significant.

Results

In Vitro Vasohibin-1 Release from the Device

Each result is shown as mean ± SD of three different experiments in Figure 1E. A prominent initial increase was observed in vasohibin-1 pellets (Pellet) and it appeared to almost plateau at 7 days after the start of incubation. A minor increase was observed in the vasohibin-1 delivery devices (VDD) with an almost level release observed over the 28 days of incubation. If we examine the amount released from the device (4×4×1.5 mm) between Days 7 and 28, the amount released was estimated to be 0.31 nM/day in the 10VDD group, 0.070 nM/day in the VDD group, 0.088 nM/day in the pellets, and 0 in the NVDD group (Fig. 1E) in a closed incubation system, when we used 500 mg/mL COLs for the permeable PEG/COLs membranes. These calculations were performed from the fitting line between 0 and 28 days. In rat experiments, the release amount would be less, because we used a smaller device for rats than used in the *in vitro* release assay. The larger device used in the *in vitro* release assay in Fig. 1E had 5.44 times (12.25 mm^2 vs 2.25 mm^2) larger drug-releasing surface area and 3.42 times faster releasing rate than that of the transplanted device used in rats, from the results of Fig. S1. The total amount of vasohibin-1 released from the 10VDD devices during the CNV suppression experiment in rats was estimated grossly to be approximately 4.28 nM over 2 weeks. The total amount of vasohibin-1 during the 2 weeks was estimated as about 14.6 nM from the results of Figure 1E, and was divided by 3.42, which is the difference in releasing rate between *in vitro* release assay and *in vivo* experiments, although the effective amount of vasohibin-1 in CNV suppression would be smaller than 4.28 nM, due to drug elimination from the eye. These results were confirmed by western blotting analysis; Figure 1D shows the representative results at Days 1, 7, 14, and 28. A greater amount of vasohibin-1 was observed in the 10VDD and pellet groups than was seen in the NVDD and VDD groups. The results of the pellet group at Day 1 (1d in Fig. 1D) was obtained after diluting the samples five times, because the concentration was too high to be shown by western blotting. However, the size of the pellets was much smaller after 7 days of incubation.

Endothelial Tube Formation

Endothelial tube formation of HUVECs cultured on the NHDF layer was assessed using anti-human CD31 immunostaining (Fig. 2). We used a range of native vasohibin-1 concentrations (from 0 to 10 nM, using 2 nM VEGF) for the preliminary experiments. After the initial examination, the cells were fixed and stained using anti-human CD31. Figures 2A–2G show representative photographs of the experimental results. Figure 2E shows the results of released vasohibin-1 (0.56 nM) from the devices with 2 nM VEGF. Figure 2H shows the average of each experiment; significantly fewer CD31-positive points were observed in released vasohibin-1-treated wells when compared to those of the vehicle released from the NVDD ($p = 0.000001$) or VEGF-treated control ($p = 0.000002$). Vasohibin-1 released from the device showed activity comparable to the native vasohibin-1.

Macro Examination

FD40 was detected in the device (Figs. S2A and S2B show color and fluorescein photographs, respectively) or in pellets (Figs. S2G and S2H) at the implant site through the conjunctiva in the live rats. When we enucleated the eyes at a week after device implantation, mild fibrosis was observed around the devices (Fig. S2C) and around the pellets (Fig. S2I). Fluorescein photography demonstrated the presence of FD40 in the device, with little fluorescein in the conjunctiva and surrounding tissues (Fig. S2D, arrow). FD40 was also detected in the sclera after removal of the device (Figs. S2E and S2F, arrow). Conversely, FD40 pellets showed strong fluorescein on the conjunctiva and surrounding tissues, as was seen for the pellet itself (Fig. S2J, arrow). Furthermore, little fluorescein was observed on the sclera after removal of the device (Figs. S2K and S2L, arrow). Similar conditions were observed when we examined the tissues at 2 weeks after device and pellet implantation; fluorescence was observed over a wider area for those specimens where the device was implanted compared to results at Week 1 (data not shown).

Immunohistology of Vasohibin-1

In immunostained eyes, vasohibin-1-positivity was found in only the 10VDD group (Fig. 3B), but not in the NVDD group (Fig. 3A) or the negative control without the first antibody (Fig. 3D), mainly at the region where vasohibin-1 releasing devices were placed. Pellets showed strong local immunoreactivity, but no immunoreactivity in the retina (Fig. 3C). Vasohibin-1 positivity was observed in the neural retina and optic nerve (white arrows in Fig. 3B). Strong immunoreactivity was observed in the choroid, RPE, and at the inner layer (such as the ganglion cell layer [GCL]) by magnified photographs after device implantation (Fig. 3E).

Leakage from CNV

Fluorescein angiography results of each group at 1 week after the laser CNV procedure are shown in Figure 4A. The results show that an intravitreal injection of vasohibin-1 on Day 4 after the CNV procedure led to a significant reduction of FA scores when compared to those of NVDD ($p = 0.0014$), pellet ($p = 0.020$), and vehicle injection ($p = 0.040$) (Fig. 4B). The 10VDD implantation led to a significant reduction of FA scores when compared to the result of the NVDD group ($p = 0.00006$). The VDD implantation led to a significant reduction of FA scores when compared to those of NVDD ($p = 0.000017$), pellet ($p = 0.012$), and vehicle injection ($p = 0.026$). Although FA scores of the 10VDD group seemed to be smaller than those of the pellet ($p = 0.065$) and vehicle injection ($p = 0.12$), the results were not significant. Figure 5A shows the FA results at Week 2 in each group. Significantly lower FA scores were observed for the vasohibin-1 intravitreal injection group when compared to those of NVDD ($p = 0.000022$), and vehicle intravitreal injection ($p = 0.0065$). Further, significantly lower FA scores were observed in the 10VDD group when compared to those of NVDD ($p = 0.000003$) and vehicle injection ($p = 0.0080$) (Fig. 5B). Significantly lower FA scores were also observed in the VDD group when compared to those of NVDD ($p = 0.000058$) and vehicle injection ($p = 0.011$).

Flat-mount Examination of the CNV Site

Choroidal flat mounts were prepared 2 weeks after device implantation; representative results of each group are shown in Figure 6A. The area of the CNV was 27,288±7,975 μm^2 for the NVDD group; 23,532±13,120 μm^2 for the VDD group; 17,382±715 μm^2 for the 10VDD group; 30,502±780 μm^2 for the vasohibin-pellet group; 26,900±9,067 μm^2 for the intravitreal vehicle injection group, and 12,731±4,113 μm^2 for the intravitreal vasohibin-1 injection group (Fig. 6B). The CNV area was smaller in eyes that were treated with 10VDD or intravitreal vasohibin-1 injection compared to the other treatments. A significantly smaller CNV area was observed in the 10VDD group when compared to those of the NVDD ($p = 0.0004$), pellet transplantation ($p = 0.0011$), and intravitreal vehicle injection groups ($p = 0.000015$). A significantly smaller CNV area was also observed in eyes injected with intravitreal vasohibin-1 when compared to those of the NVDD ($p = 0.000006$), VDD ($p = 0.0036$), pellet transplantation ($p = 0.000023$), and intravitreal vehicle injection groups ($p = 0.000001$) (Fig. 6B). No significant difference was observed when we compared the VDD with those

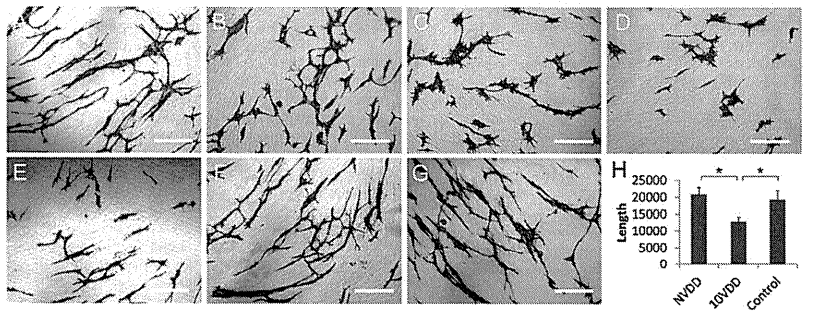

Figure 2. The activity of vasohibin-1 by an endothelial cell tube formation assay. The activity of vasohibin-1 was confirmed by an *in vitro* endothelial cell tube formation assay. Vasohibin-1 suppressed the HUVEC tube formation in a dose-dependent manner. Representative results of HUVEC tube formation treated with 2 nM VEGF combined with 0 (A), 0.2 (B), 2 (C), and 10 nM vasohibin-1 (D) are shown. Bars indicate 100 μm. The released vasohibin-1 from the device showed comparable results to native activity (E). Significant suppression of HUVEC tube formation was observed in released vasohibin-1 when compared to those treated with NVDD (F) and with only 2 nM VEGF without vasohibin-1 (G). (H) shows the average of each experiment; significantly fewer CD31-positive points were observed in released vasohibin-1-treated wells when compared to those of the vehicle released from NVDD ($p<0.0001$) or the VEGF-treated control ($p<0.0001$). The vasohibin-1 released from the device showed activity comparable to the native vasohibin-1. Vertical bar indicates total length of tube formation. NVDD: non-vasohibin-1 (vehicle) delivery device, 10VDD: 10 μM vasohibin-1 delivery device.
doi:10.1371/journal.pone.0058580.g002

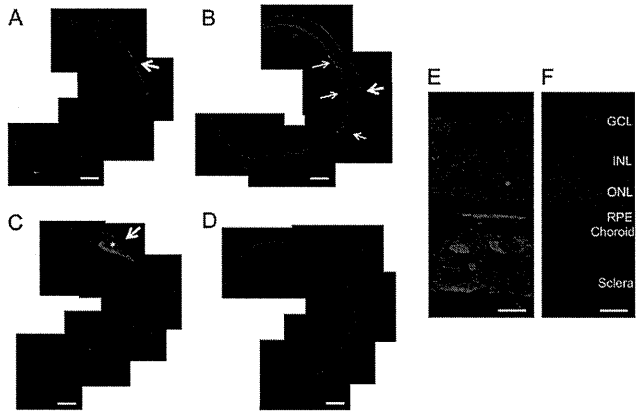

Figure 3. Immunohistochemistry of vasohibin-1 after device implantation. The immunohistochemistry results of vasohibin-1 after NVDD, 10VDD, and pellet implantation are shown. No immunoreactivity was observed after NVDD transplantation (A) and negative control without first antibody (D). 10VDD shows vasohibin-1 immunoreactivity at the device implant area (B). White arrows show the immunoreactivity in the retina and optic nerve at low magnification. Diffuse immunoreactivity was observed in the sclera, choroid, RPE, and retina at greater magnification (E). Strong immunoreactivity was observed in the ganglion cell layer (GCL) and retinal pigment epithelium (RPE), as well as in the sclera and choroid. INL and ONL indicate the inner and outer nuclear layers. These results were not observed in the NVDD group (A) or the negative controls (D and F). Strong immunoreactivity was observed in the pellet (asterisk) and in the tissues surrounding the implanted pellet (C). Yellow arrows indicate the positions where devices or pellets were placed. Devices were removed before sectioning, but pellets were not removed before sectioning. Bars: 200 μm (A–D), and 50 μm (E, F).
doi:10.1371/journal.pone.0058580.g003

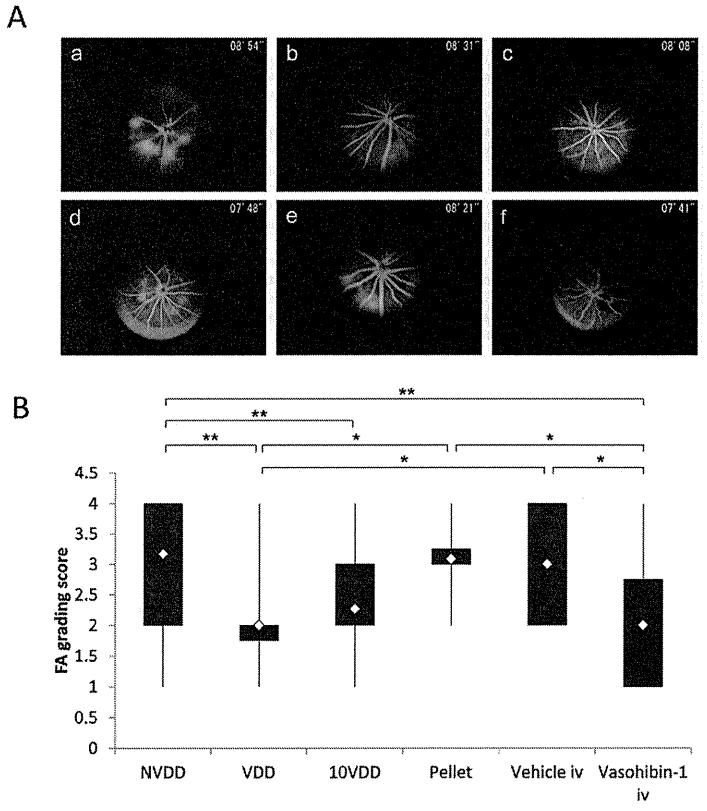

Figure 4. Fluorescein angiography 1 week after CNV laser procedure. (A) Representative results of fluorescein angiography (FA) in each group at 1 week after CNV laser procedure. The groups were treated with NVDD (a), VDD (b), 10VDD (c), vasohibin-1 pellet (d), intravitreal vehicle injection (Vehicle iv) (e), or intravitreal vasohibin-1 injection (Vasohibin-1 iv) (f). (B) Fluorescein angiography scores for each of the six laser spots in each eye are plotted and calculated for each group. Significantly lower FA scores was shown in the Vasohibin-1 iv group when compared to those of NVDD ($p = 0.00014$), pellet ($p = 0.02$), and Vehicle iv ($p = 0.040$). Significantly lower FA scores are also observed in the 10VDD group when compared to the NVDD group ($p = 0.00006$). Significantly lower FA scores are also observed in the VDD group when compared those of NVDD ($p = 0.00017$), Pellet ($p = 0.012$), and intravitreal vasohibin-1 injection ($p = 0.026$). Significant differences are shown as asterisks. NVDD: non-vasohibin-1 (vehicle) delivery device, VDD: 1 μM vasohibin-1 delivery device, 10VDD: 10 μM vasohibin-1 delivery device, Pellet: vasohibin-1 pelletized at the same concentration of 10VDD (without reservoir and cover).
doi:10.1371/journal.pone.0058580.g004

of NVDD ($p = 0.7374$), pellet transplantation ($p = 0.3616$), and intravitreal vehicle injection ($p = 0.7178$) groups.

Discussion

Attention has been paid to sustained drug delivery in the treatment of AMD because regimens including intravitreal anti-VEGF injection require repeated injection and may lead to adverse side effects [9,35]. Sustained delivery of large molecules such as antibodies may be attractive, because not only anti-VEGF therapy and anti-TNFα antibody have shown excellent results in the treatment of refractory eye diseases (such as Behcet's disease), although this regimen also requires repeated cycles of therapy [36,37]. When our devices were cultured in PBS, vasohibin-1 was released over time, with activity equivalent to that seen with native vasohibin-1. These positive results were also observed with brain-derived neurotrophic factor (BDNF) and 40 kDa dextran, as reported previously [24]. Our implantable device showed sustained protein release over time. The relatively large standard

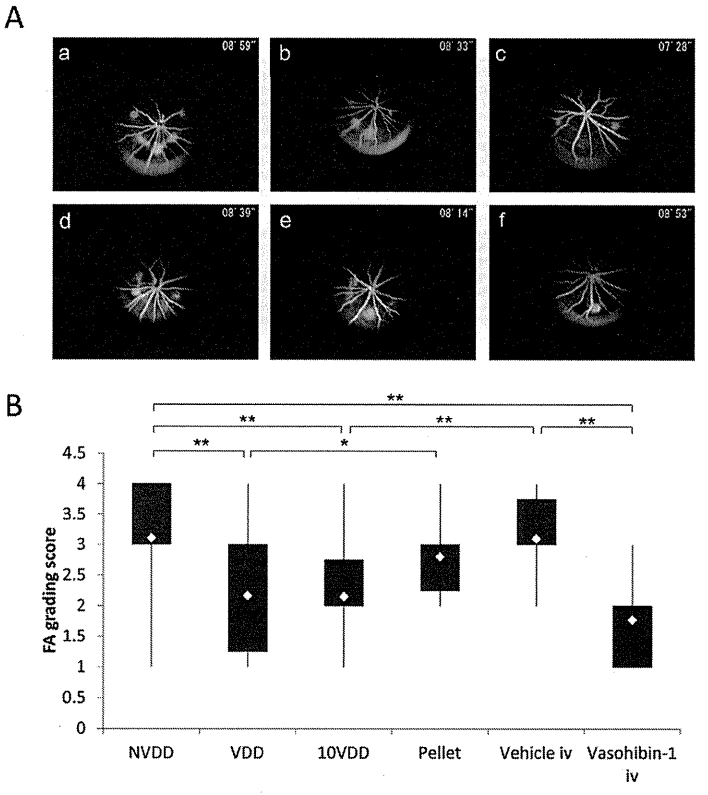

Figure 5. Fluorescein angiography 2 weeks after CNV laser procedure. (A) Representative results of fluorescein angiography in each group at 2 weeks after CNV laser procedure. The groups were treated with NVDD (a), VDD (b), 10VDD (c), vasohibin-1 pellet (d), intravitreal vehicle injection (Vehicle iv) (e), intravitreal vasohibin-1 injection (Vasohibin-1 iv) (f). (B) Significantly lower FA scores was shown in the Vasohibin-1 iv group when compared to those of NVDD ($p = 0.000022$), and Vehicle iv ($p = 0.0065$). Significantly lower FA scores are also observed in the 10VDD group when compared to the NVDD group ($p = 0.00003$) and intravitreal vehicle injection ($p = 0.011$). Significant differences are shown as asterisks. NVDD: non-vasohibin-1 (vehicle) delivery device, VDD: 1 μM vasohibin-1 delivery device, 10VDD: 10 μM vasohibin-1 delivery device, Pellets: vasohibin-1 pelletized at the same concentration of 10VDD (without reservoir and cover).
doi:10.1371/journal.pone.0058580.g005

deviation in the 10VDD group may be indicative of imperfect device preparation. From the results of western blotting, the 10VDD group showed a mild initial release of drug, although the level was far less than seen in the pellet-only group. Technical improvements in delivery device design may overcome these problems. This is an attractive device designed with sustained protein delivery for the treatment of eye diseases.

Subconjunctival drug administration produces better drug penetration than eye drops and is less invasive than intravitreal injection. However, conjunctival and episcleral blood and lymphatic flows have been reported to be the main limiting factors for posterior segment drug distribution by subconjunctival drug administration [38–40]. Our results also showed that implantation of pelletized vasohibin-1 alone (with no reservoir) produced much less vasohibin-1 immunoreactivity than seen with 10VDD implantation. Implanted between the sclera and conjunctiva, our device was designed to release the drugs only to the scleral side of the eye, so a limiting factor of drug diversion to the conjunctival blood flow may be reduced. Carvalho et al [41] reported that their tightly-sutured, one-side-open device delivered higher amount of sodium fluorescein than others, although they used small molecules with their device. From the histological analysis of our experimental procedure, we saw no signs of inflammation or adverse effects in the eye that could be attributed

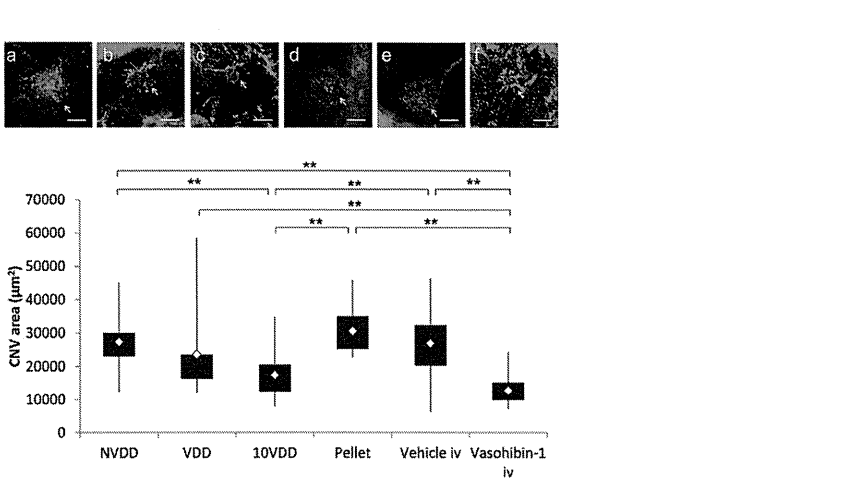

Figure 6. Flat-mount examination of the CNV site. The areas of choroidal neovascularization with devices, pellets, and intravitreal injection of recombinant vasohibin-1 protein. (A) Representative choroidal flat-mount photographs of the groups treated with NVDD (a), VDD (b), 10VDD (c), vasohibin-1 pellet (Pellet) (d), intravitreal vehicle injection (Vehicle iv) (e), intravitreal vasohibin-1 injection (Vasohibin-1 iv) (f) eyes at 2 weeks after the CNV laser procedure. Mean values of actual areas are shown in the text. Bars: 200 μm. (B) Significantly smaller CNV areas were observed in the 10VDD group when compared to those of the NVDD ($p = 0.0004$), Pellet ($p = 0.0011$), and Vehicle iv groups ($p = 0.000015$). Significantly smaller CNV areas were observed in eyes treated with Vasohibin-1 iv when compared to those treated with NVDD ($p = 0.000006$), VDD ($p = 0.0036$), Pellet ($p = 0.000023$), or Vehicle iv ($p = 0.000001$). NVDD: non-vasohibin-1 (vehicle) delivery device, VDD: 1 μM vasohibin-1 delivery device, 10VDD: 10 μM vasohibin-1 delivery device, Pellet: vasohibin-1 pelletized at the same concentration of 10VDD (without reservoir and cover).
doi:10.1371/journal.pone.0058580.g006

to device implantation, except for a mild fibrosis observed around the devices at 2 weeks post-surgery. We also found that the devices removed from the rats where fibrosis was noted showed continuing vasohibin-1 release and comparable activity when we cultured the removed device/tissues in PBS (data not shown).

Vasohibin-1 was observed on the retina at 2 weeks post-implant, principally noted in the regions where the devices were implanted. Some of the regions showed strong immunoreactivity for vasohibin-1, especially at the retinal pigmented epithelium (RPE) and the retinal ganglion cell layer (GCL); the first finding may be due to being the main outer blood-retinal barrier, while the second may be due to the vitreous-retinal barrier [42]. Vasohibin-1 released from the device may be stored in cells in these regions and later released to other regions of the retina or vitreous.

Our results demonstrated that vasohibin-1 can be delivered by our device into the retina transsclerally. Amaral et al also reported transscleral protein (pigment epithelium-derived factor and ovalbumin) delivery into the retina, although they used uncontrollable drug release via a matrix-type implant [10]. Drug released from their device was not delivered unidirectionally. Although there is a blood-retinal barrier, the penetration of such large molecules into the eye may not be so surprising. When we consider the phenomenon of some type of cancer-associated retinopathy, auto-antibodies against retinal cells or retinal-specific antigens have been reported to cause retinal dysfunction [43–45]. The elimination of proteins is reported to be one to two orders of magnitude slower than that of small molecules via the sub-conjunctival and episcleral blood flow [46], with similar results reported for the choroidal blood flow [21]. This fact may also help protein delivery to the retina with the use of our device.

Although we have not studied vasohibin-1 release from the device for more than 2 weeks *in vivo* because of the experimental design, more than 80% of the vasohibin-1 was present in the device at the end of the experimental procedure. The devices removed at the end of the experiment were still releasing vasohibin-1 (data not shown), indicating that it might be possible to use the implanted device for a longer time. These data could also indicate that we may be able to use a smaller device than those used in this experiment to deliver the same amount of drug.

Fluorescein angiography examination showed significantly lower scores in the eyes that received intravitreal vasohibin-1 than those of the intravitreal vehicle-injected eyes. The effects of vasohibin-1 were also confirmed from the flat-mount experiments. These results were same as those previously noted in mice [25]. Our 10VDD device delivered vasohibin-1 to the retina transsclerally, with results comparable to those seen with intravitreal vasohibin-1 injections. With a less invasive method than that of intravitreal injection and the added advantage of continuous drug delivery, our device may be able to replace invasive intravitreal drug injections. Although there was no significant difference between 10VDD and VDD when we evaluated by FA, a statistically significant effect was observed in only 10VDD, but not VDD when we performed the flat-mount examination. One of the reasons these two do not match exactly may be due to the uncertainty about the FA evaluation, as not only blockage by hemorrhage, but also tissue staining and/or leakage sometimes make evaluation difficult [47]. Further study is needed to determine the exact amounts of vasohibin-1 released from the device, the kinetics of drug distribution, the correlation between drug amount and ocular distribution, and the effects of this regimen on CNV, as well as the appropriate duration of vasohibin-1 release.

Choroidal neovascularization has been reported to be produced by choriocapillaris of the choroidal blood flow [48]. Many effects of choroidal blood flow or RPE may stimulate CNV formation into the retina [49]. Drusen, a preclinical feature of age-related macular degeneration, also stimulates CNV formation [50]. Transscleral anti-CNV drug delivery will be more reasonable than that of intravitreal injection not only from the points of safety, but also from the aspect of CNV pathophysiology. The RPE and RPE-choroid complex are reported to be one to two orders of magnitude slower in drug penetration [21]. When we put our device on the sclera, the drug can pass through the sclera and reach the choroid and RPE earlier than the retina. Between the choroid and neural retina, anti-CNV drugs released from our device may suppress on-going CNV formation. Suprachoroidal bevacizumab was reported to be delivered to the RPE, choroid, and photoreceptors, whereas intravitreal injection distributed more to the inner retina [11]. Olsen et al stressed the importance of delivery of a sustained-release formulation of large molecules to the suprachoroidal space [11]. Our device will offer a safer therapeutic method than those previously reported, especially in the treatment of AMD.

Conclusion

We developed a sustained delivery device for the release of vasohibin-1 in the eye. The released vasohibin-1 showed activity comparable to vasohibin-1 delivered via other methods. When we placed the device on the rat sclera, we found vasohibin-1 released to the sclera, retinal pigment epithelium, and retina. Transscleral vasohibin-1 delivery significantly reduced laser-induced CNV that are comparable as those of effects seen with intravitreal vasohibin-1 injection in the rat eye. Our device will offer a safer therapeutic method than intravitreal injections.

Supporting Information

Figure S1 The size of the devices. The size of the device was 4 mm×4 mm×1.5 mm for the vasohibin-1 releasing assay (A, Device (a)) and 2 mm×2 mm wide ×1 mm high for the rat experiments (A, Device (b)). Because it was very difficult to detect using standard ELISA techniques, we used a larger size device for ELISA. The vasohibin-1 releasing area was 5.44 times larger in Device (a) (3.5 mm×3.5 mm = 12.25 mm^2) than that of Device (b) (1.5 mm×1.5 mm = 2.25 mm^2). Bar: 5 mm. We formulated fluorescein isothiocyanate (FITC) dextran (FD40) as simulated drugs and the device was incubated in a Transwell in 400 μL of PBS at 37°C. To estimate the amounts of FD40 that had diffused out of the Transwells, the fluorescent intensities of the PBS solutions were measured spectrofluorometrically (FluoroscanAscent; Thermo). From the results of a fitting curve (B), we calculated that the releasing rate of the larger device was 0.958 μg/hr/day, whereas the smaller device released 0.28 μg/hr/day; the difference of the releasing rates was calculated as 3.42 (0.958/0.28).
(TIF)

Figure S2 Comparison of FD40DD and FD40 pellet implantations. Rats implanted with FD40DD or FD40 pellets are shown. Devices or pellets were confirmed by color photographs (A and G), after enucleation (C and I), and after device (E) or pellet (K) removal. Mild fibrosis was observed around the devices (C) or pellets (I). FD40 was detected in the device (B), or pellets (H) by fluorescein photography at the site of the implant through the conjunctiva in the live rats during the experiment. When the eyes were enucleated at 1 week after device implantation, little fluorescence was observed in the conjunctiva and surrounding tissues (D, white arrow) in FD40DD-treated rats, whereas strong fluorescence in the conjunctiva was observed in pellet-treated rats (J, white arrow). FD40 was also detected on the sclera after removal of the device (F), but not the pellet (L) (yellow squares indicate the implantation site).
(TIF)

Acknowledgments

The authors alone are responsible for the content and writing of this paper.

Author Contributions

Conceived and designed the experiments: TA NN. Performed the experiments: HO NN HK MN YS NO TN TA. Analyzed the data: HO NN TA. Contributed reagents/materials/analysis tools: NN HK MN TA. Wrote the paper: TA.

References

1. Klein R, Peto T, Bird A, Vannewkirk MR (2004) The epidemiology of age-related macular degeneration. Am J Ophthalmol 137: 486–495.
2. (1986) Argon laser photocoagulation for neovascular maculopathy. Three-year results from randomized clinical trials. Macular Photocoagulation Study Group. Arch Ophthalmol 104: 694–701.
3. Thomas MA, Grand MG, Williams DF, Lee CM, Pesin SR, et al. (1992) Surgical management of subfoveal choroidal neovascularization. Ophthalmology 99: 952–968; discussion 975–956.
4. Eckardt C, Eckardt U, Conrad HG (1999) Macular rotation with and without counter-rotation of the globe in patients with age-related macular degeneration. Graefes Arch Clin Exp Ophthalmol 237: 313–325.
5. Reichel E, Berrocal AM, Ip M, Krell AJ, Desai V, et al. (1999) Transpupillary thermotherapy of occult subfoveal choroidal neovascularization in patients with age-related macular degeneration. Ophthalmology 106: 1908–1914.
6. (1999) Photodynamic therapy of subfoveal choroidal neovascularization in age-related macular degeneration with verteporfin: one-year results of 2 randomized clinical trials – TAP report. Treatment of age-related macular degeneration with photodynamic therapy (TAP) Study Group. Arch Ophthalmol 117: 1329–1345.
7. Grisanti S, Tatar O (2008) The role of vascular endothelial growth factor and other endogenous interplayers in age-related macular degeneration. Prog Retin Eye Res 27: 372–390.
8. Miller JW, Adamis AP, Shima DT, D'Amore PA, Moulton RS, et al. (1994) Vascular endothelial growth factor/vascular permeability factor is temporally and spatially correlated with ocular angiogenesis in a primate model. Am J Pathol 145: 574–584.
9. Pilli S, Kotsolis A, Spaide RF, Slakter J, Freund KB, et al. (2008) Endophthalmitis associated with intravitreal anti-vascular endothelial growth factor therapy injections in an office setting. Am J Ophthalmol 145: 879–882.
10. Amaral J, Fariss RN, Campos MM, Robison WG Jr., Kim H, et al. (2005) Transscleral-RPE permeability of PEDF and ovalbumin proteins: implications for subconjunctival protein delivery. Invest Ophthalmol Vis Sci 46: 4383–4392.
11. Olsen TW, Feng X, Wabner K, Csaky K, Pambuccian S, et al. (2011) Pharmacokinetics of pars plana intravitreal injections versus microcannula suprachoroidal injections of bevacizumab in a porcine model. Invest Ophthalmol Vis Sci 52: 4749–4756.
12. Martin DF, Parks DJ, Mellow SD, Ferris FL, Walton RC, et al. (1994) Treatment of cytomegalovirus retinitis with an intraocular sustained-release ganciclovir implant. A randomized controlled clinical trial. Arch Ophthalmol 112: 1531–1539.
13. Charles NC, Freiberg L (2002) Endophthalmitis associated with extrusion of a ganciclovir implant. Am J Ophthalmol 133: 273–275.
14. Srivastava S, Taylor P, Wood LV, Lee SS, Robinson MR (2004) Post-surgical scleritis associated with the ganciclovir implant. Ophthalmic Surg Lasers Imaging 35: 254–255.

15. Cashman SM, Ramo K, Kumar-Singh R (2011) A non membrane-targeted human soluble CD59 attenuates choroidal neovascularization in a model of age related macular degeneration. PLoS One 6: e19078.
16. Campochiaro PA, Nguyen QD, Shah SM, Klein ML, Holz E, et al. (2006) Adenoviral vector-delivered pigment epithelium-derived factor for neovascular age-related macular degeneration: results of a phase I clinical trial. Hum Gene Ther 17: 167–176.
17. Chevez-Barrios P, Chintagumpala M, Mieler W, Paysse E, Boniuk M, et al. (2005) Response of retinoblastoma with vitreous tumor seeding to adenovirus-mediated delivery of thymidine kinase followed by ganciclovir. J Clin Oncol 23: 7927–7935.
18. Raghava S, Hammond M, Kompella UB (2004) Periocular routes for retinal drug delivery. Expert Opin Drug Deliv 1: 99–114.
19. Smiddy WE, Smiddy RJ, Ba'Aranh B, Flynn HW Jr., Murray TG, et al. (2005) Subconjunctival antibiotics in the treatment of endophthalmitis managed without vitrectomy. Retina 25: 751–758.
20. Yasukawa T, Ogura Y, Tabata Y, Kimura H, Wiedemann P, et al. (2004) Drug delivery systems for vitreoretinal diseases. Prog Retin Eye Res 23: 253–281.
21. Ranta VP, Mannermaa E, Lummepuro K, Subrizi A, Laukkanen A, et al. (2010) Barrier analysis of periocular drug delivery to the posterior segment. J Control Release 148: 42–48.
22. Kunou N, Ogura Y, Yasukawa T, Kimura H, Miyamoto H, et al. (2000) Long-term sustained release of ganciclovir from biodegradable scleral implant for the treatment of cytomegalovirus retinitis. J Control Release 68: 263–271.
23. McHugh AJ (2005) The role of polymer membrane formation in sustained release drug delivery systems. J Control Release 109: 211–221.
24. Kawashima T, Nagai N, Kaji H, Kumasaka N, Onami H, et al. (2011) A scalable controlled-release device for transscleral drug delivery to the retina. Biomaterials 32: 1950–1956.
25. Wakusawa R, Abe T, Sato H, Sonoda H, Sato M, et al. (2011) Suppression of choroidal neovascularization by vasohibin-1, a vascular endothelium-derived angiogenic inhibitor. Invest Ophthalmol Vis Sci 52: 3272–3280.
26. Watanabe K, Hasegawa Y, Yamashita H, Shimizu K, Ding Y, et al. (2004) Vasohibin as an endothelium-derived negative feedback regulator of angiogenesis. J Clin Invest 114: 898–907.
27. Shen J, Yang X, Xiao WH, Hackett SF, Sato Y, et al. (2006) Vasohibin is up-regulated by VEGF in the retina and suppresses VEGF receptor 2 and retinal neovascularization. FASEB J 20: 723–725.
28. Onami H, Nagai N, Machida S, Kumasaka N, Wakusawa R, et al. (2012) Reduction of laser-induced choroidal neovascularization by intravitreal vasohibin-1 in monkey eyes. Retina 32: 1204–1213.
29. Heishi T, Hosaka T, Suzuki Y, Miyashita H, Oike Y, et al. (2010) Endogenous angiogenesis inhibitor vasohibin1 exhibits broad-spectrum antilymphangiogenic activity and suppresses lymph node metastasis. Am J Pathol 176: 1950–1958.
30. Ishikawa Y, Nagai N, Onami H, Kumasaka N, Wakusawa R, et al. (2012) Vasohibin-1 and retinal pigment epithelium. Adv Exp Med Biol 723: 305–310.
31. Tobe T, Ortega S, Luna JD, Ozaki H, Okamoto N, et al. (1998) Targeted disruption of the FGF2 gene does not prevent choroidal neovascularization in a murine model. Am J Pathol 153: 1641–1646.
32. Krzystolik MG, Afshari MA, Adamis AP, Gaudreault J, Gragoudas ES, et al. (2002) Prevention of experimental choroidal neovascularization with intravitreal anti-vascular endothelial growth factor antibody fragment. Arch Ophthalmol 120: 338–346.
33. Yu HG, Liu X, Kiss S, Connolly E, Gragoudas ES, et al. (2008) Increased choroidal neovascularization following laser induction in mice lacking lysyl oxidase-like 1. Invest Ophthalmol Vis Sci 49: 2599–2605.
34. Edelman JL, Castro MR (2000) Quantitative image analysis of laser-induced choroidal neovascularization in rat. Exp Eye Res 71: 523–533.
35. Regillo CD, Brown DM, Abraham P, Yue H, Ianchulev T, et al. (2008) Randomized, double-masked, sham-controlled trial of ranibizumab for neovascular age-related macular degeneration: PIER Study year 1. Am J Ophthalmol 145: 239–248.
36. Sfikakis PP, Theodossiadis PG, Katsiari CG, Kaklamanis P, Markomichelakis NN (2001) Effect of infliximab on sight-threatening panuveitis in Behcet's disease. Lancet 358: 295–296.
37. Ohno S, Nakamura S, Hori S, Shimakawa M, Kawashima H, et al. (2004) Efficacy, safety, and pharmacokinetics of multiple administration of infliximab in Behcet's disease with refractory uveoretinitis. J Rheumatol 31: 1362–1368.
38. Kim H, Csaky KG (2010) Nanoparticle-integrin antagonist G16Y peptide treatment of choroidal neovascularization in rats. J Control Release 142: 286–293.
39. Robinson MR, Lee SS, Kim H, Kim S, Lutz RJ, et al. (2006) A rabbit model for assessing the ocular barriers to the transscleral delivery of triamcinolone acetonide. Exp Eye Res 82: 479–487.
40. Lee SJ, He W, Robinson SB, Robinson MR, Csaky KG, et al. (2010) Evaluation of clearance mechanisms with transscleral drug delivery. Invest Ophthalmol Vis Sci 51: 5205–5212.
41. Pontes de Carvalho RA, Krausse ML, Murphree AL, Schmitt EE, Campochiaro PA, et al. (2006) Delivery from episcleral exoplants. Invest Ophthalmol Vis Sci 47: 4532–4539.
42. Stefansson E, Geirsdottir A, Sigurdsson H (2011) Metabolic physiology in age related macular degeneration. Prog Retin Eye Res 30: 72–80.
43. Kondo M, Sasaki R, Ueno S, Nishizawa Y, Hashimoto N, et al. (2011) Identification of autoantibodies against TRPM1 in patients with paraneoplastic retinopathy associated with ON bipolar cell dysfunction. PLoS One 6: e19011.
44. Thirkill CE, FitzGerald P, Sergott RC, Roth AM, Tyler NK, et al. (1989) Cancer-associated retinopathy (CAR syndrome) with antibodies reacting with retinal, optic-nerve, and cancer cells. N Engl J Med 321: 1589–1594.
45. Chan JW (2005) Paraneoplastic retinopathies and optic neuropathies. Surv Ophthalmol 42: 12–38.
46. Kim SH, Csaky KG, Wang NS, Lutz RJ (2008) Drug elimination kinetics following subconjunctival injection using dynamic contrast-enhanced magnetic resonance imaging. Pharm Res 25: 512–520.
47. Lassota N, Kiilgaard JF, la Cour M, Scherfig E, Prause JU (2008) Natural history of choroidal neovascularization after surgical induction in an animal model. Acta Ophthalmol 86: 495–503.
48. Hayreh SS (2010) Submacular choroidal vascular bed watershed zones and their clinical importance. Am J Ophthalmol 150: 940–941; author reply 941–942.
49. Lutty G, Grunwald J, Majji AB, Uyama M, Yoneya S (1999) Changes in choriocapillaris and retinal pigment epithelium in age-related macular degeneration. Mol Vis 5: 35.
50. Booij JC, Baas DC, Beisekeeva J, Gorgels TG, Bergen AA (2010) The dynamic nature of Bruch's membrane. Prog Retin Eye Res 29: 1–18.

35th Annual International Conference of the IEEE EMBS
Osaka, Japan, 3 - 7 July, 2013

Validation of Echo-Dynamography by Virtual Color Doppler Echocardiography Generated from Phase Contrast Magnetic Resonance Angiography Datasets

Takanori Kojima, Aiko Omori, Hiroyuki Nakajima, Takafumi Kurokawa, Takeyoshi Kameyama and Yoshifumi Saijo, *Member, IEEE*

Abstract— **Echo-Dynamography (EDG) is a smart visualization technique in echocardiography in which two-dimensional distribution of blood flow vectors in cardiovascular system is deduced by applying fluid dynamics theories into Doppler velocity datasets. Previous validation studies such as numerical simulation of free jet model or model circulation were too simple to reproduce unstable and asymmetrical flow in left ventricle. In the present study, virtual color Doppler echocardiography is generated from PC-MRA (phase contrast magnetic resonance angiography) datasets. EDG is applied on virtual Doppler data and the blood flow vectors are compared with those of the original PC-MRA data. EDG-derived blood flow vectors showed similar pattern as the original PC-MRA data when blood flow velocity had high value. The errors were caused from underestimating the magnitude of vortex flow component in the flow field near the boundary of the left ventricular wall. The results also indicated that apical long axis view had small error compared with parasternal long axis view. Despite EDG method causes small errors, it provides important information on blood flow dynamics in most parts.**

I. Introduction

Evaluation of cardiac function has been performed by intracardiac blood flow measurement. For example, diastolic function was assessed by early diastolic filling (E) over /atrial filling (A) ratio and most suitable parameters of CRT (cardiac resynchronization therapy) is set to maximize velocity-time integral of left ventricular outflow.

The blood flow structure in left ventricle (LV) has been assessed by echo-dynamography (EDG) [1-4]. EDG is a smart visualization technique in echocardiography in which two-dimensional distribution of blood flow vectors in cardiovascular system is deduced by applying fluid dynamics theories into Doppler velocity datasets. EDG has been validated by numerical simulation and particle image velocimetry of model circulation [5]. However, these validations were too simple to reproduce unstable and asymmetrical flow in a beating heart. Clinical validation of EDG was performed; EDG was applied on color Doppler echocardiography and the blood flow vectors were compared those obtained with PC-MRA (phase contrast magnetic resonance angiography). The distribution pattern roughly matched each other; however, quantitative analysis was difficult because the observation plane was not completely matched between echocardiography and PC-MRA [6].

In the present study, virtual color Doppler echocardiography is generated from PC-MRA datasets. EDG algorithm is validated by comparing blood flow vectors obtained by EDG applied on virtual Doppler data and those of the original PC-MRA data.

*Research supported by Industry-Academia Collaborative R&D Programs from The Japan Science and Technology Agency.

T. Kojima is with the Graduate School of Biomedical Engineering, Tohoku University, Sendai, Japan (e-mail: takanori.kojima@bme.tohoku.ac.jp).

A. Omori is with the Graduate School of Biomedical Engineering, Tohoku University, Sendai, Japan (e-mail: a.omori@ecei.tohoku.ac.jp).

H. Nakajima is with Tohoku Welfare Pension Hospital, Sendai, Japan (e-mail: hiro1029@sea.plala.or.jp).

T. Kurokawa is with Tohoku Welfare Pension Hospital, Sendai, Japan (e-mail: nenkin_kurokawa@yahoo.co.jp).

T. Kameyama is with the Department of Cardiology, Miyagi Social Insurance Hospital, Sendai, Japan (e-mail: takeyosh@wa2.so-net.ne.jp).

Y. Saijo is with the Graduate School of Biomedical Engineering, Tohoku University, Sendai, Japan (phone: +81-22-717-8514; fax: +81-22-795-7149; e-mail: saijo@ idac.tohoku.ac.jp).

II. Methods

A. Echo-dynamography

A color Doppler movie of the apical three-chamber view containing LV apex, center of mitral leaflets, and center of aortic valve was recorded in a commercially available ultrasound machine (SSD-6500SV, Aloka, Tokyo, Japan) in the left lateral recumbent position. The central frequency was 2.5 MHz and the frame rate was 10 fps.

The processing algorithm of EDG is the following.

First, the LV blood flow is considered as incompressible and three-dimensional (3D) flow. Thus, equation of continuity in the 3D space can be applied.

$$\frac{\partial u}{\partial x}+\frac{\partial v}{\partial y}+\frac{\partial w}{\partial z}=0 \cdots (1)$$

The rest of the components v on the x-y plane can be estimated by integrating continuity equation for incompressible flow along the y-axis as follows:

$$v(x,y)=-\frac{\partial}{\partial x}\int_{y_0^-(x)}^{y} u(x,y')\,\partial y' - \frac{\partial}{\partial z}\int_{y_0^-(x)}^{y} w(x,y')\,\partial y' + v\left(x,y_0^-(x)\right) \cdots (2)$$

In conventional color Doppler echocardiography, the velocity component w in the z direction cannot be measured. In some previous methods, the second term of the equation (2) was ignored assuming w=0. This flow condition is considered as 2D flow. Thus, classical statement of stream function can be applied as equation (3).

$$v(x,y)=-\frac{\partial}{\partial x}\int_{y_0^-(x)}^{y} u(x,y')\,\partial y' \cdots (3)$$

However, LV flow should be considered as 3D flow and classical stream function cannot be applied. In EDG method, the second term of the equation (2) is modeled as equation (4).

$$v(x,y)=-\frac{\partial}{\partial x}\int_{y_0^-(x)}^{y} u(x,y')\,\partial y' + \frac{\partial}{\partial x}\int_{y_0^-(x)}^{y}\left(1-k(x,y')\right)u(x,y')\,\partial y' + \left(1-k(x,y)\right)u(x,y)\tan\kappa \cdots (4)$$

Figure 1 shows an example of EDG representing blood flow velocity vectors.

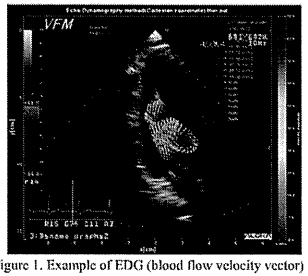

Figure 1. Example of EDG (blood flow velocity vector)

Figure 2 shows an example of EDG representing stream lines.

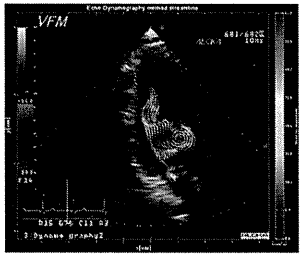

Figure 2. Example of EDG (streamline)

B. PC-MRA

ECG-triggered and breath-hold PC-MRA sequences were obtained from one healthy volunteer. A commercially available 1.5T MRI apparatus (EXCELART Vantage MRT200-PP5, Toshiba Medical, Japan) was equipped for the MRA data acquisition. 2D PC-MRA method with velocity flow encoding of 100cm/s, TR of 24 msec, TE of 10 msec, flip angle of 20 degree, slice thickness of 8 mm, matrix size of 128 (Read out direction) × 256 (Phase encoding direction) and resolution of 2.73 mm × 1.37 mm was used. The cardiac phases such as ejection (E), late systole (LS), early rapid filling (ERF), late rapid filling (LRF), and atrial contraction (AC) phase, were analyzed.

Virtual Doppler velocity is defined as the blood flow components on the radial direction in a polar coordinate system, simply directed to or away from virtual sector probe. Virtual Doppler velocity fields were acquired from various probe positions on the body surface in T2 weighted image (T2WI) (Figure 3).

Figure 3. Virtual color Doppler image generated from PC-MRA datasets. ×: Virtual probe location

C. Definition of the Error

In this study, overall relative errors were calculated according to the following equations [7]:

$$E_{\omega}=\frac{\int_{\Omega}\varepsilon(x,y)\,dS}{\int_{\Omega}\left\|\mathbf{V}_{\mathrm{MRI}}\right\|dS} \cdots (5)$$

$$\varepsilon(x,y)=\left\|\mathbf{V}_{\mathrm{MRI}}-\mathbf{V}_{\mathrm{EDG}}\right\| \cdots (6)$$

where ε shows the point wise error expressed as a function of the Cartesian coordinates (x, y), which was defined as the difference of the absolute values between $\mathbf{V}_{\mathrm{MRI}}$ (original velocity vectors measured by PC-MRA) and $\mathbf{V}_{\mathrm{EDG}}$ (reconstructed velocity vectors obtained with EDG applied on virtual color Doppler echocardiography). Ω is the area of interest. In particular, note that analytical area was limited to LV and left atrium during filling phases when aortic valve is closed, and LV and ascending aorta during ejection phases when mitral valve is closed.

III. Results

Figure 4 shows 2D blood velocity fields measured by PC-MRA and the reconstructed velocity fields with EDG method in ejection, early rapid filling and atrial contraction phases. Virtual probe position located at the apex of LV is expressed as cross (×) on the T2WI image shown in Figure 4.

978-1-4577-0216-7/13/$26.00 ©2013 IEEE

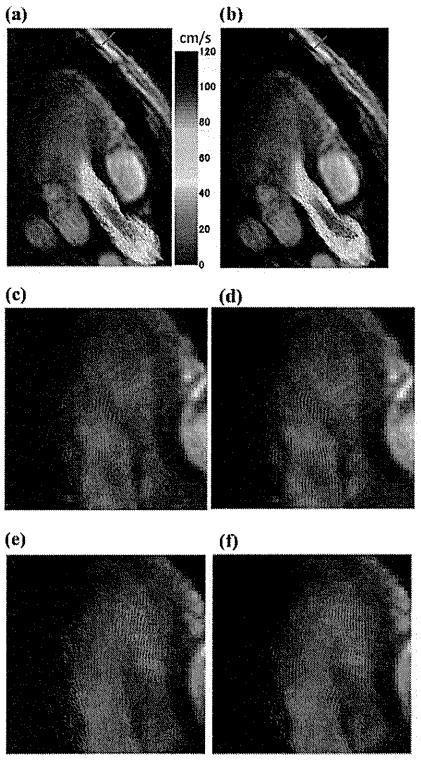

Figure 4. Blood velocity mapping in normal LV comparing the velocity field of the original PC-MRA measurements (PC-MRA) and the velocity field of EDG applied on virtual color Doppler echocardiography (EDG). (a) PC-MRA, (b) EDG at ejection phase, (c) PC-MRA, (d) EDG at early rapid filling, (e) PC-MRA, (f) EDG at atrial contraction. The vectors indicate the direction and magnitude of the velocity as coded in the color bars (cm/s). The cross (×) located at the apex of LV on T2WI represents the virtual probe position.

Velocity distribution pattern showed no significant difference by qualitative visual observations.

Table.1 represents the overall error parameter E_{tot} at five cardiac phases in the same probe position in Figure 4.

Phase	E	LS	ERF	LRF	AC
E_{tot} [%]	18.0	27.7	28.4	24.0	30.0

Table.1 Error parameters at five cardiac phases (E: ejection, LS: late systole, ERF: early rapid filling, LRF: late rapid filling, AC: atrial contraction)

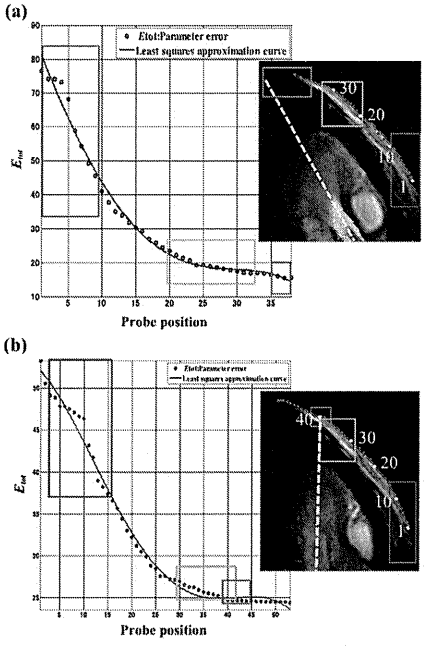

Figure 5. Relation between the error parameter E_{tot} and the virtual probe position at ejection phase (a) and early rapid filling phase (b). Blue circle shows values of E_{tot} at each probe position. Right figures show the original velocity fields measured with PC-MRA and the virtual probe position.

Graphs in Figure 5 show the relation between error parameter E_{tot} and the virtual probe position at the ejection phase and early rapid filling phase. Blue circles show values of E_{tot} at each probe position. The green curves are quadratic least square fits to the data.

The probe positions were numbered from the parasternal portion to the LV apical portion. Virtual probe position is expressed as the red circle in the right figures showing original velocity fields measured with PC-MRA. Yellow circles show the virtual probe position numbered as 1, 10, 20, 30, and 40. Apical three chamber view is obtained when the virtual probe is located in the orange-colored boxes. Left parasternal long axis view is obtained when the virtual probe is located in the red-colored boxes.

Error parameter depended on the virtual probe position at both ejection phase and early rapid filling phase. White dashed lines indicate the main flow axis at each phase. E_{tot} was minimized when the virtual probe is located in the blue-colored boxes where main flow axis aligns parallel to the virtual ultrasonic beam.

IV. Discussion

In comparison with original blood flow vectors obtained with PC-MRA, the error of EDG was smallest in the ejection phase among five cardiac phases. In the ejection phase, LV outflow showed the fastest flow and the flow was nearly parallel to the ultrasonic beam. In the early rapid filling phase, the error was relatively small and a large vortex was observed in the center of LV. In EDG algorithm, vortex flow and basic flow is separated in the first step. In these cardiac phases, vortex flow and basic flow might be clearly separated.

In our previous studies [2-4], apical three-chamber view showed clear and smooth blood flow distribution compared to other views such as apical four-chamber view or parasternal long axis view. In the present study, the error was minimized when the virtual probe point was located at the "real" LV apex. It is assumed that small errors result from when a visible vortex and a main flow have no contradiction in flow fields observed from the LV apex. On the other hand, errors were caused from underestimating the magnitude of vortex flow component in the flow field near the LV boundary. The error parameter was max at the atrial contraction phase. However, the absolute value of blood flow velocity was low in atrial contraction phase. Thus, the flow pattern was not significantly different from original PC-MRA in the visual observation.

The clinical significance of EDG, especially quantitative analysis of LV vortex was already shown in our previous study [6]. The vortex at mid diastolic phase was strongly affected by early diastolic filling while the vortex at isometric contraction was affected by atrial filling. EDG gained a new insight on relationship between systole and diastole from the view point of LV blood flow dynamics. The pump function has been mainly discussed with myocardial contractility based on the measurement of classical ejection fraction, myocardial strain obtained with tissue Doppler or speckle tracking. Discrepancies between myocardial contractility and LV blood flow obtained with EDG may clarify the nature of heart failure.

V. Conclusion

Virtual color Doppler echocardiography was generated from PC-MRA datasets. EDG algorithm was validated by comparing blood flow vectors derived by applying EDG on virtual Doppler data and original PC-MRA data. EDG-derived blood flow vectors showed similar pattern as the original PC-MRA data when blood flow velocity had high value. The errors were caused from underestimating the magnitude of vortex flow component in the flow field near the LV boundary. The results also indicated that apical long axis view had small error compared with parasternal long axis view.

As echocardiography is a real-time, non-invasive and repeatable medical imaging technique, EDG may provide important information on blood flow dynamics in clinical settings.

References

[1] Ohtsuki, S. and M. Tanaka. The flow velocity distribution from the Doppler information on a plane in three-dimensional flow. *Journal of Visualization*. 2006; 9(1):69-82.

[2] Tanaka M, Sakamoto T, Sugawara S, Nakajima H, Katahira Y, Ohtsuki S, Kanai H., Blood flow structure and dynamics, and ejection mechanism in the left ventricle: analysis using echo-dynamography. *J Cardiol*. 2008; 52(2): 86-101.

[3] Tanaka M, Sakamoto T, Sugawara S, Nakajima H, Kameyama T, Tabuchi H, Katahira Y, Ohtsuki S, Kanai H., Physiological basis and clinical significance of left ventricular suction studied using echo-dynamography. *J Cardiol*. 2011; 58(3):232-44.

[4] Nakajima H, Sugawara S, Kameyama T, Tabuchi H, Ohtsuki S, Tanaka M, Saijo Y. Location of flow axis line in the left ventricle and its interaction with local myocardial motion. *J Echocardiogr*. 2011; 9(1): 24-27.

[5] Uejima T, Koike A, Sawada H, Aizawa T, Ohtsuki S, Tanaka M, Furukawa T, Fraser AG. A new echocardiographic method for identifying vortex flow in the left ventricle: numerical validation. *Ultrasound Med Biol*. 2010; 36(5): 772-788.

[6] Kojima T, Kameyama T, Nakajima H, Khmyrova E, Kurokawa T, Saijo Y. Evaluation of vortex flow in left ventricle by echo-dynamography and phase contrast magnetic resonance angiography. *Conf Proc 34th IEEE Eng Med Biol Soc*. 2012:2676-9.

[7] Garcia D, Del Alamo JC, Tanne D, Yotti R, Cortina C, Bertrand E, Antoranz JC, Perez-David E, Rieu R, Fernandez-Aviles F, Bermejo J. Two-dimensional intraventricular flow mapping by digital processing conventional color-Doppler echocardiography images. *IEEE Trans Med Imaging*. 2010; 29(10):1701-13.

Journal of Controlled Release 172 (2013) 879–884

Contents lists available at ScienceDirect

Journal of Controlled Release

journal homepage: www.elsevier.com/locate/jconrel

Photothermal therapy of tumors in lymph nodes using gold nanorods and near-infrared laser light

Tatsuki Okuno [a], Shigeki Kato [a], Yuriko Hatakeyama [a], Junnosuke Okajima [b], Shigenao Maruyama [b], Maya Sakamoto [c], Shiro Mori [d], Tetsuya Kodama [a,*]

[a] Laboratory of Biomedical Engineering for Cancer, Department of Biomedical Engineering, Graduate School of Biomedical Engineering, Tohoku University, 4-1 Seiryo, Aoba, Sendai, Miyagi 980-8575, Japan
[b] Institute of Fluid Science, Tohoku University, 2-1-1 Katahira, Aoba Ward, Sendai, Miyagi 980-8577, Japan
[c] Department of Oral Diagnosis, Tohoku University Hospital, 1-1 Seiryo, Aoba Ward, Sendai, Miyagi 980-8575, Japan
[d] Department of Oral and Maxillofacial Surgery, Tohoku University Hospital, 1-1 Seiryo, Aoba Ward, Sendai, Miyagi 980-8575, Japan

ARTICLE INFO

Article history:
Received 13 August 2013
Accepted 10 October 2013
Available online 19 October 2013

Keywords:
Lymph node metastasis
Photothermal therapy
Gold nanorods
Plasmon resonance

ABSTRACT

Lymph node dissection for regional nodal metastasis is a primary option, but is invasive and associated with adverse effects. The development of non-invasive therapeutic methods in preclinical experiments using mice has been restricted by the small lymph node size and the limited techniques available for non-invasive monitoring of lymph node metastasis. Here, we show that photothermal therapy (PTT) using gold nanorods (GNRs) and near-infrared (NIR) laser light shows potential as a non-invasive treatment for tumors in the proper axillary lymph nodes (proper-ALNs) of MXH10/Mo–*lpr/lpr* mice, which develop systemic swelling of lymph nodes (up to 13 mm in diameter, similar in size to human lymph nodes). Tumor cells were inoculated into the proper-ALNs to develop a model of metastatic lesions, and any anti-tumor effects of therapy were assessed. We found that GNRs accumulated in the tumor in the proper-ALNs 24 h after tail vein injection, and that irradiation with NIR laser light elevated tumor temperature. Furthermore, combining local or systemic delivery of GNRs with NIR irradiation suppressed tumor growth more than irradiation alone. We propose that PTT with GNRs and NIR laser light can serve as a new therapeutic method for lymph node metastasis, as an alternative to lymph node dissection.

1. Introduction

Regional lymph node dissection is considered a priority when tumor metastases are detected by imaging modalities (ultrasound, CT, MRI or PET) [1,2], provided that the lymph nodes are resectable and the patient fit for surgery [3]. However, this is a highly invasive procedure. Since the therapeutic efficacy of radiotherapy or chemotherapy is relatively low, novel, minimally-invasive treatments for lymph node metastasis are greatly needed.

Photothermal therapy (PTT) is less invasive than radiotherapy, chemotherapy and surgical management [4]. In PTT, optical energy is converted into heat by tissue absorption, causing irreversible tissue damage through thermal denaturing of proteins (and DNAs) and tissue coagulation [5]. Gold nanoparticles, which are non-toxic, non-immunogenic, stable and biocompatible [6], can facilitate PTT by absorbing light, and minimize collateral damage to normal tissue by accumulating near a tumor through bioconjugation [5]. Near-infrared (NIR) laser light has a 'therapeutic window' corresponding to a wavelength band that is minimally absorbed by the blood and soft tissues and does not excite autofluorescence [7]. Since NIR laser light can penetrate soft tissues to depths exceeding 5 cm [8], its combination with gold nanoparticles offers a novel treatment for cancer. Gold nanoparticles exist as varying structures, including nanocages [5], nanowires [9], silica-cored nanoshells and nanorods [10]. Gold nanorods (GNRs) have two surface plasmon absorption bands: a long-wavelength (800–900 nm) and weaker short-wavelength (~500 nm) band due to longitudinal and transverse oscillation of electrons, respectively [11]. The absorption maximum of the longitudinal band shifts to longer wavelengths with increasing aspect-ratio; by selecting GNRs with an aspect-ratio appropriate for the NIR wavelength, effective treatment of cancer may be possible. Several types of GNR have been developed to increase tumor selectivity and efficacy, including GNRs conjugated to the anti-epidermal growth factor receptor [11,12], polyacrylic acid-coated GNRs [13], doxorubicin-loaded GNRs [14] and GNRs conjugated with arginine–glycine–aspartic acid peptides [15]. The selectivity of GNRs is improved further by the enhanced permeability and retention (ERP) effect [16].

In mice, PTT and GNRs have been assessed for the treatment of solid tumors [10,15,17–20], but not lymph node metastases, in part because the induction and detection of metastases in murine lymph nodes are challenging due to their small size (a few millimeters) [21]. Previously, we have used the MRL/MpJ–*lpr/lpr* (MRL/lpr) mouse as an animal model of lymph node metastasis, because its lymph nodes swell to a size similar to that in humans. However, the MRL/lpr strain is also utilized as a model of autoimmune diseases, and has the major disadvantage that lethal nephritis occurs at the same age (4–5 months) as lymph node swelling [22].

Recently, we developed a recombinant MXH10/Mo–*lpr/lpr* (MXH10/Mo/lpr) strain (by intercrossing MRL/lpr and C3H/HeJ–*lpr/lpr* mice) that shows widespread lymph node swelling at only 2.5–3 months of age, with lymph nodes as large as 10 mm; both the lymph node size and the onset of swelling are consistent and predictable. Moreover, these mice do not develop severe glomerulonephritis and vasculitis [23], and have a longer lifespan than MRL/lpr mice. Here, we have induced tumor development in the proper axillary lymph nodes (proper-ALNs) of MXH10/Mo/lpr mice, and evaluated the use of PTT in combination with GNRs for the treatment of these tumors.

2. Materials and methods

All *in vivo* studies were approved by the Institutional Animal Care and Use Committee of Tohoku University.

2.1. Gold nanorods

Bare gold nanorods (bareGNRs) (aspect ratio: 6.6; surface plasmon resonance (SPR) peak: 1050 nm; 30-HAR-1064) and neutravidin polymer-conjugated gold nanorods (GNRs) (aspect ratio: 6.7; SPR peak: 1065 nm; axial diameter: 10 nm; length: 67 nm; D12-1064-PN-50) were used (Nanopartz). Fluorescent GNRs (FluoGNRs) were prepared by conjugation (30 min, room temperature) of GNRs (12.4×10^{12} particles/mL in phosphate-buffered saline [PBS]) with Atto 590-biotin (excitation: 598 nm; emission: 624 nm; Sigma-Aldrich); excess dye was removed by three centrifugation (5000 ×g, 5 min) and washing steps. The zeta potentials of the GNRs (6.0×10^{10} particles/mL in distilled water) were measured (ELSZ-2 analyzer; Otsuka) as: bareGNRs, 46.54 ± 0.69 mV; GNRs, −13.79 ± 1.33 mV; and FluoGNRs, −16.65 ± 2.11 mV ($n = 3$ for each). GNR absorption spectra were measured using a UV-visible near-infrared spectrophotometer (V-7200; JASCO). FluoGNR configuration (6.0×10^{10} particles/mL in distilled water) was examined with a transmission electron microscope (HT7700; Hitachi) operated at 80 kV.

2.2. Cell culture

KM-Luc/GFP cells [1], which stably express a fusion of the luciferase (Luc) and enhanced-green fluorescent protein (EGFP) genes, were cultured in Complete Medium, consisting of Dulbecco's Modified Eagle Medium supplemented with 10% fetal bovine serum containing 1% L-glutamine–penicillin–streptomycin (Sigma-Aldrich) and 0.5% Geneticin G418 (Wako). The absence of *Mycoplasma* contamination was confirmed with a *Mycoplasma* detection kit (R&D Systems).

2.3. Mice

MXH10/Mo/lpr mice, established by intercrossing MRL/lpr and C3H/HeJ–*lpr/lpr* (C3H/lpr) strains [23], were bred and maintained at the Institute for Animal Experimentation, Graduate School of Medicine, Tohoku University. Seventy-six mice were used (weight, 25–35 g; age, 11–14 weeks). The longitudinal diameter of the proper-ALN, measured using a digital caliper, was 9.76 ± 0.35 mm ($n = 6$).

2.4. Induction of metastasis in the proper-ALN

Tumor development in mice ($n = 57$) was induced by injection into the proper-ALN of 3.3×10^5 KM-Luc/GFP cells/mL, suspended in a mixture of 10 μL PBS (Ca^{2+}- and Mg^{2+}-free) and 20 μL of 400 mg/mL Matrigel (Collaborative Biomedical Products), under the guidance of a high-frequency ultrasound imaging system (Vevo770; VisualSonics) with a 25 MHz transducer (RMV-710B). To measure the luciferase activities of tumors growing in the proper-ALNs, luciferin (150 mg/kg; Promega) was injected intraperitoneally under anesthesia (2% isoflurane in oxygen). 10 min after injection, luciferase bioluminescence was measured for 30 s using an *in vivo* luminescence imaging system (IVIS; Xenogen); this procedure was carried out on days 2, 3, 4, 5, 7 and 9 post-inoculation. The proper-ALN size was measured using an *in vivo* high-resolution three-dimensional microimaging system (VEVO770; VisualSonics) with a 25 MHz transducer (RMV-710B; axial resolution 70 μm, focal length 15 mm) set at 50% transmission power [24].

2.5. Blood biochemistry investigations

The toxicity of systemic GNR injection was evaluated using serum biochemistry tests. Four mice were injected intravenously with GNRs (12.4×10^{12} particles/mL, 100 μL), and four controls with PBS (100 μL). On day 17 after injection, blood samples from the caudal vena cava (taken under general anesthesia) were centrifuged (2000 ×g, 5 min) to obtain serum. Hepatic and renal injuries were evaluated from serum measurements of total bilirubin (T-BIL), alanine aminotransferase (ALT), aspartate aminotransferase (AST) and blood urea nitrogen (BUN) (Oriental Yeast).

2.6. GNR Biodistribution

Mice were injected intravenously with GNRs (12.4×10^{11} particles/mL) in PBS, and sacrificed after 12 h, 24 h or 17 days ($n = 3$ for each). Blood was drawn from the abdominal aorta, and the organs and tissues quickly removed and freeze-dried for 20 h. Samples in nitrohydrochloric acid were heated (160 °C for 5 min, 190 °C for 45 min), dispensed into 25 mL PBS, and analyzed for metal concentration by inductively-coupled plasma mass spectrometry (ICP–MS, HP4500, Hitachi). Values for each sample were divided by the quantity of GNRs injected to obtain a percentage (%).

2.7. NIR laser light irradiation

Laser light of 1.5 W/cm² from a continuous Nd: YVO4 air-cooled laser (1064 nm; beam diameter: TEM_{00}, 0.6 mm; CYD-010-TUBC; Neoarc) was delivered to the target site by an optical fiber (fiber diameter: 400 μm; collimator diameter: 20 mm). The collimator head was fixed to a three-dimensional stage control system (Mark-204-MS; Sigma Koki). The temperature at the irradiated site was measured by functional thermography (1.07 mrad spatial resolution, 0.05 °C minimum temperature resolution; TVS-500; Nippon Avionics).

2.8. Treatment of tumors in the proper-ALNs with PTT

To evaluate the anti-tumor effects of laser irradiation (1.5 W/cm², 180 s) and local/systemic GNR delivery, luciferase activities of tumors in the proper-ALNs were measured on days 2, 3, 4, 5, 7 and 9 after tumor inoculation. The proper-ALN volume was measured on days 0, 6 and 9 (Vevo770 high-frequency ultrasound system). Based on studies of human skin burns, the possible occurrence of skin burning was evaluated through macroscopic observations of redness, blistering, ulceration, and full-thickness necrosis of the skin.

* Corresponding author at: Laboratory of Biomedical Engineering for Cancer, Graduate School of Biomedical Engineering, Tohoku University, 4-1 Seiryo, Aoba Ward, Sendai, Miyagi 980-8575, Japan. Tel./fax: +81 22 717 7583.
E-mail address: kodama@bme.tohoku.ac.jp (T. Kodama).

0168-3659/$ – see front matter © 2013 Elsevier B.V. All rights reserved.
http://dx.doi.org/10.1016/j.jconrel.2013.10.014

NANOMEDICINE

2.8.1. Local delivery of GNRs

In the control group ($n = 6$), 30 μL saline was injected intranodally on days 3 and 4 after tumor inoculation. In the GNRs group ($n = 6$), 30 μL GNRs (3.6×10^{12} GNRs/mL) was injected into the proper-ALN on day 3. In the laser group ($n = 6$), the proper-ALN was injected with 30 μL PBS on day 3, and irradiated with NIR light on days 3 and 4. In the laser + GNRs group ($n = 6$), the proper-ALN was injected with 30 μL GNRs (3.6×10^{12} GNRs/mL) on day 3, and irradiated with NIR light on days 3 and 4.

2.8.2. Systemic delivery of GNRs

In the control group ($n = 6$), 100 μL saline was injected intravenously on day 2. In the GNRs group ($n = 6$), 100 μL GNRs in saline (14.4×10^{12} GNRs/mL) was injected intravenously. In the laser group ($n = 6$), 100 μL saline was injected intravenously, and the proper-ALNs irradiated with NIR light on days 3 and 4. In the laser + GNRs group ($n = 6$), 100 μL GNRs in saline (14.4×10^{12} GNRs/mL) was injected intravenously, and the proper-ALNs irradiated with NIR light on days 3 and 4.

2.9. Histological analysis

Frozen sections of lymph nodes were fixed (4% paraformaldehyde, 15 min, room temperature) and washed (PBS). The cytotoxic area was analyzed following hematoxylin and eosin (HE), 4′,6-diamidino-2-phenylindole (DAPI) and CD31 staining. For CD31 staining, purified rat anti-mouse CD31 primary antibody (MED13.3; BD Pharmingen) was diluted (1:100) in PBS with 3% bovine serum albumin and 0.1% Triton-X, and applied overnight at 4 °C. After washing (PBS), the slides were incubated (40 min, 4 °C) with Alexa 488-conjugated goat anti-rat secondary antibody (1:500; Life Technologies) and DAPI (100 ng/mL). After washing (PBS), sections were mounted with Vectorshield (Vector). Histological images were captured using a fluorescence microscope (BX51; Olympus), digital camera (DP72; Olympus) and Photoshop CS3 (Adobe). For paraffin-embedded samples, harvested lymph nodes were fixed overnight (10% formaldehyde, 4 °C; Rapid Fixative; Kojima Chemical Industry), dehydrated, embedded in paraffin, sectioned (2–4 μm serial sections), stained with HE, and analyzed using a microscope (BX51; Olympus) and digital camera (DP72; Olympus).

2.10. Statistical analysis

Data are presented as the mean ± SD or SEM. Statistical differences were analyzed using the Kruskal–Wallis and Steel tests. $P < 0.05$ was considered indicative of statistical significance.

3. Results

First, we investigated GNR biodistribution 12 h, 24 h and 17 days after intravenous injection ($n = 3$) (Fig. 1A). The GNR level (% initial dose) in the liver was 30–40% at each time point, with much lower accumulation in the spleen and kidney. Accumulation in the proper-ALN was approximately 0.01% at 24 h with tumor present, but negligible in the absence of tumor. Accumulation of FluoGNRs in the tumor was confirmed by fluorescence microscopy: Fig. 1Ba shows representative HE staining, and Fig. 1Bb presents a corresponding image with nuclei stained by DAPI, CD31-positive cells stained green, and FluoGNRs detected as red. Table 1 shows the evaluation of GNR toxicity (17 days after injection) from changes in body weight and serum biochemistry investigations. There were no significant differences in body weight and serum T-BIL, ALT, AST and BUN between control mice and those administered GNRs.

Next, we investigated the effect of laser light irradiation on tumors in lymph nodes, compared with local and systemic delivery of GNRs. Fig. 2A shows representative thermographic images of proper-ALNs containing tumors: the local rise in temperature induced by laser irradiation was further increased by GNR administration, with local

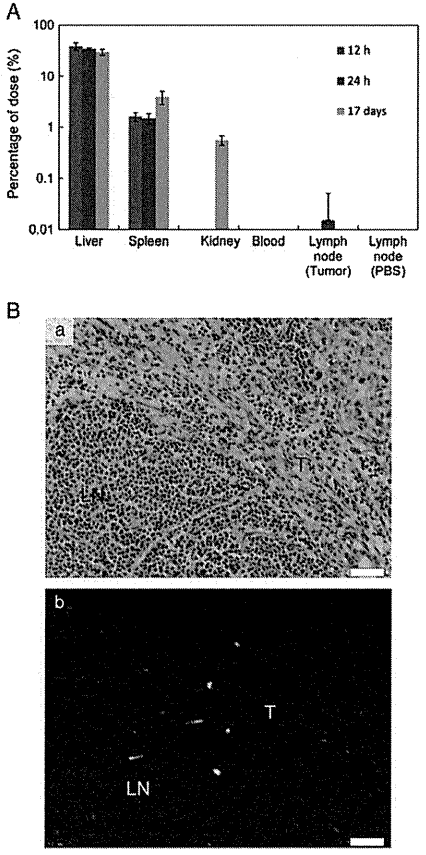

Fig. 1. Uptake of GNRs into organs. A. Biodistribution of the GNRs, injected intravenously 2 days after tumor inoculation into the proper-ALNs. GNR uptake into organs was measured 12 h, 24 h and 17 days after injection. Hepatic uptake was significantly higher than that of other organs. GNR uptake into the tumor in the proper-ALNs was detected 24 h after injection. Mean ± SD values are shown ($n = 3$). B. Histological analysis of the proper-ALNs containing tumor. (a) HE staining, (b) overlay image. GNRs are evident in the tumor mass, independent of CD31-positive blood vessels. Blue: nuclei stained with DAPI; green: CD31-positive cells (Ex: 495 nm, Em: 520 nm); red: FluoGNRs (Ex: nm, Em: nm). Scale bar = 40 μm. T: spindle-shaped tumor cells growing invasively into lymph node tissue; LN: intact lymph node tissue.

delivery of GNRs slightly superior to systemic delivery. Fig. 2B illustrates the increment in the maximum temperature from $\Delta T = 0$ (36 °C): the temperature at 3 min reached 46 °C for laser irradiation alone, 51 °C for laser irradiation + GNRs (local delivery), and 50 °C for laser irradiation + GNRs (systemic delivery).

The cytoreductive effects of PTT were assessed using bioluminescence imaging and high-frequency ultrasound systems. Fig. 3A presents the changes in luciferase activities over time. Compared with the control group, the luciferase activities of the laser + GNRs groups (both local and systemic) were significantly lower on day 4, and that of the laser + GNRs (local) group was significantly lower on day 5 ($P < 0.05$,

Table 1
Evaluation of GNR toxicity.

	Control	GNRs	Statistical significance
T-BIL (mg/dL)	0.05 ± 0.01	0.03 ± 0.01	NS
ALT (IU/L)	69.75 ± 8.06	58.75 ± 8.61	NS
AST (IU/L)	172.67 ± 16.94	155.25 ± 19.93	NS
BUN (mg/dL)	32.00 ± 3.02	49.98 ± 13.32	NS
Body weight change (g)	2.80 ± 0.43	1.75 ± 1.38	NS

Blood samples were obtained on day 17. Values represent the mean ± SEM ($n = 4$). NS, not significant; T-BIL, total bilirubin; ALT, alanine aminotransferase; AST, aspartate aminotransferase; BUN; blood urea nitrogen.

Steel test). Although irradiation with laser light was carried out on days 3 and 4 for both local and systemic GNR delivery, tumor growth was inhibited up to day 9 (Fig. 3A and B). As shown in Fig. 3C and D, the proper-ALN size increased approximately 2-fold over the 9-day study period in the control group; this is consistent with the normal lymph node tissue of the proper-ALN being partially replaced by infiltrating tumor cells, resulting in a noticeable, but not substantial, increase in the proper-ALN size. However, the proper-ALN size did not change significantly in the laser + GNRs (systemic) group (Steel test) (Fig. 3C and D), despite the fact that the luciferase activity was increased (Fig. 3A). This suggests that tumor necrosis following the administration of laser light and GNRs limited the volume growth of the lymph node.

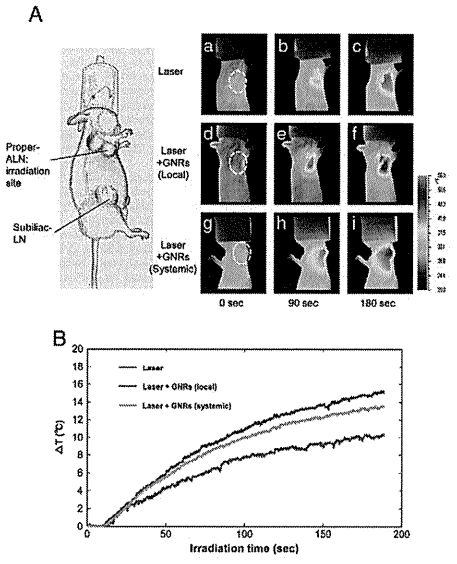

Fig. 2. Laser irradiation of tumors in the proper-ALNs. A. Anatomical and thermographic images of tumors in the proper-ALNs, irradiated on day 3. (a, b, c): laser light alone; (d, e, f): laser light with local GNR delivery; (g, h, i): laser light with systemic GNR delivery. (a, d, g): irradiation time 0 s; (b, e, h): irradiation time 90 s; (c, f, i): irradiation time 180 s. The dashed regions in (a), (d) and (g) indicate proper-ALN regions. The longitudinal diameter of the proper-ALN, measured using a digital caliper, was 9.76 ± 0.35 mm ($n = 6$). B. Increment in the maximum temperature, from $\Delta T = 0$ (36 °C), against time, measured by thermography. At 3 min, the temperature reached 46 °C for laser irradiation alone, and approximately 51 °C for laser irradiation with GNRs (either local or systemic).

The assessment of skin burning revealed that there were no obvious skin lesions in the laser alone group, full-thickness necrosis of the skin in 33.3% of the laser + GNRs (systemic) group, and full-thickness necrosis of the skin in all animals of the laser + GNRs (local) group. The extent of the tissue damage induced by each treatment method was assessed using histological techniques. NIR laser light was irradiated in the direction of the arrows shown in Fig. 4. Lymph nodes of the control group, which had been inoculated with tumor cells, demonstrated progressive proliferation and invasion of spindle-shaped tumor cells (Fig. 4A,B,C). In lymph nodes treated with laser irradiation alone, both lymphatic tissue and tumor in the irradiated area showed evidence of coagulative necrosis, characterized by nuclear debris and pyknotic cells surrounded by an eosinophilic necrotic mass at the periphery (Fig. 4D,E,F). However, proliferation of tumor cells was still discernible outside the area of irradiation (Fig. 4F). Lymph nodes treated locally with GNRs plus laser irradiation also showed a localized region of necrosis (Fig. 4G,H,I), although this seemed more extensive than that with laser irradiation alone (Fig. 4G). In lymph nodes treated with systemic administration of GNRs plus laser irradiation, the findings were similar to those observed with local GNR delivery (Fig. 4J,K,L).

4. Discussion

The present study is the first to show, in MXH10/Mo/lpr mice that develop systemic swelling of lymph nodes to sizes similar to those in humans, that lymph node metastasis may be treated with PTT consisting of NIR laser light and GNRs. The anti-tumor effects of PTT with systemic delivery of GNRs (injection into the tail vein), as indicated by changes in the luciferase activity, were smaller than those achieved using local delivery (injection into the proper-ALN), but larger than those of NIR laser irradiation alone. A significant anti-tumor effect was observed on day 3, followed by an inhibition of tumor growth (Fig. 3A and B). This inhibition of tumor growth was achieved with accumulation in the proper-ALN of only 0.01% of the total GNR dose administered, with most of the GNRs accumulating into non-target sites such as the liver, spleen and reticuloendothelial system for 17 days without severe side effect (Fig. 1, Table 1) [25]. It is notable that the change in lymph node volume, as shown in Fig. 3C and D, does not serve as a sensitive parameter of the anti-tumor effect, as compared with luciferase activity. This is partly because the normal lymph node tissue is partially replaced by infiltrating tumor cells, causing only a slight increase in nodal size [1], and partly because necrosis of tumor cells by laser irradiation does not contribute substantially to a decrease in lymph node volume over a short period of time.

In the present study, tumor cells were injected into the proper-ALNs so that they subsequently developed in the lymph node as a solid tumor. However, in the establishment of metastasis in a patient with a malignant tumor, the tumor cells metastasize into the marginal sinus *via* the afferent lymphatic vessel, and invade into the cortex and paracortex, and then into the medulla [1]. Furthermore, blood vessels in non-metastatic lymph nodes may increase in size and number, while lymph vessels in the region of non-metastatic lymph nodes decrease their total size and may collapse due to the expanding primary tumor [1]. Therefore, the accumulation of GNRs and the subsequent anti-tumor effect observed in the present study may differ from that which would occur in lymph nodes with a true metastatic tumor. Thus, the anti-tumor actions of PTT with GNRs on lymph nodes with true metastases require further investigation.

The tumor in the lymph node was irradiated with NIR laser light at 1.5 W/cm^2 for 3 min. Laser irradiation alone increased the temperature in the proper-ALN to more than 46 °C, while the addition of local and systemic delivery of GNRs resulted in temperature rises to over 50 °C (Fig. 2B). Thermal damage occurs up to a depth of 10 mm (Fig. 4) [26]. It was notable that the temperature increment was similar for local and systemic injection of GNRs (Fig. 2), despite the fact that local injection would be expected to result in a higher concentration of

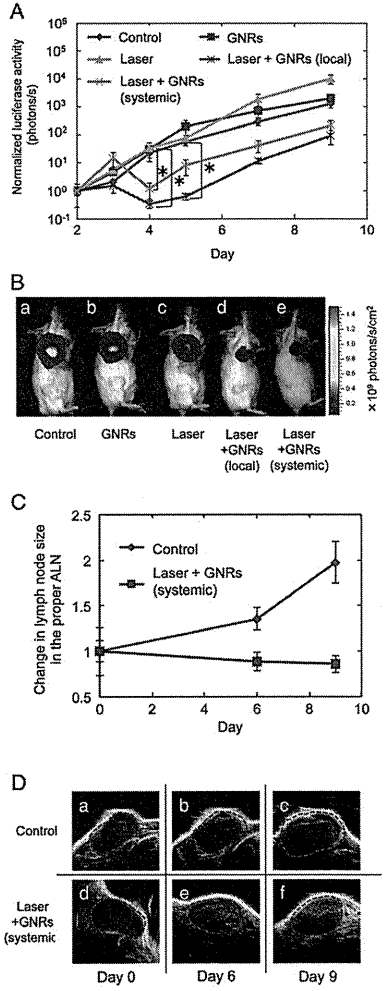

Fig. 3. *In vivo* anti-tumor effects of NIR laser light and GNRs. A. Luciferase activities (bioluminescence imaging) in the proper-ALNs, normalized to that on day 2. Significant differences between groups (* $P < 0.05$, Steel test) were detected on day 4 (control *vs.* laser + GNRs (local); control *vs.* laser + GNRs (systemic)) and day 5 (control *vs.* laser + GNRs (local)). Mean ± SD values are shown ($n = 6$). B. Representative images of the tumor in the proper-ALN observed using an *in vivo* bioluminescence imaging system on day 9. C. Changes in the proper-ALN size over time in the control and laser + GNRs (systemic) groups, assessed using three-dimensional high-frequency ultrasound. The values were normalized to those on day 0. On days 6 and 9, lymph node size had increased in the control group, but not in the laser + GNRs (systemic) group. Mean ± SD values are shown ($n = 6$). D. Two-dimensional high-frequency ultrasound images, showing temporal changes in the lymph node size in the control and laser + GNRs (systemic) groups. The dashed regions indicate proper-ALN regions.

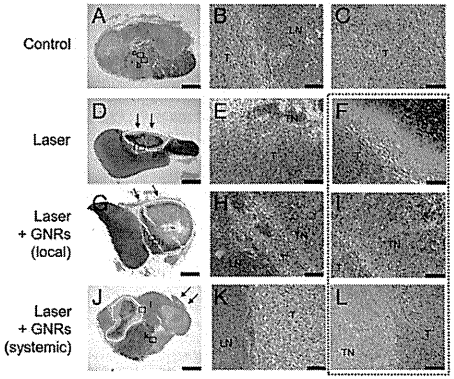

Fig. 4. Histochemical features. The lymph node inoculated with tumor cells and not treated with PTT (control) showed progressive proliferation and invasion of spindle-shaped tumor cells (A, B, C). The node treated by laser irradiation alone (laser) showed coagulative necrosis in the irradiated area, with nuclear debris and pyknotic cells surrounded by an eosinophilic necrotic mass (D, E, F). Outside the area of laser irradiation, tumor cell proliferation was discernible (F). The node treated by local GNR injection plus laser irradiation (laser + GNRs (local)) showed similar necrosis (G, H, I), although the necrotic area was more extensive than that of the lymph node treated with laser irradiation alone (G). In the lymph node treated by systemic GNR administration plus laser irradiation (laser + GNRs (systemic)), the histopathological findings were similar to those for local GNR injection (J, K, L), although the entire irradiated area showed extensive necrosis of lymphatic tissue and tumor; nonetheless, residual viable tumor cells remained. Sections were stained with HE on day 9 after tumor inoculation into the proper-ALNs. The boxed areas in (A), (D), (G), (J) are presented at higher magnification in the middle and right panels. Arrows: direction of the NIR laser light. Bar (left to right): 2 mm, 100 μm, 100 μm. T: tumor; TN: tumor necrosis; LN: lymph node tissue. The solid regions in (D), (G) and (J) indicate TN regions. The dashed line circumscribing (F), (I) and (L) highlights images containing T and TN regions.

GNRs. This is likely due to the characteristics of thermography, which is limited to measuring the surface temperature of the material. Thus, even if the amount of heat generated deeper in the structure was different between systemic and local injection of GNRs, this difference could not be measured with thermography. In addition, heat flow from inside the lymph node to the surface is inhibited by the blood flow in the skin, limiting the increase in the surface temperature.

The assessment of skin burning showed no obvious skin lesions for laser alone, full-thickness necrosis of the skin in 33.3% of the laser + GNRs (systemic) group, and full-thickness necrosis of the skin in all animals of the laser + GNRs (local) group, indicating that GNRs may have leaked into the tissue close to the skin. Alternatively, the dose of GNRs administered may influence the occurrence of burns. However, despite the increased temperature and resulting irreversible tissue damage, the tumor was not completely destroyed as viable tumor cells were found to regrow. In order to develop a more effective therapy, a novel irradiation method should be developed that is able to treat deep tumors without skin damage, possibly by employing active cooling of the skin surface.

5. Conclusion

We have demonstrated the potential of PTT, using systemic or local delivery of GNRs together with only two applications of NIR laser light, to treat tumors in the proper-ALN. Future studies optimizing the characteristics of the GNRs, and the methods used for the delivery of GNRs and laser irradiation, may allow for the development of an effective and minimally invasive treatment for metastatic lesions.

NANOMEDICINE

NANOMEDICINE

Acknowledgments

This study was supported by a Grant for the World Center of Education and Research for Trans-disciplinary Flow Dynamics, Tohoku University Global COE Program, and a Grant for the Collaborative Research Project (J13094) of the Institute of Fluid Science, Tohoku University, a Grant-in-Aid for Challenging Exploratory Research (24659884, 24650286), and a Grant-in-Aid for Scientific Research (B) (23300183, 25293382). The authors thank M. Ono and M. Nose for helpful discussion, N. Sax for technical assistance, and the Biomedical Research Core of Tohoku University Graduate School of Medicine for technical support.

References

[1] L. Li, S. Mori, M. Kodama, M. Sakamoto, S. Takahashi, T. Kodama, Enhanced sonographic imaging to diagnose lymph node metastasis: importance of blood vessel volume and density, Cancer Res. 73 (2013) 2082–2092.
[2] I.J. Robertson, F. Hand, M.R. Kell, FDG-PET/CT in the staging of local/regional metastases in breast cancer, Breast 20 (2011) 491–494.
[3] J.E. Gershenwald, M.I. Ross, Sentinel-lymph-node biopsy for cutaneous melanoma, N. Engl. J. Med. 364 (2011) 1738–1745.
[4] A.M. Alkilany, L.B. Thompson, S.P. Boulos, P.N. Sisco, C.J. Murphy, Gold nanorods: their potential for photothermal therapeutics and drug delivery, tempered by the complexity of their biological interactions, Adv. Drug Deliv. Rev. 64 (2012) 190–199.
[5] J. Chen, D. Wang, J. Xi, L. Au, A. Siekkinen, A. Warsen, Z.Y. Li, H. Zhang, Y. Xia, X. Li, Immuno gold nanocages with tailored optical properties for targeted photothermal destruction of cancer cells, Nano Lett. 7 (2007) 1318–1322.
[6] J. You, R. Zhang, G. Zhang, M. Zhong, Y. Liu, C.S. Van Pelt, D. Liang, W. Wei, A.K. Sood, C. Li, Photothermal-chemotherapy with doxorubicin-loaded hollow gold nanospheres: a platform for near-infrared light-trigged drug release, J. Control. Release 158 (2012) 319–328.
[7] W.S. Kuo, Y.T. Chang, K.C. Cho, K.C. Chiu, C.H. Lien, C.S. Yeh, S.J. Chen, Gold nanomaterials conjugated with indocyanine green for dual-modality photodynamic and photothermal therapy, Biomaterials 33 (2012) 3270–3278.
[8] G. Ku, L.V. Wang, Deeply penetrating photoacoustic tomography in biological tissues enhanced with an optical contrast agent, Opt. Lett. 30 (2005) 507–509.
[9] H.K. Moon, M. Son, J.E. Park, S.M. Yoon, S.H. Lee, H.C. Choi, Significant increase in the water dispersibility of zinc phthalocyanine nanowires and applications in cancer phototherapy, NPG Asia Mater. 4 (2012) e12.
[10] G. von Maltzahn, J.H. Park, A. Agrawal, N.K. Bandaru, S.K. Das, M.J. Sailor, S.N. Bhatia, Computationally guided photothermal tumor therapy using long-circulating gold nanorod antennas, Cancer Res. 69 (2009) 3892–3900.
[11] X. Huang, I.H. El-Sayed, W. Qian, M.A. El-Sayed, Cancer cell imaging and photothermal therapy in the near-infrared region by using gold nanorods, J. Am. Chem. Soc. 128 (2006) 2115–2120.
[12] X. Huang, I.H. El-Sayed, W. Qian, M.A. El-Sayed, Cancer cells assemble and align gold nanorods conjugated to antibodies to produce highly enhanced, sharp, and polarized surface Raman spectra: a potential cancer diagnostic marker, Nano Lett. 7 (2007) 1591–1597.
[13] J. Wang, B. Dong, B. Chen, Z. Jiang, H. Song, Selective photothermal therapy for breast cancer with targeting peptide modified gold nanorods, Dalton Trans. 41 (2012) 11134–11144.
[14] S. Shen, H. Tang, X. Zhang, J. Ren, Z. Pang, D. Wang, H. Gao, Y. Qian, X. Jiang, W. Yang, Targeting mesoporous silica-encapsulated gold nanorods for chemo-photothermal therapy with near-infrared radiation, Biomaterials 34 (2013) 3150–3158.
[15] G.P. Goodrich, L. Bao, K. Gill-Sharp, K.L. Sang, J. Wang, J.D. Payne, Photothermal therapy in a murine colon cancer model using near-infrared absorbing gold nanorods, J. Biomed. Opt. 15 (2010) 018001.
[16] Y. Matsumura, H. Maeda, A new concept for macromolecular therapeutics in cancer chemotherapy: mechanism of tumoritropic accumulation of proteins and the anti-tumor agent smancs, Cancer Res. 46 (1986) 6387–6392.
[17] J.T. Robinson, K. Welsher, S.M. Tabakman, S.P. Sherlock, H. Wang, R. Luong, H. Dai, High performance *in vivo* near-IR (>1 mum) imaging and photothermal cancer therapy with carbon nanotubes, Nano Res. 3 (2010) 779–793.
[18] A.J. Gormley, K. Greish, A. Ray, R. Robinson, J.A. Gustafson, H. Ghandehari, Gold nanorod mediated plasmonic photothermal therapy: a tool to enhance macromolecular delivery, Int. J. Pharm. 415 (2011) 315–318.
[19] X.F. Yu, Z. Sun, M. Li, Y. Xiang, Q.Q. Wang, F. Tang, Y. Wu, Z. Cao, W. Li, Neurotoxin-conjugated upconversion nanoprobes for direct visualization of tumors under near-infrared irradiation, Biomaterials 31 (2010) 8724–8731.
[20] M. Jaunich, S. Raje, K. Kim, K. Mitra, Z.X. Guo, Bio-heat transfer analysis during short pulse laser irradiation of tissues, Int. J. Heat Mass Transfer 51 (2008) 5511–5521.
[21] L. Li, S. Mori, M. Sakamoto, S. Takahashi, T. Kodama, Mouse model of lymph node metastasis via afferent lymphatic vessels for development of imaging modalities, PLoS ONE 8 (2013) e55797.
[22] E.D. Murphy, J.B. Roths, Autoimmunity and lymphoproliferation: induction by mutant gene lpr, and acceleration by a male-associated factor in strain BXSB mice, Elsevier/North-Holland, New York, 1978.
[23] L. Shao, S. Mori, Y. Yagishita, T. Okuno, Y. Hatakeyama, T. Sato, T. Kodama, Lymphatic mapping of mice with systemic lymphoproliferative disorder: usefulness as an inter-lymph node metastasis model of cancer, J. Immunol. Methods 389 (2013) 69–78.
[24] T. Kodama, N. Tomita, Y. Yagishita, S. Horie, K. Funamoto, T. Hayase, M. Sakamoto, S. Mori, Volumetric and angiogenic evaluation of antitumor effects with acoustic liposome and high-frequency ultrasound, Cancer Res. 71 (2011) 6957–6964.
[25] N. Khlebtsov, L. Dykman, Biodistribution and toxicity of engineered gold nanoparticles: a review of *in vitro* and *in vivo* studies, Chem. Soc. Rev. 40 (2011) 1647–1671.
[26] L.R. Hirsch, R.J. Stafford, J.A. Bankson, S.R. Sershen, B. Rivera, R.E. Price, J.D. Hazle, N.J. Halas, J.L. West, Nanoshell-mediated near-infrared thermal therapy of tumors under magnetic resonance guidance, Proc. Natl. Acad. Sci. U. S. A. 100 (2003) 13549–13554.